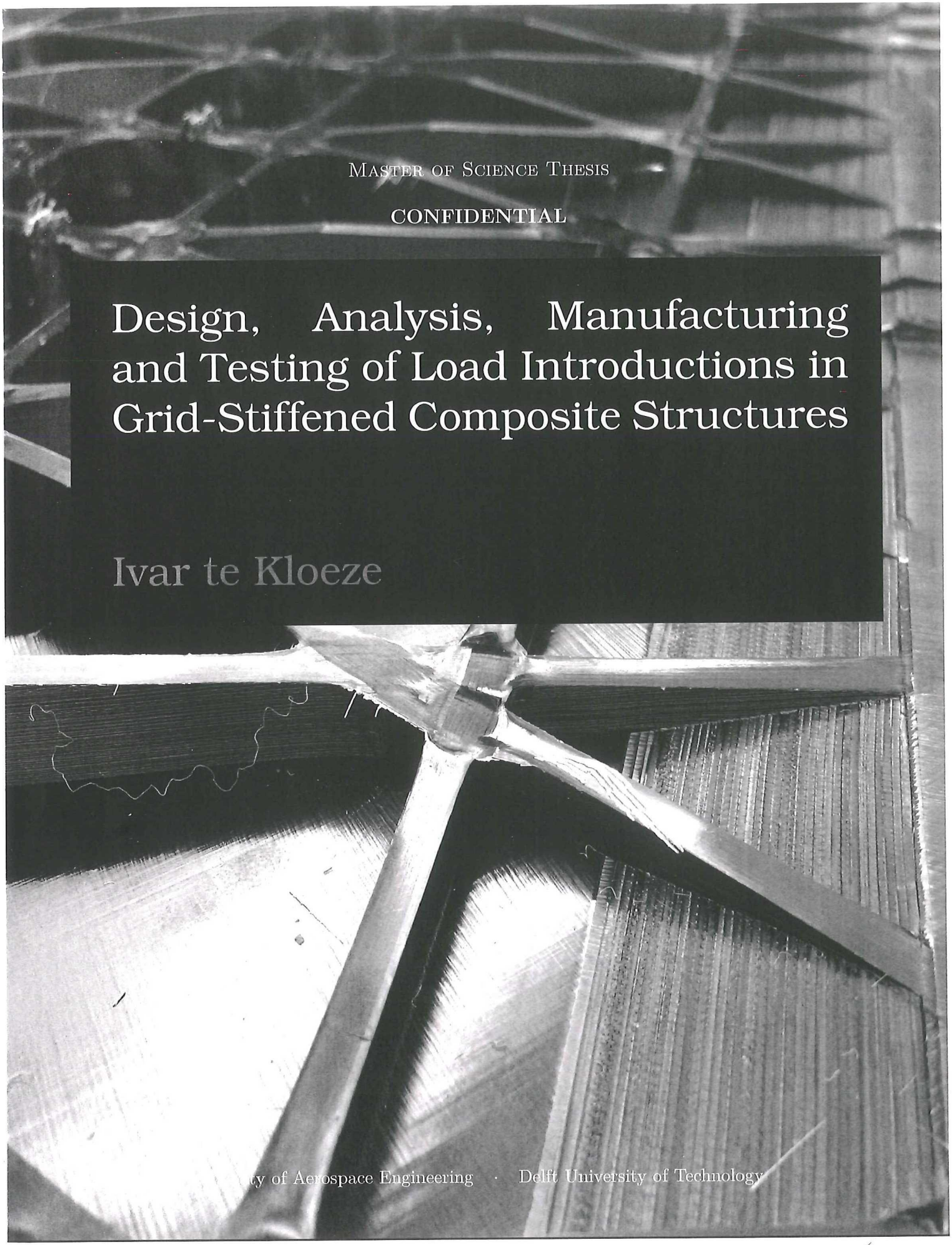

Master of Science Thesis

CONFIDENTIAL

Design, Analysis, Manufacturing and Testing of Load Introductions in Grid-Stiffened Composite Structures

Ivar te Kloeze

ty of Aerospace Engineering · Delft University of Technology

CONFIDENTIAL

Design, Analysis, Manufacturing and Testing of Load Introductions in Grid-Stiffened Composite Structures

MASTER OF SCIENCE THESIS

For obtaining the degree of Master of Science in Aerospace Engineering
at Delft University of Technology

Ivar te Kloeze

2015-11-6

Faculty of Aerospace Engineering · Delft University of Technology

The work in this thesis was completed for and with significant support from ATG Europe. Their input is gratefully acknowledged.

Delft University of Technology
Faculty of Aerospace Engineering
Department of Aerospace Structures and Materials

GRADUATION COMMITTEE

Dated: 2015-11-6

Chair holder:

dr. C. Kassapoglou

Committee members:

dr. ir. O.K. Bergsma

dr. ir. S. Shroff

ir. S.M. Simonian

Abstract

Grid-Stiffened composite structures have found their way into a variety of applications for their structural efficiency, cost and inherent damage tolerance. Where previous studies and research have focused on global optimization of the far-field grid structure, the current work focuses on the development of an efficient though versatile load introduction zone at the edge of the structure. A global lightweight design requires structural efficiency throughout the structure. Therefore, having a versatile design for the load introduction zones allows for optimization of the far-field structure and can result in a design that efficiently transfers loads to the next structure. To this end a design is developed where the ribs are interwoven with a laminate which can then easily be connected to the next structure. A parametrized Finite Element Method model has been verified through correlation with two different designs which also proves versatility of the rib-to-laminate concept. Using this FEM model the load introduction zone can be optimized for a variety of grid structures and layouts. Since limitations and effects of the manufacturing process can make or break a design, the two analyzed designs are manufactured and tested to prove feasibility and performance. Their quality is assessed and used as input for improvement of the FEM model. The end result is a parametrized and verified concept for load introductions that can be used in the global optimization of a grid-stiffened composite structure.

Table of Contents

List of Figures

List of Tables

List of Symbols

List of Symbols

Abbreviations

AFP	Automated Fiber Placement
CAD	Computer Aided Design
CFRP	Carbon Fiber Reinforced Polymer
CNC	Computer Numerical Control
DAQ	Data acquisition
DASML	Delft Aerospace Structures and Materials Lab
DIC	Digital Image Correlation
DIM	Improved Dimensional
ESA	European Space Agency
FBD	Free Body Diagram
FEM	Finite Element Method
FVF	Fiber Volume Fraction
GS	Grid-Stiffened
LVDT	Linear Variable Differential Transformers
MAT	Material Assignment
QI	Quasi Isotropic
SG	Strain Gages

Greek Symbols

ν	Poisson's ratio

Latin Symbols

E11	Modulus in fiber direction
E22	Modulus in transverse direction
G12	Shear modulus
t_{ply}	Ply thickness

Acknowledgments

First and foremost I would like to thank ATG Europe for giving me the opportunity to work on this great project. A special thanks to Samo Simonian and Leonid Pavlov for their support throughout my thesis. I am definitely looking forward to be working with you.

To the same extent I would like to thank Christos Kassapoglou for being my supervisor in this project. You have motivated me to go the extra mile, not only during my thesis but throughout my master.

I would like to thank Otto Bergsma and Sonell Shroff for being part of my graduation committee.

I would like to thank Thijs Papenhuijzen and Bart Smeets for helping me out during manufacturing and testing. In this stressful period I might not have been the most cheerful person to work with, but your company and support is highly appreciated. To this end I also would like to thank the DASML staff and in particular Gertjan Mulder who has assisted with testing, making it all happen.

Last but not least I want to thank Vincent Maes for all kinds of modeling support and reminding me of the fact that Murphy lives close by.

Delft, University of Technology
2015-11-6

Ivar te Kloeze

"#IvarProblems"

— *Vincent K. Maes, 2014*

Chapter 1

Introduction

1.1 Background Information

Grid-Stiffened (GS) structures are, as the name implies, structures in which the stiffening elements form a grid. Such a grid consists of stiffeners running in multiple directions. In contrast to a skin stiffened structure where stiffening elements are used to reinforce or stabilize a skin, in a GS structure the grid can be the main load carrying element. As such these structures do not rely on having a skin and can be made with or without one. The result is an integrated functionality of these grid members, which are often called ribs, making GS structures structurally efficient. Having multiple load-paths also improves redundancy as any failure is expected to be limited to a single cell. This inherent damage tolerance and also the fact that GS structures can be manufactured as a single part helps them outperform other types of structures, such as a sandwich, monolithic or skin stiffened structure, in terms of structural efficiency, cost and redundancy.

GS structures have been around for quite some time and can be found in many applications such as aircraft, launch vehicles and spacecraft structures. In recent decades much progress has been made in analysis, optimization and manufacturing of global 'far-field' structures. Far-field refers to an undisturbed grid section, which does not include any local details of which the effects are often overlooked or underestimated. These details include, among others, cut-outs, reinforcements and (local) load introductions. A lightweight design requires efficiency on all fronts, so both an optimized far-field grid structure and efficient load transfer from adjacent structures into the far-field structure. Loads can be introduced either in-panel, which will be called attachments, and at the edge of the panel, which will be called edge-of-panel load introductions. These load introductions can have an effect on the far-field grid structure and vice versa. So a weight-optimized design is obtained iteratively and requires all designs to be versatile.

Seeing the potential, ATG Europe has started the in-house development of GS structures for a range of applications, one of which is the Interstage 2/3 of the Ariane 6 launcher. To come to a complete design for a GS structure three main areas were identified and developed in parallel; the far-field grid structure (with cut-outs), load introduction zones at the edge-of-panel and local in-panel attachments. This thesis presents the development of the edge-of-panel load introductions.

1.2 Research Objectives

The objective of this thesis is to aid in the development of grid-stiffened composite structures in total by:

Developing a versatile lightweight solution for edge-of-panel load introductions in grid-stiffened composite structures.

A versatile solution is not limited to a single design of a far-field structure but can be used in different configurations or global designs. That means the solution has to be able to adapt to different (grid) geometries and load cases.

The development consists of a full design cycle including:

- Conducting a literature study to define the state-of-art
- Creating and analyzing a versatile design
- Detailed analysis, by Finite Element Method (FEM)
- Manufacturing of samples to verify feasibility and manufacturability
- Testing of samples to verify performance and provide data for design model correlation
- Correlating and improving design model using obtained manufacturing quality results and test data

This research will address all theoretical and practical aspects of load introductions in grid stiffened composites and creates links between the aspects. And thus does not focus on a single specific item in the design cycle. The analysis will focus on the global and local elastic behavior quantitatively, whereas failure is qualitatively accounted for in the research. Detailed analysis will be done using FEM models which allow for optimization and hence should be versatile. The models have to be able to indicate the critical areas and in combination with a suitable failure criterion give a prediction for strength.

Feasibility of the designs has to be verified through, among others, manufacturing. A detailed quality assessment of the samples will lead to an understanding of the implications and effects of manufacturing on the global performance of the structure. Performance of the designs has to be verified though mechanical tests which also allow for correlation and verification of the FEM models.

1.3 Thesis Structure

The thesis will start with a literature study in Chapter 2 which focuses on existing solutions for load introductions. Based on the findings in literature a design is created and analyzed in Chapter 3. To this end a global FEM model is created to perform trend studies on different design parameters that will allow for weight optimization of the structure. The results from these trend studies are then converted into two different test sample designs that will be used to verify the global FEM model. The test sample designs are described and analyzed in Chapter 4. Chapter 5 describes the manufacturing of these test samples as well as a detailed assessment of their quality. Testing of the samples and correlating the results with the corresponding test sample models can be found in Chapter 6. The results from the correlation are then combined with the findings of the quality assessment to improve the test sample models in Chapter 7. The final conclusions and recommendations for further research are presented in Chapter 8. To make the report readable many of the test and correlation results are not presented in the corresponding chapters, but can be found in the appendices.

Chapter 2

Literature Study

In this chapter the different existing solutions for attachment regions in GS structures, as presented in literature, are reviewed. The concepts are assessed based on criteria such as design (or alteration), working principle, advantages, disadvantages, analysis methods, manufacturability, reproducibility and any other aspects that are specific to that solution. The focus of this thesis and literature study is on the load introductions in GS structures and hence only literature that is related to this specific area is presented.

First a short overview of the current state-of-art of GS structures is given, followed by a more detailed overview of existing load introduction solutions. Conclusions are drawn in the final section.

2.1 State-of-Art

The research in grid-stiffened composite structures has mainly been limited to global design & optimization [5–9] and manufacturing [10–13]. Limited documented effort has been made on the design, analysis and optimization of details in GS structures, like load introduction. These details however could potentially have a big effect on the overall performance of a part or product. The mass of the attachment rings of the CFRP Grid Stiffened conical payload adapter of the Proton-M launcher for example add up to roughly 40% of the mass of the total adapter [14].

Examples of grid-stiffened structures are discussed in literature quite extensively. The solutions for the load introduction zones can be categorized in four main concepts and are called, in this thesis, edge rib, flattened rib, insert or laminate.

2.1.1 Edge Rib Concept

An end-of-panel attachment that can be found often in literature is the concept where a rib of the grid forms the interface between the Grid Stiffened structure and the adjacent structure. The adjacent structure is attached (bolted/riveted) to this edge rib [1,14–17]. An example of such a connection is shown in Figure 2.1. In this sample the yellow strip is the rib along the edge of the structure. Relatively high ribs allow for the attachment bolts to run through this edge rib directly.

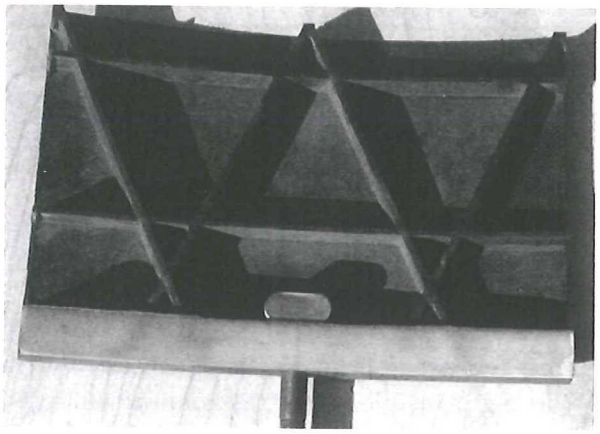

Figure 2.1: Example of edge rib concept [1]

For most structures these edge ribs are thicker hoop ribs, which are uni-directional. For a tension load-case the helical ribs will pull on the edge rib resulting in bending of the edge rib as shown in Figure 2.2. These uni-directional ribs will not perform well in bending, being vulnerable to splitting. Thicker ribs will be required to keep the inter-laminar stresses low and prevent this type of failure. Depending on the manufacturing process it might be possible to incorporate angled plies in these edge ribs, however this has not been shown in literature. Another downside is that all loads from the helical ribs are transferred through a relatively small overlap with the edge rib, creating a potential critical weak spot.

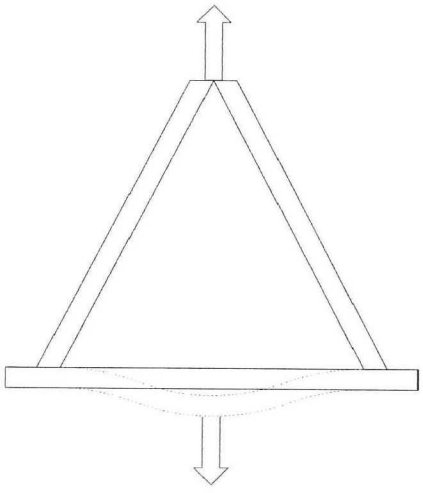

Figure 2.2: Sketch indicating bending of edge rib for tensile loads

An alteration on this design has been developed [10]. Near the edge ribs the structure is left without the skin to allow for the installation of the bolts. The strength of the edge rib however is dictated by its quality and dimensions. For a dry filament winding process (manufacturing process where dry continuous fibers are wound around a mandrel) for example, this is dictated by the tool expansion during cure, the width of the tool, the width of the dry fiber tows and the amount of tension applied during winding. All of which have a big influence on the performance of the edge rib concept.

The upper and lower interface flanges of the Proton-M conical payload adapters are connected to the adjacent structure using an edge rib [14]. The design and optimization of the composite grid-stiffened adapter has been researched quite thoroughly. Analytical [13, 15] and computational analysis [16] methods were used to optimize the grid structure, but the attachment zones were not analyzed to the same level of detail.

Most optimization studies for GS structures using FEM make use of either beam, shell or solid elements. The complex geometry of the edge ribs and local effects require a detailed model. For bigger structures, having a very detailed model quickly becomes very demanding computationally. To overcome this (potential) issue, local modeling can be used; only small sections are modeled in detail. One can go as far as modeling each individual layer or ply [18]. The quality of the model depends on the detail of the model and the implementation of the failure criteria. Modeling each ply requires either very good control of manufacturing to make sure plies are placed as modeled or a lot of complex modeling to model each ply as it is cured. At the nodes multiple ribs intersect. The fiber volume fraction will change drastically where plies are overlapping. This will change the material properties within each ply. So modeling each individual ply and assigning correct material properties will be cumbersome. This method will only also work with manufacturing processes where either no movement of the material is expected or where the material movement can be predicted accurately.

2.1.2 Flattened Rib Concept

One way of avoiding the edge rib is by changing the aspect ratio of the helical ribs such that a fastener can be run directly through. At the edge of the panel the individual tows in the ribs are spread [2]. By locally increasing the width of the rib, whilst keeping the same number of tows, the height of the rib is reduced. This spreading allows for bolting through a rib without cutting all fibers creating a direct load path from the fasteners to the ribs. Downside of this concept is that the individual plies have to be steered, increasing the complexity of layup.

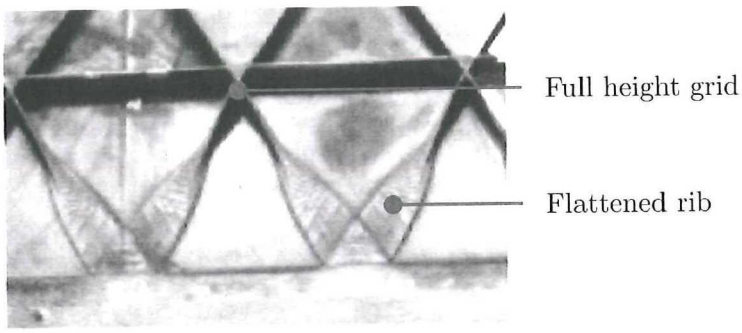

Figure 2.3: Example of flattened rib concept [2]

2.1.3 Insert Concept

Another concept incorporates a metal insert in the grid-stiffened structure [1, 19]. The end of the helical ribs and often a hoop rib are enclosed by an insert which is then connected to the next structure. Loads will be spread more evenly over the ribs reducing the risk of local failure in the composite. The insert is either bonded or co-cured to the grid structure. The composite tapes or tows can be placed in grooves in the insert directly which in that case replaces part of the tooling. This allows for a single manufacturing step. This also limits the applicability to every manufacturing process. A pre-preg material is often cured at elevated temperatures, potentially introducing thermal stresses at the interface between the insert and the composite due to a difference in thermal expansion coefficient. The insert also hinders the compaction of the ribs for processes which rely on rubber tooling forming and compacting the ribs. Since no holes have to be drilled in the ribs themselves, there is no limit on the dimension or geometry of the ribs.

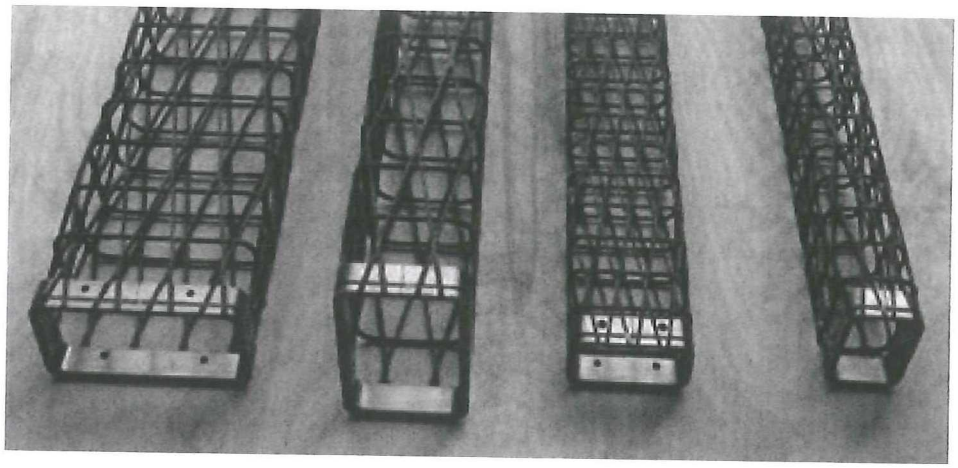

Figure 2.4: Example of incorporating a metal ring in the grid structure [1]

2.1.4 Laminate Concept

For skin-stiffened structures where the skin carries most of the load the stiffening elements are often terminated towards the edges and the load is transferred to the next structure through the skin. Grid-stiffened structures are different in this respect since the grid carries most of the load. Nevertheless examples can be found where the ribs terminate near the edge and the extending skin is fastened to the next structure [20, 21]. The skin in these cases has to be reinforced to provide adequate strength and stiffness [22]. The relatively stiff skin carries most of the load and by gradually dropping skin plies the load is transfered into the ribs. This reduces the risk of skin-rib separation [20].

A special alteration of this concept is shown in Figure 2.5. Domes are machined in a thick laminate allowing for in-plane fastening. The ribs in this case are terminated before the skin laminate is build up.

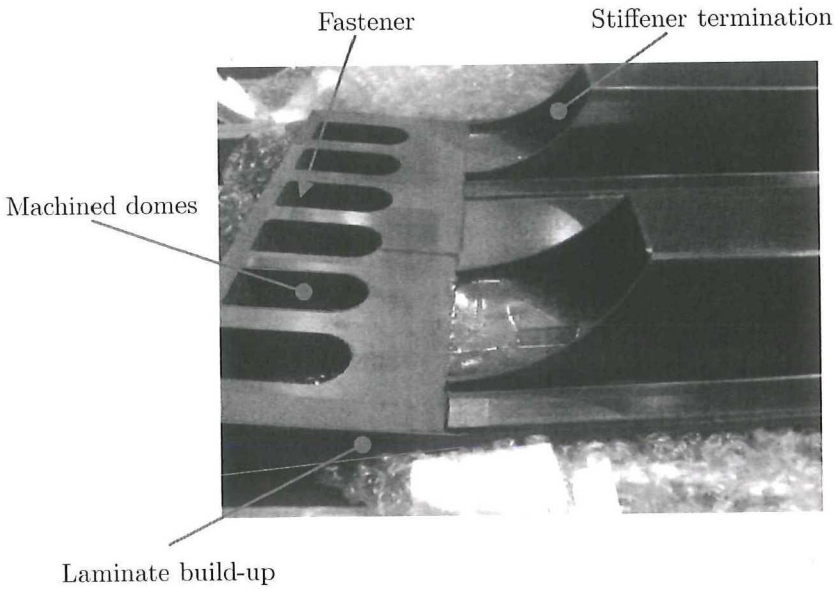

Figure 2.5: Example of laminate concept for in-plane fastening [3]

2.2 Conclusion

From the literature review can be concluded that solutions for edge-of-panel attachments in Grid Stiffened composite structure do exist. However none of the research published so far has focused on the optimality of the attachment zones or the details of local load transfer and re-distribution while it has been shown that these areas can have a big impact on the total mass of the structure [14]. Finding the optimum mass design starts with accurately predicting mechanical properties, such as stiffness and strength. The method described in [18] might be a good start. The Grid Stiffened structures considered for this research will be manufactured using pre-preg carbon fiber tape, making the Finite Element method described in [18] suitable for practically all concepts described. The next step towards mass optimality is the optimization method itself. None of the literature reviewed in the previous chapter shows any optimization method. The optimal mass solution will be different for almost every case and could even be a combination of two or more concepts. Some flattening of the ribs could for example be used to prevent skin-rib separation for the laminate concept. Finding the optimal mass designs therefore requires a method which can combine the different concepts. Some concepts however have limitations; the edge rib concept for example needs a certain minimum rib size to allow bolts through, whereas the other concepts have no minimum rib size. The flattened rib concept on the other hand requires the use of pre-preg material or in-situ curing to be able to steer the material in more complex shapes contrary to the other concepts which can be made with practically every composite material. This means a well-defined design space is required to select the right concept or combination.

- Solutions for load introductions in grid-stiffened composite structures do exist, although limited
- Load introduction zones can have a big impact on the total mass of the structure

- Little has been published on the analysis and performance of these local details in grid-stiffened structures
- Any optimal design is most likely a combination of the various load introduction concepts
- Manufacturing processes limit the applicability of the different concepts
- Manufacturing quality potentially has a huge influence on part performance

Based on this discussion, the focus of this thesis is on the development of a versatile load introduction zone by predicting, though detailed analysis, global and local elastic behavior and relating manufacturing quality to the performance as outlined in Chapter 1.

Chapter 3

Design and Analysis

Various concepts for load introductions in grid-stiffened structures have been presented in Chapter 2. It goes without saying that there is not a single design that will work in all cases. Every application is different, so every optimal design is different. The design process nevertheless could be similar for all concepts. A design case is needed that on the one hand will be specific enough to allow for convergence towards an optimum and on the other hand will still be versatile enough that the design process can be applied on a variety of cases. The load introduction into the interstage 2/3 for the Ariane 6 launcher has been selected for this research.

Based on the requirements and project limitations, outlined in Section 3.1, and the concepts found in literature a design is developed. Due to the complex nature of the problem a FEM is used for analyzing and optimizing the structure while keeping in mind applicable design rules. Using this FEM model a trend-study is performed to investigate the influence of the different design parameters on the overall performance in Section 3.4.

3.1 Design Case

Ariane 6 is still under development but the global geometry and requirements for one of its iteration configurations are outlined in the Request For Consultation provided by the European Space Agency (ESA) [23]. The interstage consists of a conical section with cylindrical ends as shown in Figure 3.1. The top end is connected to the third stage through a separation ring and the bottom end is connected to the second stage directly. The total interstage is 7.7m long of which the bottom and top cylindrical sections are 1.0m and 0.7m long respectively. The bottom section has a diameter of 3.5m and the top section has a diameter of 4.0m. For the remainder of this research it has been assumed that the attachment zone does not run into the conical section and thus has only a single curvature.

The design of the separation ring itself is beyond the scope of this thesis. In the current (or previous) design the separation ring is bonded to a honeycomb interstage structure. For this reason it is assumed that the grid-stiffened interstage as developed is going to be bonded

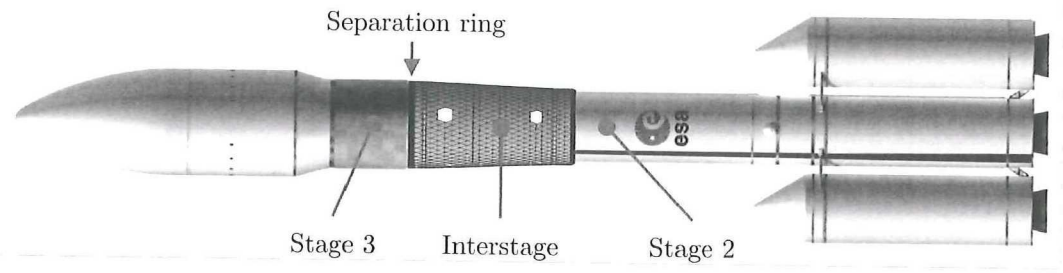

Figure 3.1: Ariane 6 showing interstage and separation ring

to this ring as well. An impression of the separation ring can be seen in Figure 3.2. The dimensions of the ring can be tailored to the thickness of the composite. The bottom end of the interstage is most likely bolted to the second stage. It has been decided that the top attachment is the main focus and that the bottom attachment is outside the scope of this Thesis.

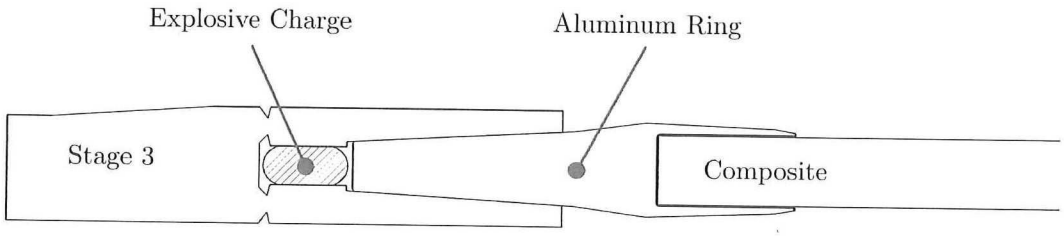

Figure 3.2: Cross-sectional drawing of the separation ring assembly

The load case for the interstage is defined as follows:

- Maximal expected compression mechanical flux of 1200 kN/m at the lower flange.
- Maximal expected tension mechanical flux of 350 kN/m at the lower flange.

Since the upper flange has a larger diameter the compressive mechanical flux reduces to 1050 kN/m and the tension mechanical flux reduces to 306.25 kN/m. While the real structure might experience more complex loads, no combined loading is taken into account at this point.

3.1.1 Project Limitations

Parallel to this thesis a optimization of the global interstage is performed by ATG Europe [4]. The results of this work are used as inputs for the development of the load introductions. The grid structure and dimensions are based on the global optimization and will be fixed for the remainder of this research. Small changes should not affect the design to such an extent that the analysis becomes inapplicable. Hence the design and analysis should be flexible to allow for global design changes.

The far field grid structure is based on the global optimization and an overview is given in Table 3.1. Tailoring of the grid at the attachment zone to find the lightest load introduction is

the goal of the thesis, so the limitations on the grid structure mentioned are only fixed at the interface with the far-field structure. The area affected by geometrical changes is considered attachment zone.

Table 3.1: Far-field grid structure dimensions based on global optimization [4]

Variable	Dimension
Grid Type	Regular triangular
Helical Rib Angle	20°
Helical Rib Spacing	157.0mm
Hoop Rib Spacing	215.7mm
Rib Width	10mm
Rib Height	30mm
Skin Layup	[45/-45/-45/45/90]2s
Grid mass (axial)	152 g/mm

A Carbon Fiber Reinforced Polymer (CFRP) material is selected. The Hexcel IM7/8552 pre-preg is readily available and has good mechanical properties. A pre-preg material is used based on the future potential of Automated Fiber Placement (AFP) as manufacturing process for the interstage. The manufacturing of test-samples described in Chapter 5 however is done by hand, since no fiber placement robot is available at this point. For a small number of samples a fiber placement robot will only increase the complexity of manufacturing.

For the creation and solving of the FEM models ABAQUS is used. Computer Aided Design (CAD) models are generated with CATIA and are imported in ABAQUS through a STEP file conversion. Scripting of the FEM models and parametrization of the CAD models allowed for easy implementation of design changes.

3.2 Global Design

In Chapter 2, four main concepts for the load introduction are described. The design presented in this section is based on a combination of the edge rib, laminate and flattened rib concept. A laminate is bonded to the separation ring on both faces as depicted in Figure 3.2. By bonding on both faces, peel stresses in the adhesive, due to local bending arising from eccentricity, are limited and shear stresses in the adhesive are lowered. An additional benefit of enclosing the laminate is that compressive loads are led directly into the aluminum ring through the end of the laminate. A Free Body Diagram (FBD) is presented in Figure 3.3.

Since the ribs in the global structure are the load carrying elements, terminating the ribs prior to the laminate would require a skin strong enough to carry all the loads. Terminating the ribs would also drastically reduce both the membrane and bending stiffness locally. For proper load transfer the ribs are integrated in the laminate. The rib plies are interwoven with the laminate plies over a length of twice the distance between successive ply-drops of the laminate. This way buildup in the laminate never exceeds 1 or 2 plies respectively, by which excessive build-up in the laminate is avoided. The overlap however should be large enough

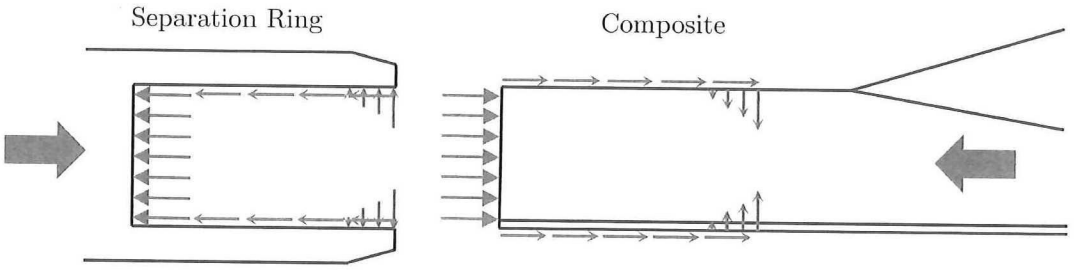

Figure 3.3: FBD showing applied loads and internal stresses

that the shear stresses at the interface do not exceed the interlaminar shear strength. By dropping the rib plies at a finite distance in the laminate, the rib plies do not become part of the laminate plies. This makes the orientation of the laminate plies independent of the orientation of the helical ribs.

Plies in the ribs are dropped to bring the ribs to the same height as the laminate. Providing that the bending stiffness is adequate, the ribs only need the height of the laminate at the interface. The tapering of ribs is done at a constant taper ratio. Further optimization might indicate that a non-constant taper ratio is better, but these small improvements are beyond the scope of this research. As indicated by [24] the dropped rib plies should be interspersed with the continuing rib plies to distribute the load transfer over all rib plies rather than a single one. This automatically ensures that the ply-drops of the ribs are internal. The ply drops for the laminate will be external due to the interwoven rib plies.

To prove feasibility of the design, samples (shown in Figure 3.4) are manufactured following the same approach as described in chapter 5. From these samples can be concluded that an excessive buildup at the rib-laminate interface can be avoided by dropping the rib plies at a fixed distance in the laminate.

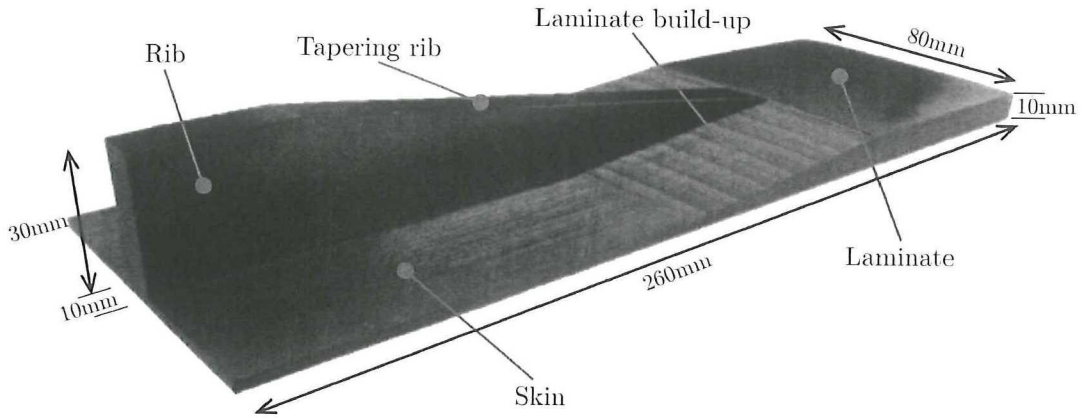

Figure 3.4: Sample proving feasibility design

The adhesive ScotchWeld 9323 B/A made by 3M has been selected for the adhesive in the design. This adhesive shows good mechanical properties and is readily available. It is representative for the adhesives which are used in the (aero)space industry. Maximum shear strength is obtained with a bond line thickness of 0.1-0.2mm [25]. To allow for deviations in the laminate thickness and other manufacturing tolerances the upper value (0.20mm) is used.

3.3 Global Model

The analysis of the design will be done using FEM. A rather detailed model is required to capture all the local effects. First the modeling approach will be discussed. The FEM model is a representation of the real structure and not every detail can be modeled, so simplifications have to be made. These simplifications are outlined in Section 3.3.2.

3.3.1 Modeling Approach

To keep the model computational efficient only the attachment zone is modeled. The attachment zone is defined as the area that is affected by geometrical changes to the far-field grid structure as outlined in Table 3.1. The effects of geometry changes might extend beyond a cell of the grid structure, so in axial direction an additional far-field cell is modeled. This also ensures the attachment zone itself is free of edge and boundary effects. Since the applied load is constant along the circumference and the structure is radially symmetric, the interstage can be split in 72 identical sections. Each section consisting of a set of helical ribs. This forms the minimum size section that would still allow for a representative analysis of the entire attachment zone. To eliminate any edge and boundary effects three of these sections are combined. The final geometry is shown in Figure 3.5.

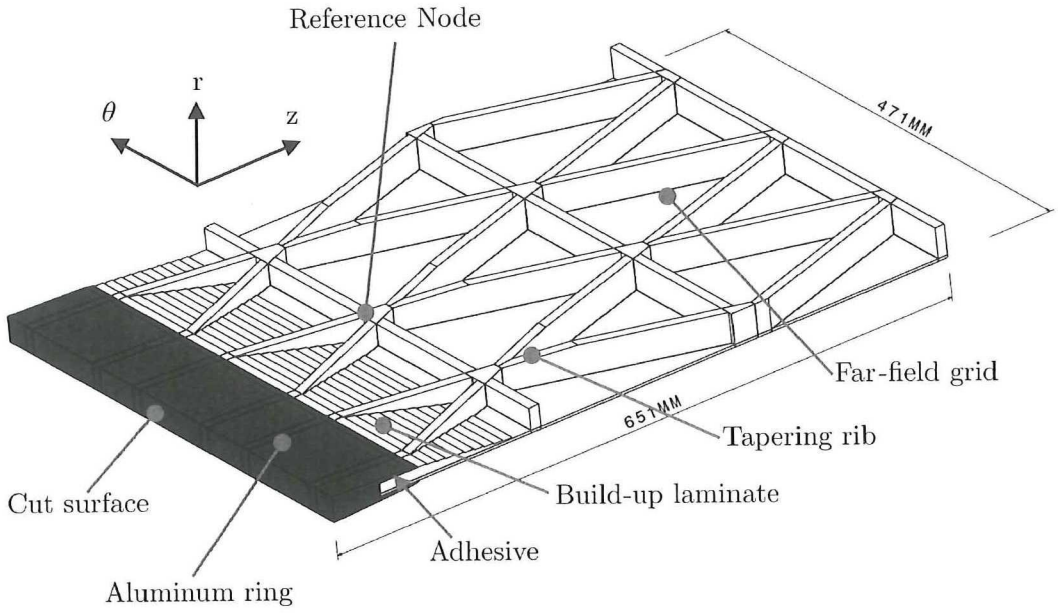

Figure 3.5: Outline geometry used for global analysis. Axial direction indicated by 'z', radial by 'r' and circumferential by 'θ'

The design of the aluminum separation ring is not part of this research, however the aluminum ring is partly modeled to ensure that a realistic boundary condition is applied to the adhesive and composite. The cut surface of the aluminum ring is then fixed in axial direction. The stress at this surface should be uniform along the circumference of the ring. Any stress difference on this surface might indicate that the fixed boundary condition, being infinitively stiff, has an effect on the stress fields. Since the structure is radially symmetric, two symmetry

boundary conditions can be applied at the side edges. The symmetry planes intersect with the axis of the interstage, as can be seen in Figure 3.6. The structure is free to move parallel but cannot move normal these symmetry planes. Loading is applied by displacing the hoop rib at the end of the structure. This displacement field of the top surface is uniform.

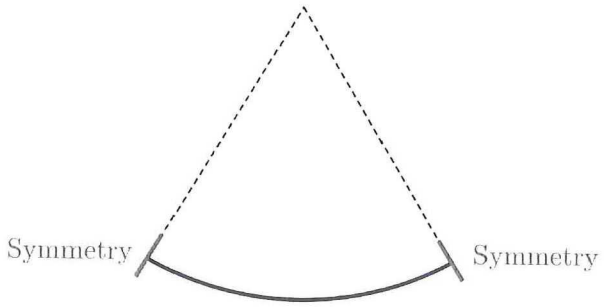

Figure 3.6: Symmetry boundary conditions for global model

To capture the major local effects such as transverse shear and interlaminar stresses 3D solid elements are used. Composite layups are used for the skin, laminate and nodes to model the plies with different orientations. Even though the ribs are laid up as plies, the ribs are modeled pure unidirectional effectively making it a homogeneous material. Hence the ribs are assigned oriented material properties. Special attention has to be paid to the mesh in the section with a composite layup. ABAQUS will assign the defined layup to every element. So changing the number of elements through the thickness changes the layup. For example having twice the number of elements, results in twice the number of plies. Since the element size has been halved the thickness per ply will be half, effectively changing only the stacking sequence. The A matrix will not change. The B and D matrices however depend on the stacking sequence. So changing the mesh size without changing the corresponding layups will also influence the behavior of the composite layups.

For such a stiff structure material failure is expected before any significant buckling will occur. The non-linear effects are therefore small and the model is solved linearly. This prevents the model from becoming computationally heavy and allows for performing relatively quick trend studies which will be discussed in Section 3.4.

The material properties that will be used in the analysis are given in Table 3.2.

3.3.2 Simplifications

There is a fine line between being too accurate and not accurate enough. Any shortcuts in modeling could potentially lead to inaccurate results. But making the model 100% accurate is virtually impossible. So it is important to clearly state the simplifications of the model. The main simplification will be discussed in this section.

The first simplifications were already mentioned in Section 3.3.1; sub-modeling of the attachment zone, (simplified) boundary conditions, linear modeling and the elements used.

As mentioned the interstage is cylindrical with a diameter of 4m at the upper attachment zone. Numerous attempts have been made during this thesis to create a curved model using solid elements. Due to the complexity of the rib-laminate interface the model has to be

Table 3.2: Material properties used in the global model

Material	Property	Value
Hexcel 8552 IM7	E11	143.0 GPa
	E22	11.5 GPa
	G12	5.0 GPa
	ν	0.32
	t_{ply}	0.127 mm
Aluminum 7075-T6	E	71.7 GPa
	ν	0.33
ScotchWeld 9323 b/A	E	2.1 GPa
	ν	0.37

partitioned into very fine segments. In the conversion from CATIA to ABAQUS accuracy of the model is lost. The result being that ABAQUS is often unable to identify the interface of two adjacent curved segments. To work around this problem the panel is modeled flat. Proper boundary conditions are needed to account for the missing curvature. As indicated in Figure 3.7 the $\delta = 13.9mm$ for a panel of 471 mm wide. Perpendicular symmetry conditions will not hold anymore. Instead the symmetry planes are defined as if the structure would still be curved, intersecting at the interstage axis as can be seen in Figure 3.7. Any out-of-plane movement of the structure will still result in in-plane loads.

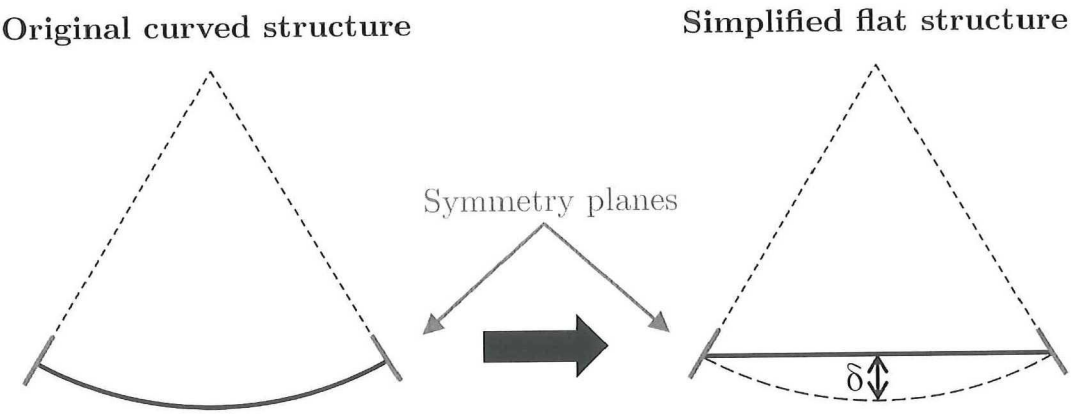

Figure 3.7: Symmetry boundary conditions for simplified, flat global model

The build-up of the laminate will consist out of multiple ply-drops. Modeling every ply drop, especially for thick laminates, will result in a very fine mesh. Guidelines indicate that no more than 0.5mm worth of plies should be dropped at the same location. To reduce the computational effort not every ply-drop is modeled but the laminate build-up is modeled with steps of about 0.5mm. The interface between the rib and the laminate is also simplified. In the real structure rib and laminate plies are interwoven. Modeling this would require modeling of the individual plies as demonstrated in [18]. Such a model would be required if detailed failure analysis is researched. This research is focused on the global elastic behavior

of the attachment zones and for that reason the accurate modeling of the overlap of rib and laminate plies is beyond the scope. For the same reason the ply drops in the ribs are not modeled. The local stress concentrations around the ply-drops will have a very limited effect on the global elastic behavior of the structure. Since the ribs are tapered part of the plies will be running under an angle. For large taper ratios the angle of the plies will not have a noticeable effect on the material properties.

The manufacturing process of grid-stiffened structures also bring complexities. A node is where multiple ribs cross. The fiber volume fraction at these overlap regions will be twice the nominal if there is no spreading of tows. At the nodes in this design two helical and a hoop rib cross, creating a complex zone with varying fiber volume fractions. For the same reason as for the rib-laminate interface the nodes are simplified to a single triangular area with layup [20/-20/90] ([helical/-helical/hoop]) as can be seen in Figure 3.8.

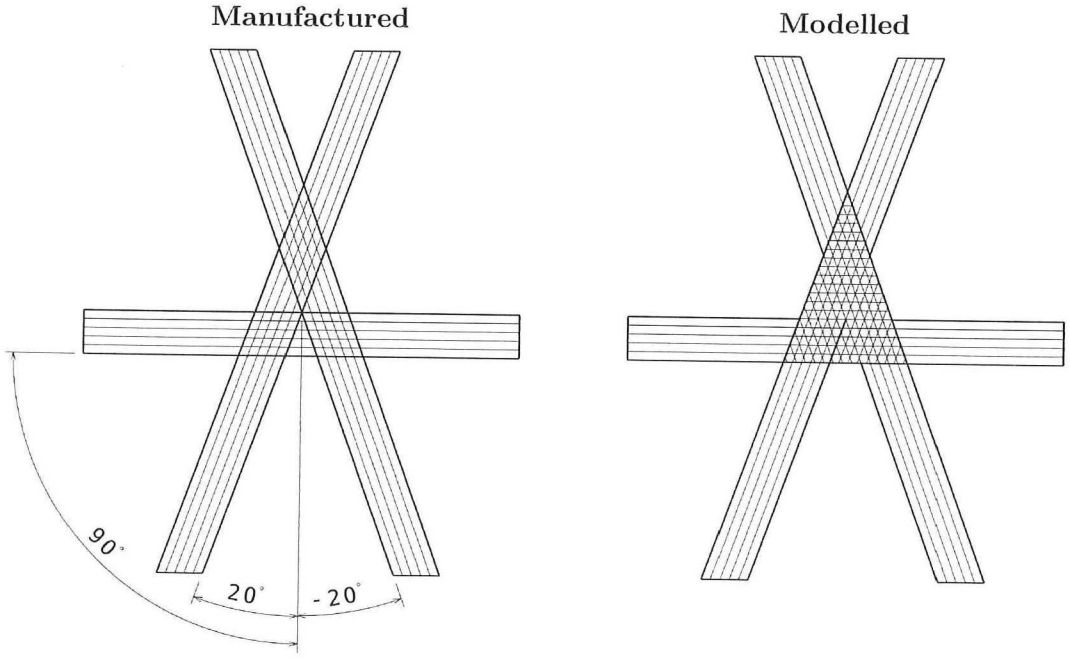

Figure 3.8: Geometry and material assignment of the node in the global model

Another manufacturing induced complexity is that of varying rib cross-sections. The final shape of the ribs is dictated by rubber tooling, as will be discussed in detail in Chapter 5. The use of soft tooling results in varying cross-sections along the ribs. A constant rib thickness, equal to the far-field rib thickness of 10mm, is used instead for the global analysis.

The last big simplification can be found in the modeling of the adhesive. Modeling of an adhesive can be very complex. To reduce complexity the adhesive is modeled as a linear isotropic material. It is assumed that the non-linear behavior of the adhesive does not influence the global elastic behavior of the entire structure. For detailed failure analysis of the adhesive more complex models will be needed. Assuming a linear behavior also ignores any plasticity of the adhesive. This results in a conservative approach of the adhesive itself.

3.4 Trend-studies

Optimization of the global attachment zone can be done multiple ways; trial and error or using an optimization strategy such as a genetic algorithm or a gradient based search. While trial and error might be fast, for problems with many parameters looking at random designs will most likely not lead to an optimum design. Making use of smart algorithms makes the chance of finding the optimum design much larger. The computational effort however also increases drastically. For a better understanding of the complex problem at hand trend-studies on the key design parameters are carried out. These should give insight on the effect on the global behavior for each design change. Design features that have an expected significant influence on the global performance of the structures are:

- **Bond-length** - The length in axial direction (z-direction in Figure 3.5) over which the laminate is bonded to the aluminum ring.
- **Laminate Length** - The length of the laminate in axial direction (z-direction in Figure 3.5) between the end of the panel and the first laminate ply drop.
- **Drop Ratio Laminate** - The rate at which plies are dropped in the laminate. This rate, also called taper ratio, is defined by the ratio of the distance between successive ply-drops and the dropped height. Design guidelines advise ratios of 10 to 20. [24, 26]
- **Drop Rate Ribs** - The rate at which plies are dropped in the rib.
- **Laminate Layup** - The orientation of the plies in the laminate. Design guidelines advise to orient plies which are in contact with the adhesive at 0° or ±45° to the loading direction. [24]
- **Laminate Thickness** - The total thickness of the laminate without the skin. The skin continues all the way to the edge of the panel. So the total thickness at the laminate section is the laminate thickness plus the skin thickness.

These parameters are visualized in Figure 3.9.

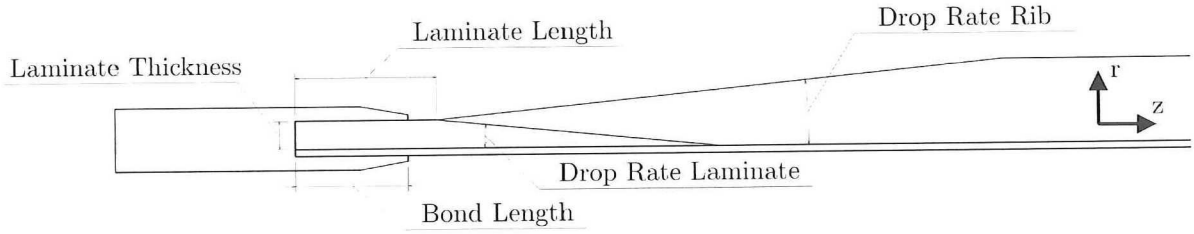

Figure 3.9: Design parameters used in the trend-studies

A baseline design has been created based on guidelines and basic calculations. To study the effects each parameter has a high and low value which are assessed individually. Every parameter is changed with respect to the baseline while keeping the baseline value for all the other parameters. The baseline, low and high values are given in Table 3.3. It should be noted that some of the high and low values are based on ease of modeling. Also the 0°

laminate layup is 0° dominated and is a multitude of [0/0/0/90]. The same is true for the 90° laminate layup which is 90° dominated and a multitude of [90/90/90/0]. The Quasi Isotropic (QI) laminate consists of [0/90/45/-45].

Table 3.3: Trend-study parameters with low, baseline and high values

Parameter	Low	Baseline	High
Bond-Length	20 mm	40 mm	60 mm
Laminate Length	41 mm	50 mm	60 mm
Drop Ratio Laminate	5	10	14
Drop Ratio Rib	5	10	15
Laminate Thickness	5 mm	10 mm	14 mm
Laminate Layup	0°	QI	90°

The high compressive mechanical flux, compared to the tension flux, (as discussed in Chapter 3.1) makes that the critical load case. Therefore all trend-study results are obtained for the compressive load case. Any conclusions on the effect of design changes are drawn on global behavior. Any local effects described are based on average values over multiple elements.

3.4.1 Baseline Design

The baseline attachment zone for the upper flange of the interstage has a total mass of 146.5 kg (for this calculation the attachment zone is assumed to be 0.65m in axial direction, see Figure 3.5). The aluminum ring and adhesive account for 46.5 kg. The adhesive clearly shows peak stresses near the ribs with shear stresses around 30 MPa on the skin side whereas the shear stresses at the grid side are only 16 MPa. The shear stresses fluctuate around 20% along the edge of the adhesive. The amount of load transfered through the adhesive into the aluminum flanges is roughly 51% and the remaining 49% is transfered through the laminate directly into the solid section of the aluminum ring. The resulting maximum von Mises stress in the aluminum flanges is 112 MPa (again at the skin side).

The critical region in the composite can be found in the laminate at the end of the ribs, where the strain values are just above half the maximum allowable strain values. This ratio of the actual strain divided by the maximum allowable strain will be called the failure index (maximum strain criteria). The failure index of the helical ribs is at 0.28 and the maximum strains can be found at the very end where the top rib plies are interwoven with the laminate, as indicated in Figure 3.10.

It is difficult to express the bending stiffness of the attachment zone in a single value. The out-of-plane displacement can be used as an indication for the bending stiffness. To this end the middle node closest to the laminate is used as a reference node (indicated in Figure 3.5). The out-of-plane displacement at this node is obtained even though the number on itself does not give much information. By comparing the displacements for different designs the relative bending stiffness can qualitatively be described. The total in-plane displacement is a measure for the membrane stiffness of the panel and is measured at the surface where the load is applied.

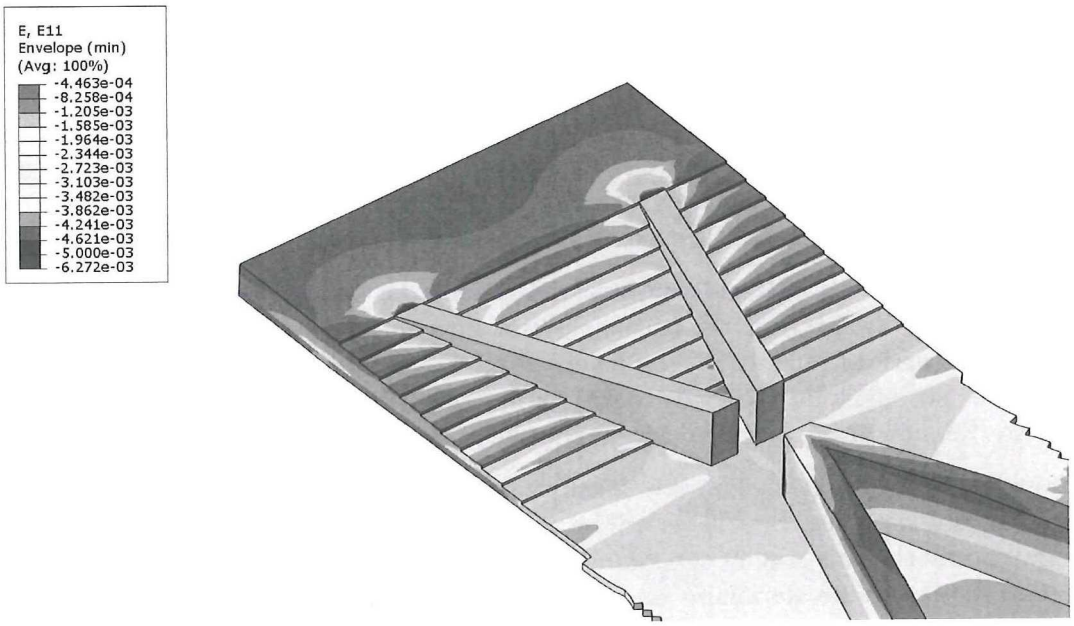

Figure 3.10: Compressive strain in fiber direction in laminate and helical ribs for baseline configuration

Table 3.4: FEM results for baseline design

Mass	146.5 kg
Adhesive shear stresses	30 MPa
Aluminum von Mises stresses	112 MPa
Laminate Failure Index	0.55
Helical rib Failure Index	0.28
Out-of-plane displacement	0.38 mm
In-plane displacement	1.70 mm

3.4.2 Bond Length

The easiest trend that can be observed for the bond-length, or for any parameter, is the influence on the mass of the structure. By simply extending the bond length the entire interstage becomes longer, which in reality will not be the case. The length of the aluminum ring is fixed, so any additional bond-length will reduce the length of the far-field composite grid. The mass of the far field structure is on average 152 grams per millimeter in axial direction. The average mass of the bond area (laminate, adhesive and aluminum flanges) is 445 g/mm. So for every additional millimeter of bond length the mass of the structure increases by 293 grams. Increasing the bond length to 60mm, increases the mass by 5.9kg (4%). Likewise a shorter bond-length will decrease the mass by 5.9kg (4%).

The most pronounced effect of the bond length can be seen in the adhesive itself. Shear stresses in the adhesive near the end of the ribs increase by roughly 10% for the short bond length. A decrease of roughly 3% can be observed for the long bond length. The shorter bond length does not allow for the loads to distribute, increasing the stresses at the edge(s) of the adhesive. Similar to the baseline design, the shear stresses concentrate near the helical ribs.

Although the stresses in the adhesive locally rise for a shorter bond length, the stresses in the aluminum ring decrease. Less loads will be transfered through the adhesive into the aluminum flanges and more loads stay in the laminate and are transferred by compression directly into the solid section of the aluminum ring. This effect can be seen in the compressive stresses in the adhesive which are shown in Figure 3.11. Roughly 42% and 55% of the load is transfered through shear by the adhesive for the short and long bond length respectively.

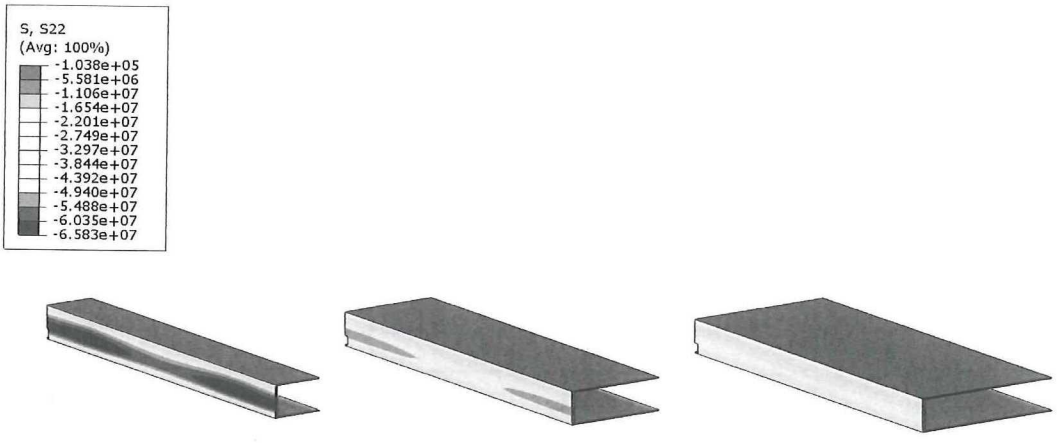

Figure 3.11: Stresses in the adhesive in the loading direction for the various bond lengths. Bond length from left to right: 20mm, 40mm, 60mm.

The longer bond length configuration shows 34% more out-of-plane displacement of the reference node. As described earlier the bonded laminate replaces part of the far-field grid. This laminate is relatively soft in bending compared to the far-field grid which results in more out-of-plane displacement for a longer laminate. Increasing the bond length also increases the maximum strains in the laminate and helical ribs by roughly 5%. The opposite is true for the shorter bond length, where a decrease in out-of-plane displacement and strain values is observed.

Table 3.5: FEM results for bond length trend study

Bond Length	20 mm		60 mm	
Mass	-5.9 kg	-4%	+5.9 kg	+4%
Adhesive shear stresses	33 MPa	+10%	29 MPa	-3%
Aluminum von Mises stresses	107 MPa	-4%	111 MPa	-1%
Laminate Failure Index	0.52	-5%	0.58	+6%
Helical rib Failure Index	0.27	-2%	0.29	+4%
Out-of-plane displacement	0.28 mm	-26%	0.51 mm	+34%
In-plane displacement	1.68 mm	-1%	1.73mm	+2%

3.4.3 Laminate length

As with the bond length, the mass change is observed first. The mass of the laminate depends on its thickness. For the baseline thickness of 10mm every millimeter of laminate will have a mass of 249 gram. Since the length of the aluminum ring is fixed, an increase of laminate length will decrease the length of the far-field grid section and vice versa. Reducing the laminate length to 41mm will decrease the overall mass by 1.8 kg (1.3%). An increase of 1.9 kg can be observed for the long (60mm) laminate length configuration.

Similar to what has been found for the bond length, increasing the length of the laminate will decrease the bending stiffness resulting in more out-of-plane displacement. For the 60 mm laminate an increase of 29% is found and for the 41 mm laminate the out-of-plane displacement of the reference node reduces by 24%.

The highest shear stresses in the adhesive for the baseline configuration are on the 'skin-side'. On average these shear stresses are twice as high as on the 'grid-side'. Reducing the laminate length has little effect on the shear stresses on the skin-side. However the shear stresses in the rib-side show a significant increase (+100%). A local increased strain field will be present near the ribs since these are the main load carrying elements. Normally the stresses will be distributed by the laminate, but if the adhesive is close to the rib high stresses will develop in the adhesive as well. This effect is shown in Figure 3.12.

Table 3.6: FEM results for laminate length trend study

Laminate Length	41 mm		60 mm	
Mass	-1.8 kg	-1%	+1.9 kg	+1%
Adhesive shear stresses	32 MPa	+7%	31 MPa	+3%
Aluminum von Mises stresses	110 MPa	-2%	113 MPa	+1%
Laminate Failure Index	0.64	+16%	0.58	+5%
Helical rib Failure Index	0.28	0%	0.29	+5%
Out-of-plane displacement	0.29 mm	-24%	0.49 mm	+29%
In-plane displacement	1.68 mm	-1%	1.73 mm	+2%

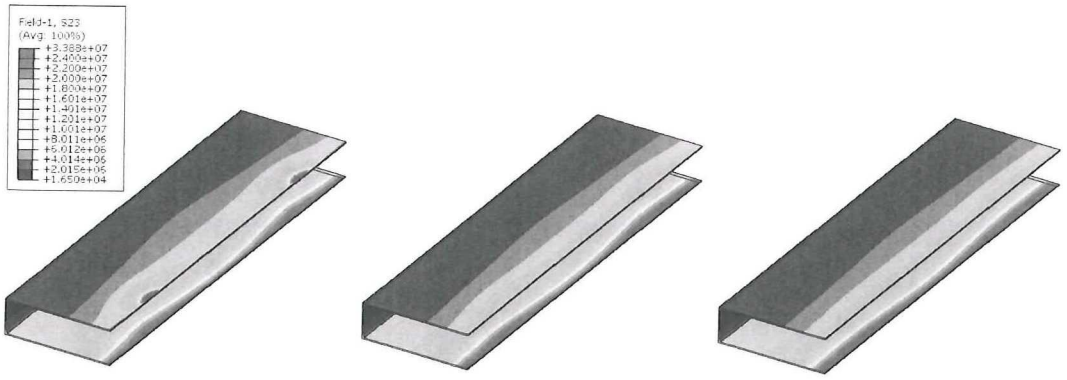

Figure 3.12: Shear stresses in the adhesive for the different laminate lengths. Laminate length from left to right: 41mm, 50mm, 60mm.

3.4.4 Drop Ratio Laminate

Dropping laminate plies over a shorter length will decrease the mass. Going to a drop ratio of 5 decreases the mass by 3.9 kg (2.7%) and an increase of 2.9 kg is observed for a drop ratio of 14.

However dropping plies also reduces the local membrane stiffness of the laminate, resulting in higher strains in the helical ribs (roughly 47%). One would expect a lower bending stiffness as well since laminate plies are dropped. However the exact opposite is true. The laminate plies that are dropped are replaced by the stiffer rib plies effectively increasing the bending stiffness.

The short build-up won't allow for proper stress distribution in the laminate. The strain levels at the rib-laminate interface increase as much as 52% as shown in Figure 3.13. The improper load distribution also results in an increase of the local shear stresses in the adhesive at both skin- and grid-side (roughly 17%). A more gradual build up of the laminate reduces the strain levels only about 15% and has almost no effect on the shear stresses in the adhesive.

Table 3.7: FEM results for drop ratio laminate trend study

Laminate Drop Ratio	5		14	
Mass	-3.9 kg	-3%	+2.9 kg	+2%
Adhesive shear stresses	35 MPa	+17%	29 MPa	-3%
Aluminum von Mises stresses	122 MPa	+9%	109 MPa	-3%
Laminate Failure Index	0.84	+52%	0.46	-16%
Helical rib Failure Index	0.41	+47%	0.25	-11%
Out-of-plane displacement	0.27 mm	-29%	0.46 mm	+21%
In-plane displacement	1.79 mm	+5%	1.65 mm	-3%

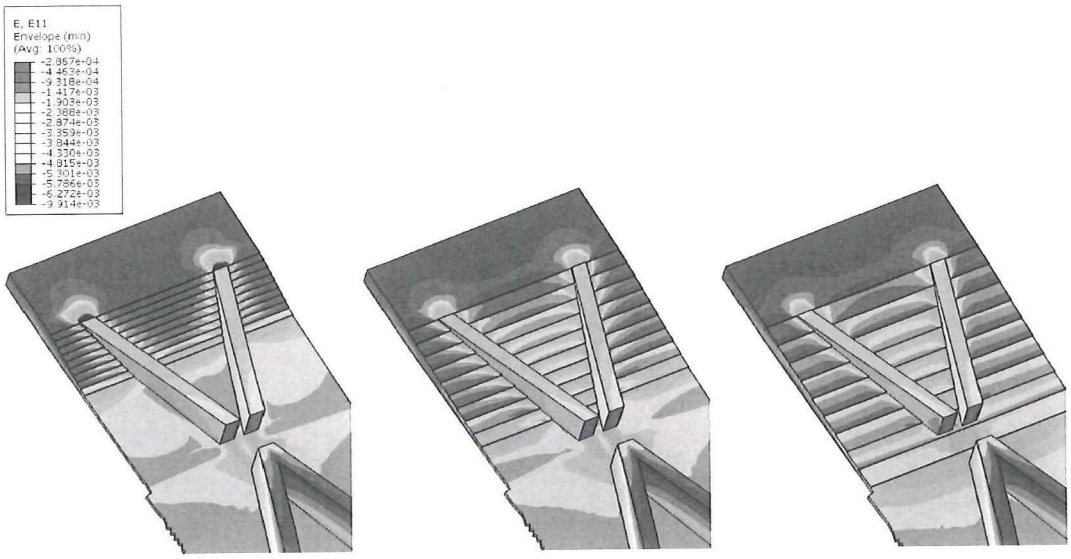

Figure 3.13: Strain in fiber direction at the rib-laminate interface for different laminate drop ratios. Laminate drop ratios from left to right: 5, 10, 14.

3.4.5 Drop Ratio Rib

Opposite of the laminate drop ratio, a drop ratio of 5 will increase the mass by 4.1 kg (2.8%). Ribs will run longer at the full height, increasing the mass. The ratio between mass savings and drop ratio is not linear, but a drop ratio of 15 still saves 3.3 kg (2.2%).

Starting to drop rib plies early directly results in a reduced bending stiffness. The out-of-plane displacement at the reference node shows an increase of 161%. For comparison the increased laminate length only resulted in an increase of 21%. Again the opposite is also true. A drop ratio of 5 will decrease the out-of-plane deflection at this reference node with 132%. A decrease of more than 100% means the panel starts to deflect in the opposite direction.

Not only does the early dropping of rib plies cause excessive out-of-plane deflections, it also slightly increases the strain levels in the helical ribs. The relatively small ribs however also carry less load. At the end of the ribs most of the load has been transferred to the laminate and the skin already. The critical region shifts from the end of the rib to the start of the laminate build-up, slightly (15%) reducing the strain values in the laminate. The exact opposite happens with the very steep drop (ratio of 5). All the loads accumulate at the end of the rib, creating a large stress concentration in the rib-laminate interface as can been seen in Figure 3.14. The stiff ribs in this case also pull more loads to the grid-side of the laminate, increasing the stresses in the adhesive on the grid-side and reducing the shear stresses at the skin-side. The net result is that the maximum shear stress in the adhesive is reduced by 13%.

Dropping rib plies early (drop ratio of 15) and transferring loads into the laminate and skin will result in a large decrease (31%) of shear stresses in the adhesive at the grid-side but only a small increase at the skin-side (10%). The stress concentration caused by the helical ribs is less severe as the ribs have a reduced stiffness.

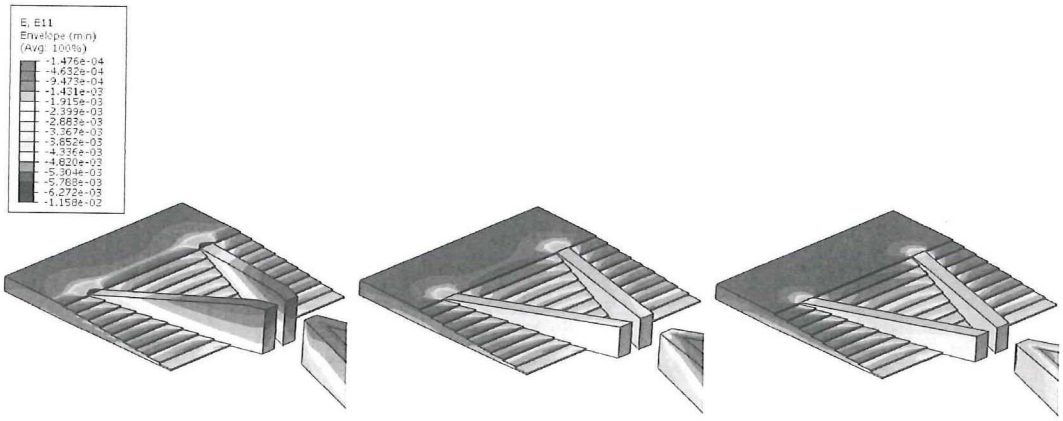

Figure 3.14: Strain in fiber direction at the rib-laminate interface for different rib drop ratios. Rib drop ratios from left to right: 5, 10, 15.

Table 3.8: FEM results for drop ratio rib trend study

Rib Drop Ratio	5		15	
Mass	+4.1 kg	+3%	-3.3 kg	-2%
Adhesive shear stresses	26 MPa	-13%	33 MPa	+10%
Aluminum von Mises stresses	106 MPa	-5%	115 MPa	+3%
Laminate Failure Index	0.89	+62%	0.47	-15%
Helical rib Failure Index	0.39	+38%	0.34	+22%
Out-of-plane displacement	-0.12 mm	-132%	0.99 mm	+161%
In-plane displacement	1.63 mm	-4%	1.80 mm	+6%

3.4.6 Laminate Thickness

Increasing the thickness of the laminate directly increases the mass of the laminate; by 3.2kg (2.2%) for the 14 mm thick laminate. Not only the thickness of the laminate itself increases, also the length of the laminate drop zone increases. Another secondary effect is the increased mass of the ribs. The total attachment zone mass increases by 13.6 kg (9.3%) for 4 mm thicker laminate.

A thinner laminate not only decreases the bending stiffness of the laminate section, also the bending stiffness of the ribs is reduced. The height of the ribs at the end is equal to the laminate thickness. The drop ratio of the rib is kept to the baseline value, resulting in less tall ribs. The resulting out-of-plane deflection is therefore large (89% increase at the node).

The strain levels in the laminate and ribs almost double for a laminate with a thickness of 5 mm. The increased strain in the laminate in the vicinity of the rib also doubles the shear stress in the adhesive. The opposite is found for a 14 mm thick laminate where the shear stresses in the adhesive almost halve. This effect can be seen in Figure 3.15.

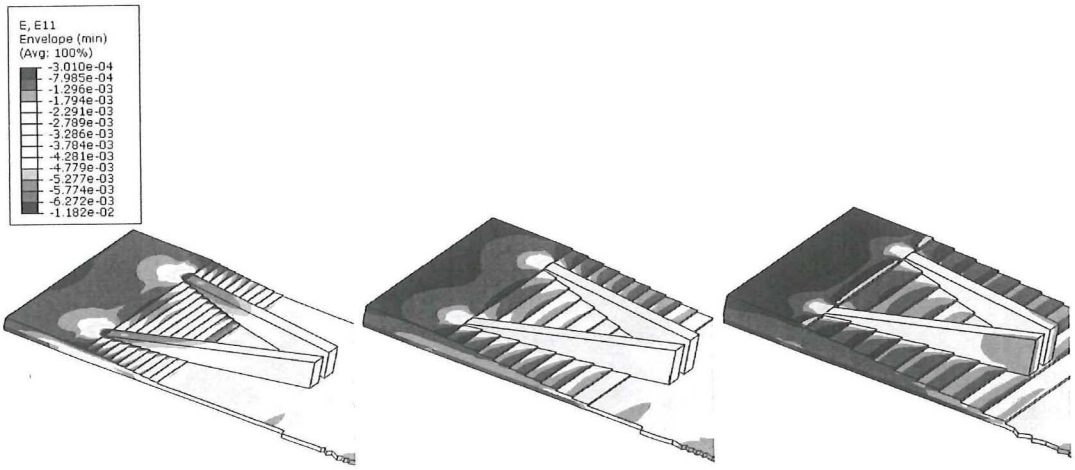

Figure 3.15: Strain in fiber direction at the rib-laminate interface for different laminate thicknesses. Laminate thickness from left to right: 5 mm, 10 mm, 14 mm.

Table 3.9: FEM results for laminate thickness trend study

Laminate Thickness	5 mm		14 mm	
Mass	-14.5 kg	-10%	+13.6 kg	+9%
Adhesive shear stresses	61 MPa	+103%	19 MPa	-37%
Aluminum von Mises stresses	141 MPa	+26%	102 MPa	-9%
Laminate Failure Index	1.02	+85%	0.41	-26%
Helical rib Failure Index	0.51	+84%	0.23	-18%
Out-of-plane displacement	0.72 mm	+89%	0.36 mm	-5%
In-plane displacement	2.05 mm	+21%	1.54 mm	-9%

3.4.7 Laminate Layup

Once the number of plies has been selected, the orientation of the plies in the laminate has no direct effect on the total mass of the structure.

The level of shear stress in the adhesive depends on the ratio of stiffness of the aluminum flanges and the composite laminate. A stiffer 0°-dominated laminate will transfer more loads trough the end of the laminate into the aluminum ring, similar to what has been described in Section 3.4.2, reducing the shear stresses in the adhesive. In this case only 46% of the load is transferred through shear by the adhesive. The reduction in shear stresses for the 0°-dominated layup is roughly 17% while the 90-dominated layup shows an increase of 17%. The stiffness ratio of the laminate and ribs also contribute to this reduction. A stiffer laminate pulls more loads from the ribs, reducing the stress concentration at the end of the rib. The opposite is observed for the 90°-dominated layup, which is a lot softer and the strains in the laminate at the end of the rib increase with as much as 90% as can be seen in Figure 3.16.

The laminate layup has only little effect on the bending performance and total in-plane displacement.

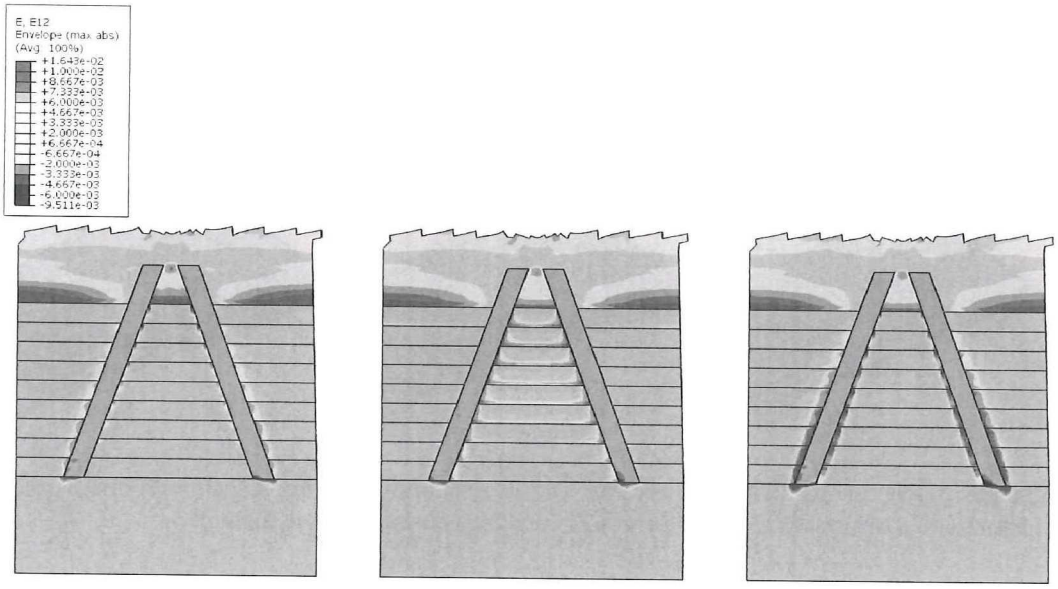

Figure 3.16: Shear strain at the rib-laminate interface for different laminate layups. Laminate layup from left to right: 0°, QI, 90°

Table 3.10: FEM results for laminate layup trend study

Laminate Layup	0°		90°	
Mass	±0 kg	±0%	±0 kg	±0%
Adhesive shear stresses	25 MPa	-17%	35 MPa	+17%
Aluminum von Mises stresses	100 MPa	-11%	112 MPa	±0%
Laminate Failure Index	0.59	+7%	1.05	+90%
Helical rib Failure Index	0.30	+6%	0.33	+17%
Out-of-plane displacement	0.41 mm	+8%	0.35 mm	-8%
In-plane displacement	1.64 mm	-4%	1.75 mm	+3%

3.4.8 Conclusions

From the trend studies presented in this chapter the following observations can be made:

- The length of the laminate can be minimized to decrease the mass a little (-1%) and increase the bending stiffness while only increasing the shear stresses in the adhesive on the grid-side.
- Reducing the bond length decreases the mass significantly (-4%) and only increases the shear stresses in the adhesive a little (+10%).
- A 0°-dominated layup will reduce shear stresses in the adhesive (-17%) without increasing mass or strain levels in the composite.
- The membrane stiffness of the laminate determines the loads transfer between rib and laminate and can be tailored to spread the load transfer over the entire laminate build-up. A stiffer, 0°-dominated, layup will tend to form higher strains at the start of the build-up whereas a softer, 0°-dominated, layup will create high strains at the end of the build-up.
- Increasing the drop ratio of the ribs can be used to lower the stress concentration at the end of the ribs and reduce stress levels in the laminate (-15%) and adhesive at the grid-side (-31%). A medium reduction of mass (-2%) can be achieved but out-of-plane displacement will be increased a lot (+161%).
- Reducing the drop ratio of the laminate will results in a medium mass reduction (-3%), but increases strain levels in the laminate a lot (+50%).
- The thickness of the laminate will drive the mass primarily by secondary effects. By reducing the laminate thickness the mass can be reduced by a lot (-10%) but strain levels in the laminate and ribs will increase a lot too (+85%). Shear stresses in the adhesive will double (+100%).

With the use of trend studies a better understanding of the complex problem is obtained. The effects of the key design parameters are identified. However finding the optimal combination of parameters will still require an optimization strategy.

Chapter 4

Verification Plan

Any conclusion drawn in Chapter 3 is only as good as the model used. To verify the global model the same modeling approach is used to create a model for the test samples. These will be tested to failure not only to provide information on the elastic behavior but also on the failure behavior. The test sample model will, like the global model, not be used to perform a detailed failure analysis. The model should indicate critical regions and be used to estimate the failure load based on simple failure criteria. The test samples will primarily be used to verify the global elastic behavior (both in-plane and out-of-plane) and load paths. By measuring strains and deflections at key locations and correlating these with the model, the global behavior can be verified. A model can be correlated and tailored such that it will match a single design. A model correlated with multiple designs will lead to more confidence that the model is versatile and can be used for optimization. For this reason two distinct different designs are manufactured and tested. By manufacturing two distinct different designs and thereby proofing feasibility, the versatility of the design concept on itself is also proven.

The most severe load case for the this design case is the compression loading of the interstage. Thus, all results presented in Chapter 3 are for the compressive load case and the test samples will be loaded in compression only.

4.1 Test Sample Design

To verify the global model the test samples have to reflect the global design. The geometry can be kept similar and hence the samples are based on the same layout: a grid stiffened skin with helical ribs running at 20° transforming into a laminate at the load introduction zone which is bonded to an aluminum 'ring'.

The geometry is scaled down by a factor two to reduce manufacturing time and costs. Scaling will not directly change the FEM model, but it is important for dimensioning thicknesses. On top of that, tolerances and ply thicknesses will have a bigger effect. To keep the time and cost down, the size of the samples is kept to a minimum which would still be representative for the full structure. The test samples will consist of four helical ribs and two hoop ribs.

The resulting structure allows for the full tapering of the ribs to be within the test section and contains a full cell which is not disturbed by any boundary or edge effects.

L-beams are glued at the sides of the panel to stabilize the skin at the open edge cells and prevent rib-skin separation at the end of the hoop ribs. It also mimics the symmetry boundary conditions in the model by resisting bending of the panel. The L-beams are terminated to prevent them from running into the aluminum ring. They end halfway the laminate build-up to prevent the stress concentration at the end of the L-beams to interfere with the adhesive. To reduce this stress concentration the L-beams are tapered as shown in Figure 4.1.

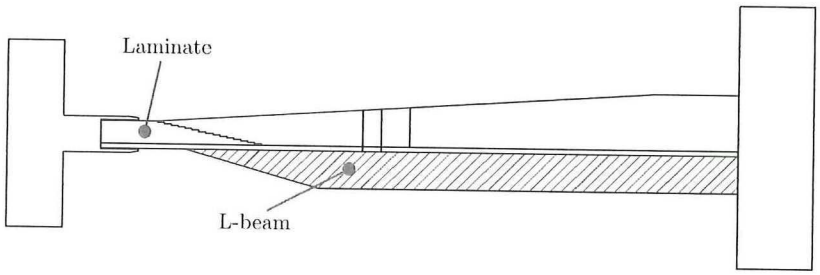

Figure 4.1: Side view of the test samples showing bonded L-beam termination

To stabilize the test sample, the aluminum ring is thickened at its base as can be seen in Figure 4.2. Similarly potting is added to the grid at the top. The thickness of the potting is roughly 20mm with the top hoop rib in the middle of the potting material. This reduces the risk of separation of the potting material. The resulting test sample configuration is shown in Figure 4.2.

From the trend-studies two critical areas can be identified; the adhesive and the rib-laminate interface. The first configuration, which will be called C1 from this point, has been designed such that the shear stresses in the adhesive are well below its shear strength (which is estimated to be around 30MPa). This should lead to failure in the composite part. The resulting design has a relatively thick laminate, consisting of 48 plies. As found in the trend studies a 0-dominated layup is preferable to reduce the shear stresses in the adhesive. To limit the amount of 0-plies stacked together the laminate is built up out of stacks of [0/0/0/0/45/-45]. To reduce weight the laminate has a drop ratio of five. As observed in the trend studies, this would increase the strains at the rib-laminate interface drastically. However the relatively thick laminate brings the strain levels down again. Due to the thick laminate the ribs are already quite tall, so a large drop ratio for the ribs will not affect the bending stiffness to the same extent as for a thin laminate and will still reduce the mass a little.

For the second configuration, C2, the shear stress in the adhesive is allowed to exceed the shear strength. However the design should not result in a stupid design, but should be competitive to the first configuration in terms of final strength. The design relies on plasticity of the adhesive and should result in a lighter design. To this end C2 has a thin laminate, consisting of 30 plies built out of the same stacks of [0/0/0/0/45/-45]. As shown in the trend studies the strain levels in the laminate will increase drastically for a thin laminate, especially at the end of the rib. A 0°-dominated layup will result in a better load distribution over the rib-laminate interface. It will also reduce the shear stresses in the adhesive. To lower the strain values in the laminate, the drop ratio of the laminate is 10. The mass penalty paid will be less for a

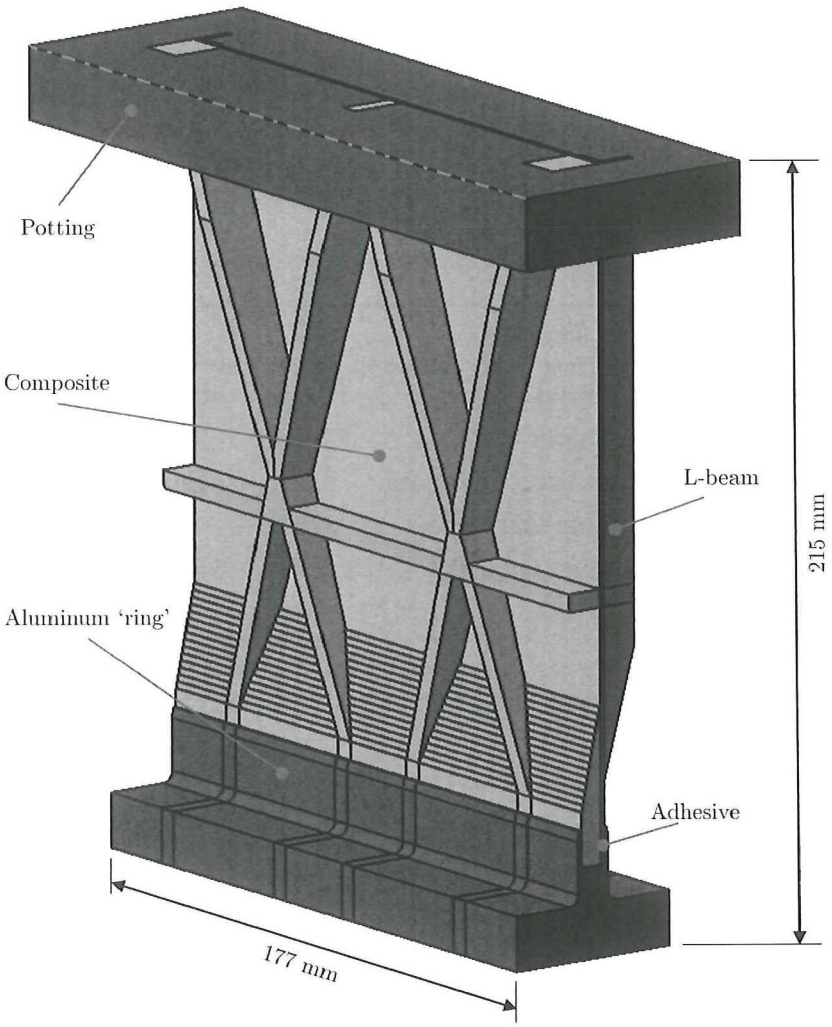

Figure 4.2: Test-sample design for the C1 configuration

thinner laminate, so the mass can be kept low. A rib drop ratio of 12 has been chosen such that the axial location of the full rib is the same as for the C1 configuration.

The bond length is 10mm for both configurations. This has been chosen for practical reasons. The upper limit for the length is based on a manufacturing constraint. The laminates are relatively thin and machining deep narrow slots whilst still achieving tight tolerances, becomes difficult. For a very short bond length, any defect will have a large influence on the performance and hence a longer bond length is needed for creating consistent samples.

From the trend studies is observed that a small distance between the adhesive and the laminate build-up (or build-down) is sufficient to prevent excessive stress concentrations in the adhesive. However the top plies of the ribs are interwoven with the laminate for about 3mm. To prevent a local build-up to interfere with the adhesive, the laminate length is thus set to 15mm.

The final design parameters for the test sample configurations are summarized in Table 4.1.

Table 4.1: Design parameters for test sample configurations

Parameter	C1	C2
Bond Length	10 mm	10 mm
Laminate Length	15 mm	15 mm
Drop Ratio laminate	5	10
Drop Ratio Rib	15	12
Laminate Thickness	6.1 mm	3.8 mm
Laminate Layup	0°	0°
Mass composite	214.3 g	193.1 g

4.2 Test Sample Model

4.2.1 Modeling Approach

All components of the actual test sample are modeled; potting, L-beams, aluminum ring, adhesive and composite panel. That means the only boundary conditions are the ones at the two interfaces with the test bench, being the bottom side of the aluminum ring and the top surface of the potting material. The bottom side of the aluminum ring is fixed in axial (loading) direction and the load is applied at the top surface of the potting.

The same simplifications as for the global model (see Section 3.3.2) are made. The global model was modeled linear to allow for fast iteration. The non-linear effects will not change the trends observed but might not give the correct absolute value. Since only limited amount of test sample models have to be run, a non-linear model will better capture the out-of-plane effects of the test-sample and allow for better correlation with the test samples.

4.2.2 Results

To group the results the sample is divided in five key regions; adhesive, aluminum, laminate (with tapering), ribs and skin. For each region the maximum failure index is calculated. For the composite regions this is based on the maximum strain failure criterion. For the adhesive the shear stress is divided by the shear strength and for the aluminum the von Mises stress is divided by the yield strength. The failure indices at 93kN compressive load are presented in Table 4.2. The compressive load of 93kN is based on the compressive flux of 1050kN/m, which has been presented in Section 3.1, multiplied by the width of the sample and then divided by two to account for the scale. For each region the load that will lead to failure can also be obtained with the model and is presented in Table 4.3.

Table 4.2: Failure index indicated by FEM at 93kN compression load

Location	C1	C2
Adhesive	0.77	1.16
Aluminum	0.48	0.62
Laminate	0.53	0.61
Ribs	0.31	0.37
Skin	0.59	0.61

Based on the models the adhesive will show failure first for both configurations. However as already mentioned in Section 3.3.2 the adhesive is modeled without plasticity. So even if the shear stress exceeds the shear strength in the model, the actual stress might have been relieved by the adhesive deforming plastically. The same can be said about the aluminum, where in the case of C2 yielding will start before any composite area shows failure. Local plastic deformation of the aluminum will only redistribute the loads a little but will not directly lead to complete failure of the test sample.

Table 4.3: Compression load required for failure to occur at key regions

Location	C1	C2
Adhesive	117 kN	82 kN
Aluminum	185 kN	142 kN
Laminate	172 kN	147 kN
Ribs	200+ kN	189 kN
Skin	163 kN	153 kN

From the compression loads required for failure to occur in the key regions it can be concluded that the adhesive will fail first. If we would ignore the failure in the adhesive and aluminum, the next critical region for C1 can be found in the skin. The shear strains exceed the maximum strain at 163kN at the start of the laminate build-up between the helical ribs as can be seen in Figure 4.3. This failure mode is closely followed by failure at the rib-laminate interface at 172kN, as shown in Figure 4.4. The FEM model of C2 indicates failure to start at 147kN at

the rib-laminate interface, similar to the second failure mode of C1.

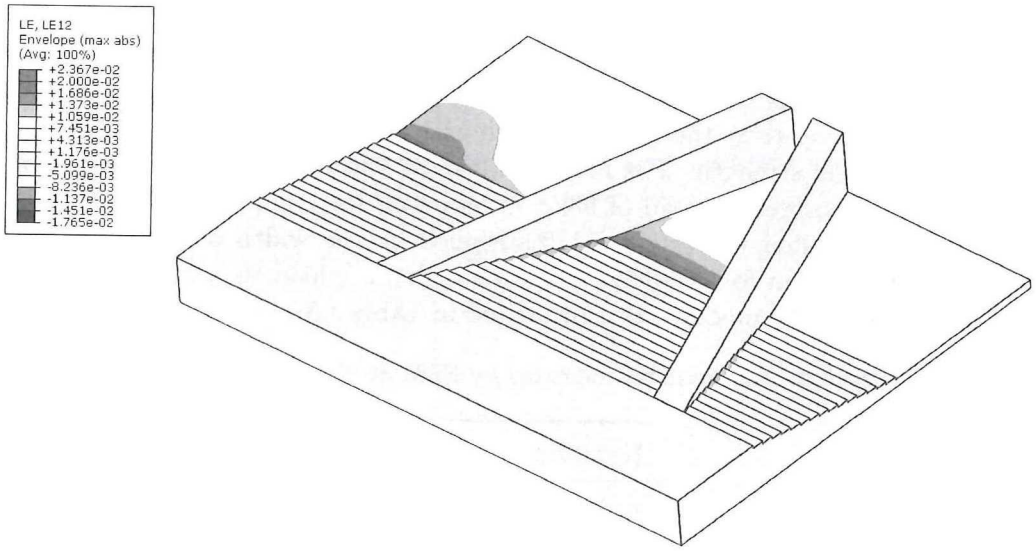

Figure 4.3: Shear strain plot for C1 indicating failure located at skin

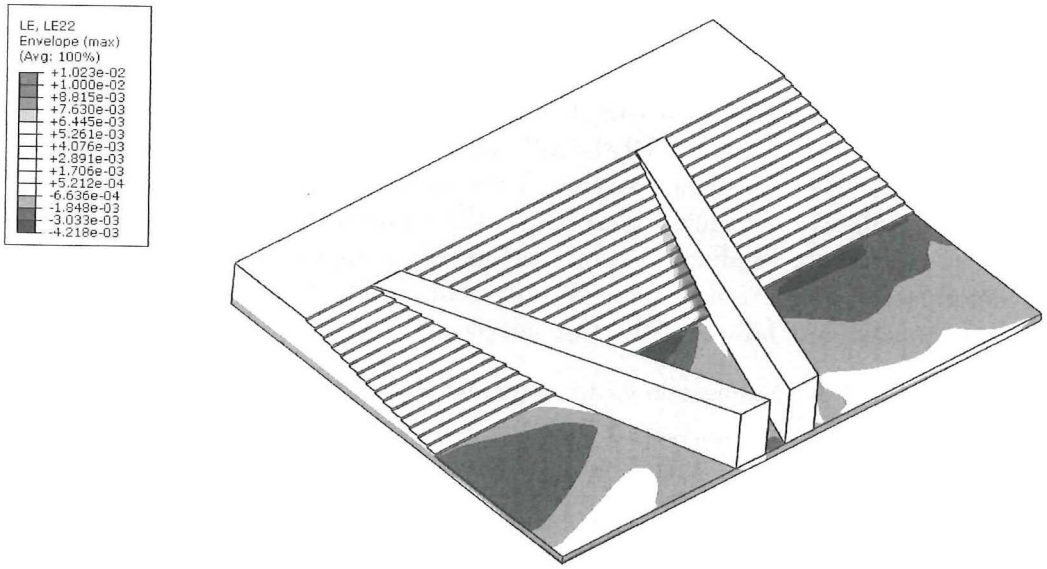

Figure 4.4: Transverse strain plot for C1 indicating failure located at rib-laminate interface

The expected failure locations, failure loads and total in-plane displacement at failure can be found in Table 4.4. For both configurations it is assumed that the adhesive might plastically deform but this will most likely not result in collapse of the sample and as such is not defined as failure.

Table 4.4: Expected failure location, failure loads and total in-plane displacement

	C1	C2
Failure location	skin	laminate
Failure load	163 kN	147 kN
Displacement at failure load	0.93 mm	0.93 mm
Displacement at 93 kN	0.51 mm	0.57 mm

Chapter 5

Manufacturing

Manufacturing can have a huge influence on the performance of a structure. For better understanding and correct interpretation of the test results, presented in Chapter 6, the key steps in the manufacturing are described in this chapter. First the different manufacturing steps of the composite panels are described, followed by a detailed discussion on the quality of the manufactured samples and how the quality is influenced by the different manufacturing steps. The implications the quality has on the model correlation will be discussed in Chapter 7. In the last section of this chapter the assembly steps are described. The manufacturing of samples has been carried out at the Delft Aerospace Structures and Materials Lab (DASML) and in the D:DREAM hall of the TU Delft.

5.1 Manufacturing Approach Composite Section

The composite grid is built out of CFRP prepreg tapes, which are placed manually in the correct pattern. The prepreg used requires cure in an autoclave. Tooling is required to shape the grid and prevent the grid from collapsing under the autoclave pressure. The tooling that gives the grid its shape consists of rubber pieces that will be placed between the ribs. The rubber tooling will expand in the autoclave and provide compaction of the ribs.

In initial manufacturing trials it has been observed that the edges of a panel show far lower quality due to shifted fibers or resin accumulation. To make sure the test area is not affected by these edge effects, additional cells are provided which are trimmed off as shown in Figure 5.1.

5.1.1 Rubber Tooling

A silicon rubber has been chosen for the expansion tooling for its good thermal expansion properties and ease of manufacturing. The rubber tooling is molded in 3D printed molds. Using a 3D printer allows for the molding of complex shapes with good accuracy at low cost. An example of such a mold and the rubber tooling can be seen in Figure 5.2. All rubber

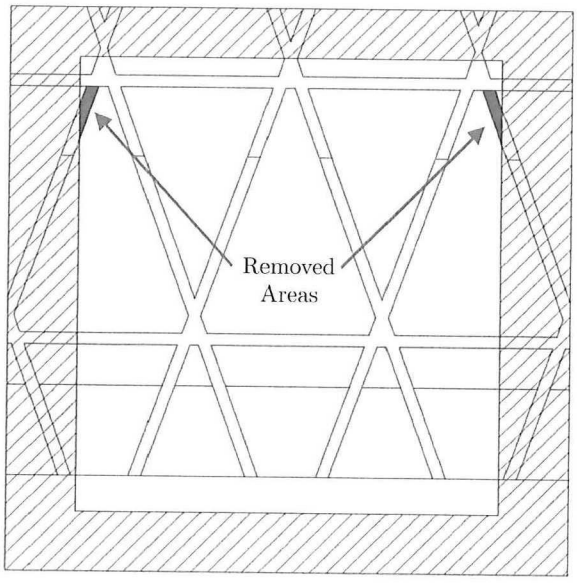

Figure 5.1: Layout composite panel with test-sample outline

tooling is post-cured to assure full cure to eliminate silicon molecules interacting with the resin and to assure the correct hardness. During initial manufacturing trials it was observed that not post-curing the rubber will result in indentation of the rubber and rubber tooling sticking to the composite.

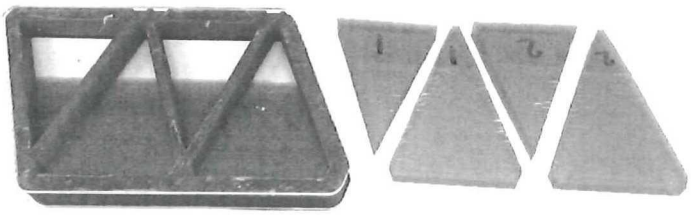

Figure 5.2: 3D printed mold for rubber expansion tooling

5.1.2 Layup

The ribs are built with CFRP tapes, which are slightly wider than the final rib width. In the autoclave the rubber tooling will expand and compress the ribs. The ribs will rise and reach the final required height. For this research the tapes are cut from a 300mm wide prepreg UD roll using a fiber cutter. Cutting tapes from a wide roll allows for the use of a specific tape width. The required tape width depends on various parameters such as the final required rib width, cell size, expansion tooling properties, cure temperature and cure pressure. So being able to select any tape width does not limit the design space. The test samples required tapes of 7.25mm wide, which was based on the required final width of the ribs and expansion of the rubber tooling. Tapes with this width are not readily available but can be ordered at an increased cost. The accuracy of the Gerber fiber cutter at the DASML lab assured the

width of the tapes was within ±0.1mm. By picking the plies randomly the ribs will have both narrower and wider tapes, averaging out the inaccuracy over the cutter.

A template with the outlines of the ribs is used to align the rib plies during layup. The taper of the ribs require plies to be dropped at a specific location. These locations are indicated on this template as well. The rib ply drops are kept internal and are alternated with continuing rib plies to prevent potential splitting of the rib. To ensure proper load transfer capabilities the fibers of the helical ribs are interwoven with the laminate plies. The layup can be seen in Figure 5.3.

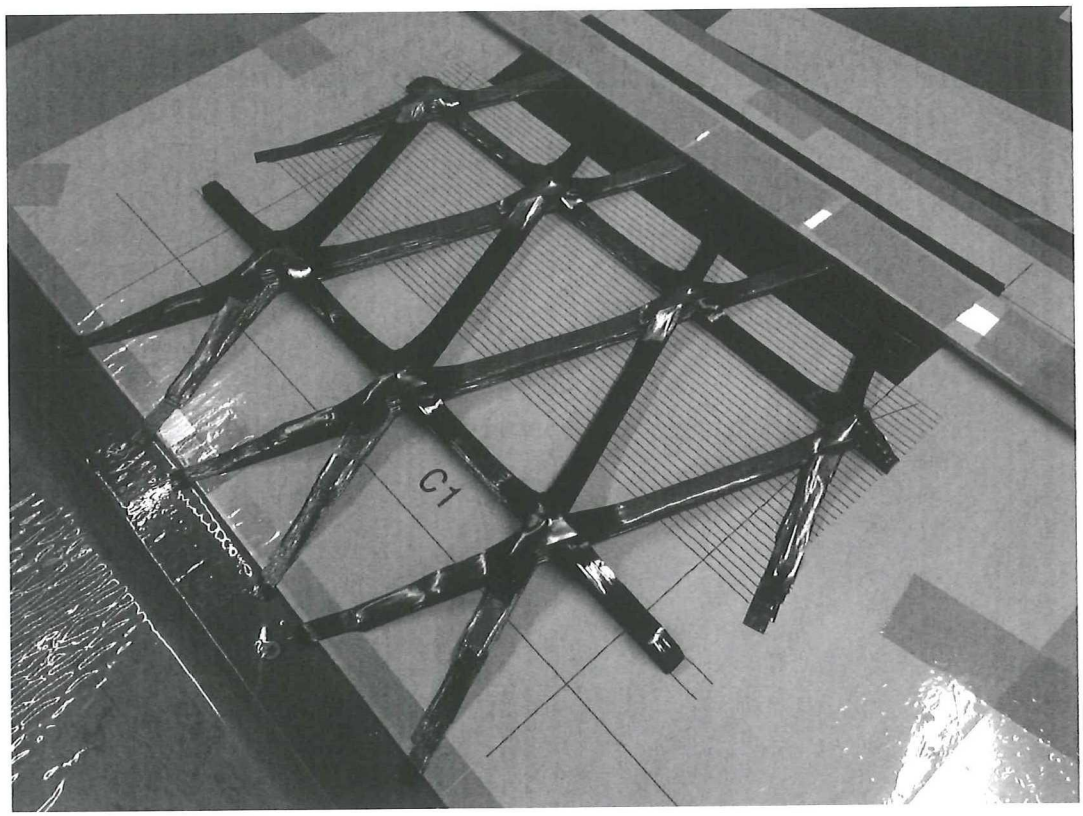

Figure 5.3: Layup of test-sample

During layup the ribs that cross each other will form nodes; local build-ups of plies. At these nodes twice the material is placed. That also means the nodes will start to build-up height twice as fast as the ribs between the nodes. The ribs in the test samples consist of 82 plies, each of which is 0.152mm thick uncured. The node containing twice the number of rib plies results in an uncured height of 25.0mm while the rubber tooling is only 14.3mm high. Manufacturing trials have shown that fibers sticking above the rubber might end up being trapped between the rubber and the caul plate. To prevent rib plies from ending up on top of the rubber the plies are placed between the rubber and only the nodes will stick above the rubber as can be seen in Figure 5.4.

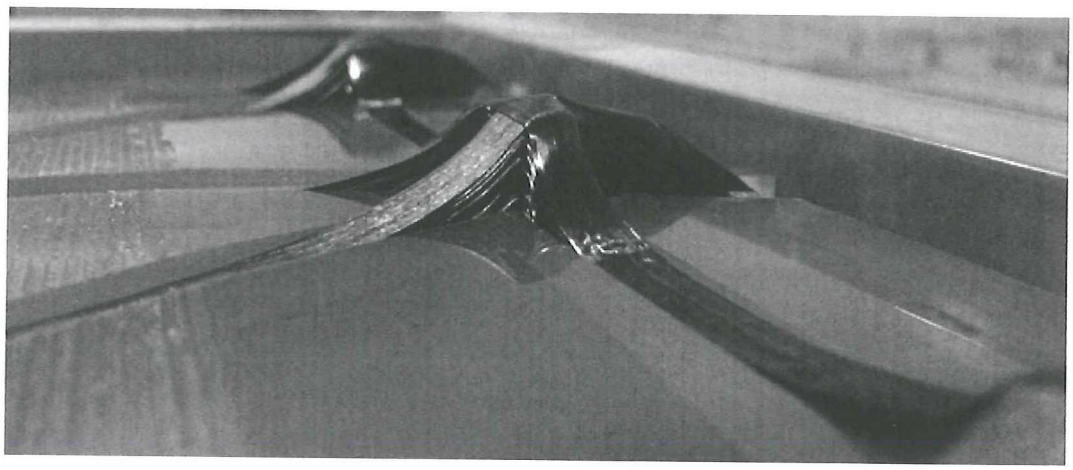

Figure 5.4: Finished layup showing node sticking above rubber expansion tooling

5.1.3 Cure

Once layup is finished the rubber tooling can be inserted in the grid. Metal dams are placed around the test sample to define the outer shape. Bundles of dry fibers are placed underneath the dams to provide a path for air to escape. Finally a caul plate is placed on top creating a flat surface on the part. The layup with the rubber expansion and autoclave tooling can be seen in Figure 5.5.

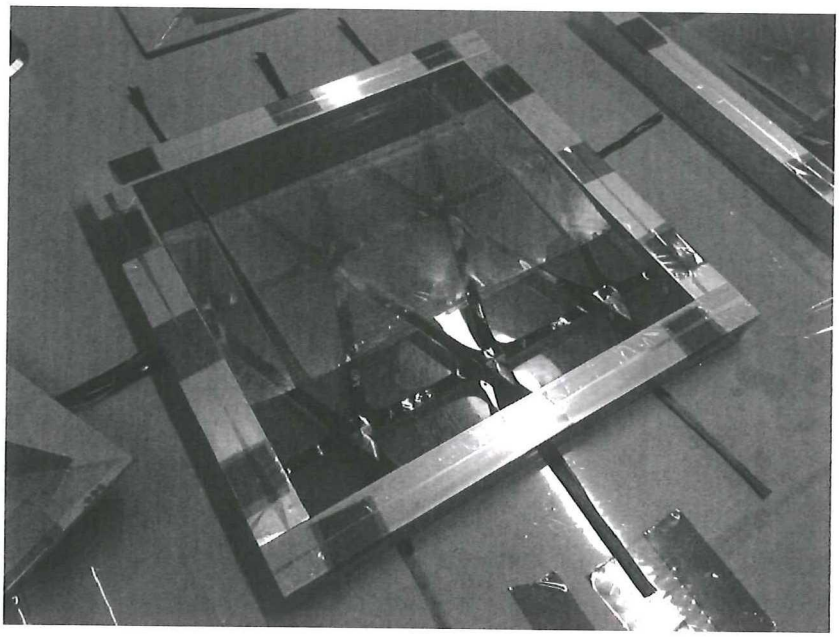

Figure 5.5: Finished layup with rubber expansion and autoclave tooling

The cure cycle is defined by the supplier and material property data is based on samples cured at this cycle. So for a correct correlation between the FEM models and the test samples it is important that the samples are cured at this exact same cure cycle. Any deviation might result in under- or over-cured sections resulting in affected material properties. The autoclave

cycle is controlled by a thermocouple in the autoclave free air and not in the part. So the temperature of the air in the autoclave might be correct, the presence of the rubber tooling and relatively thick composite sections might cause the temperature inside the product to be different. Thermocouples were embedded in one of the feasibility study samples (shown in Figure 3.4). These samples were full scale, meaning 30mm by 10mm ribs and a 10mm thick laminate. The thermocouple readings are presented in Figure 5.6 together with the autoclave thermocouple reading. The thermocouples in the product show a clear thermal lag of about 15 minutes. After the autoclave has reached the temperature set-point it takes 15 minutes for the sample to reach this same temperature. However when the autoclave starts heating again or cooling this same delay of 15 minutes can be observed. This means that the product has felt the same overall cure cycle and is cured well. Since the test samples are a lot smaller than the feasibility samples it is assumed that these will be cured at the correct cure cycle as well.

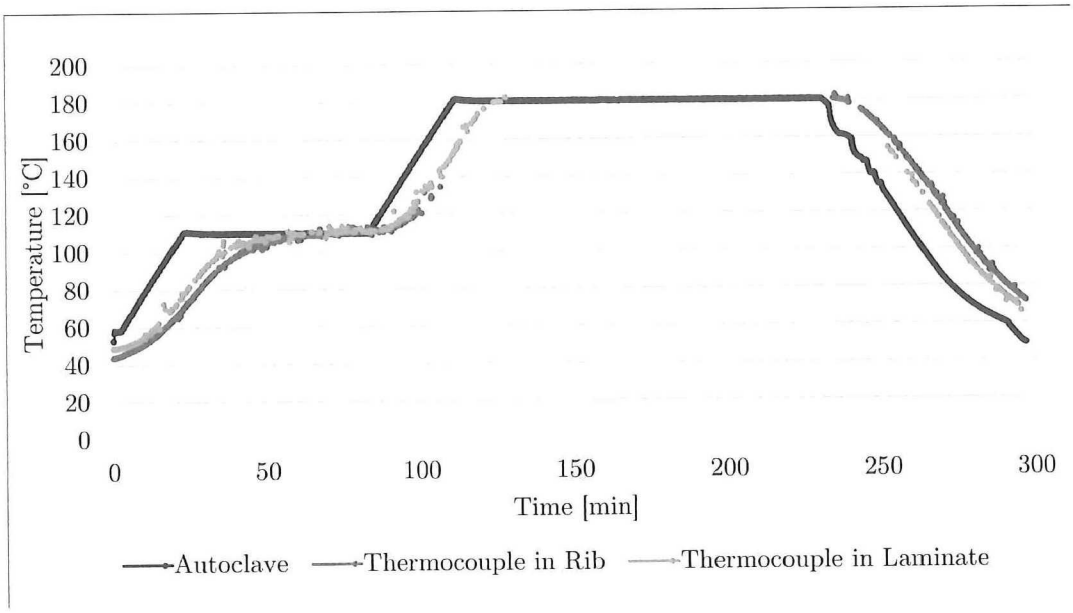

Figure 5.6: Thermocouple measurements showing full cure cycle in GS test sample

5.2 Quality

After manufacturing the quality of the test samples is assessed and presented in this section. It should be noted that all quality assessments are done after trimming but prior to assembly.

The panels are slightly heavier than estimated by the models. The masses can be found in Table 5.1. A lightweight solution requires good predictions of mass. Therefore the difference in mass will be explained in the following sections.

Table 5.1: Total mass of composite section test samples

	Estimated	Measured	Difference
C1	214 g	226 g	+5.6%
C2	193 g	203 g	+5.1%

5.2.1 Visual Inspection

First the samples are inspected visually. Small imperfections can be found, such as small particles on the surface caused by cutting of the fibers at the side of the layup. The samples also show places with imprint of the rubber tooling. The rubber tooling is molded in 3D printed molds which are build up out of small layers. The layers will leave an imprint in the rubber, which on its turn leaves an imprint in the sides of the ribs. These defects are purely superficial as can be seen in Figure 5.7. Since these defects are only superficial they are expected to have limited, if any, effect on the performance of the samples.

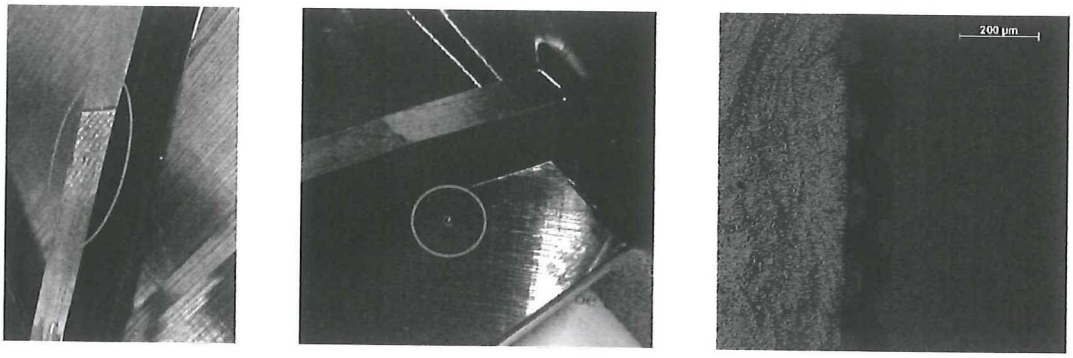

Figure 5.7: Small superficial imperfections showing imprints by the rubber tooling and small co-cured particles

Even though an attempt has been made to prevent the shift of rib plies, described in Section 5.1.2, some shift can still be observed at the nodes. The top ply seems to have shifted creating an overhang as can be seen in Figure 5.8. Due to the nodes sticking above the rubber pre-cure (see Figure 5.4) the top plies have been trapped on top of the rubber tooling during cure.

Another defect that can be found at the node is resin pockets. On the top of the ribs, close to the node resin accumulates. To prevent the shift of fibers during layup the rib plies are

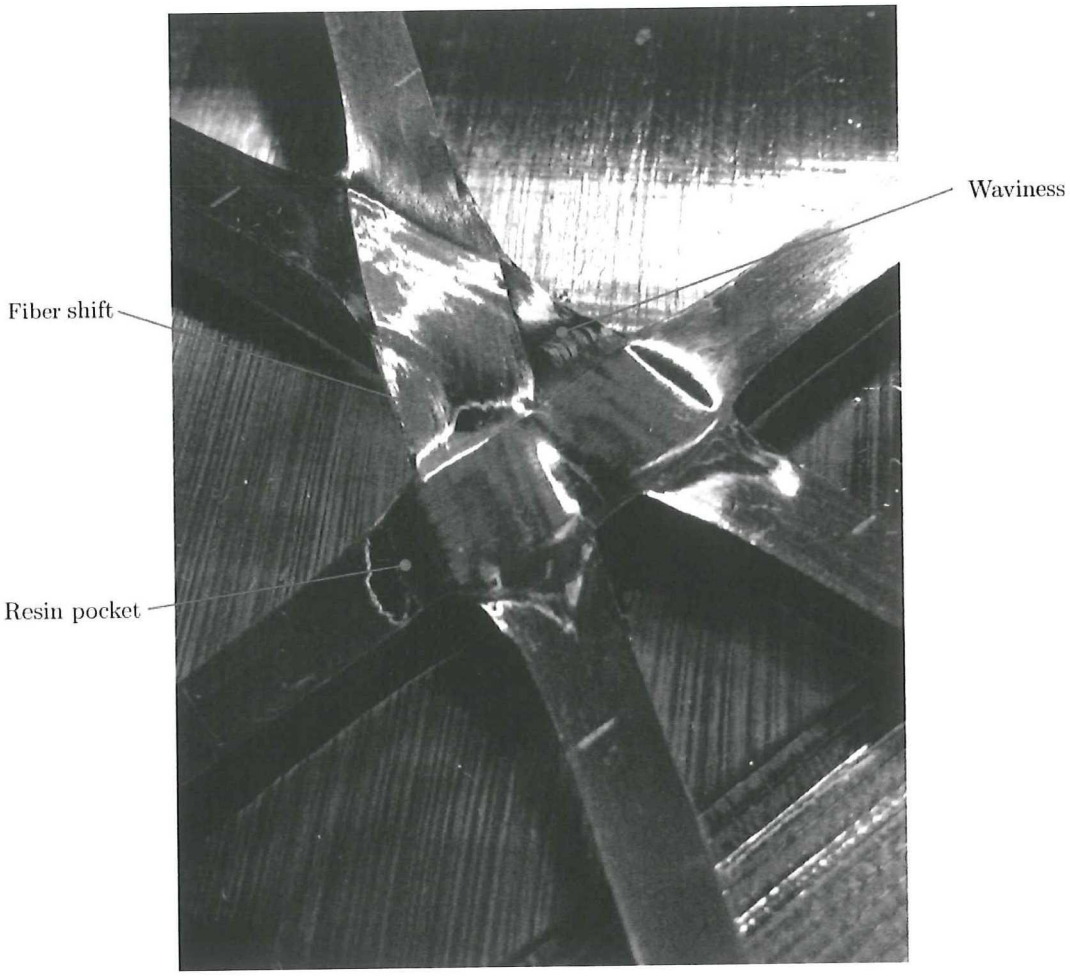

Figure 5.8: Node clearly showing shifted plies, waviness and resin pockets

pressed down in between of the nodes where the build-up of fibers is twice that of the ribs themselves. Both helical and hoop ribs are continuous, which means the fibers which are placed last will have a larger length than the fibers that are placed first. This can be seen clearly in Figure 5.9. The rib plies do need some additional length to allow for sideways movement, since the ribs will be compressed by the rubber. But this sideways movement is relatively small compared to the rib length so the additional required length to account for this is negligible. For the full height hoop ribs the top fibers are estimated to be 15% longer than the bottom fibers. This means that on average the fibers will be 6% too long. During cure the ribs will start to rise and the fibers will start to form waves, resulting in waviness and resin pockets at the nodes, which are shown in Figure 5.8. These excessive fibers add up to roughly 3.5 grams for the entire panel, which partially explains the additional mass of the test panels.

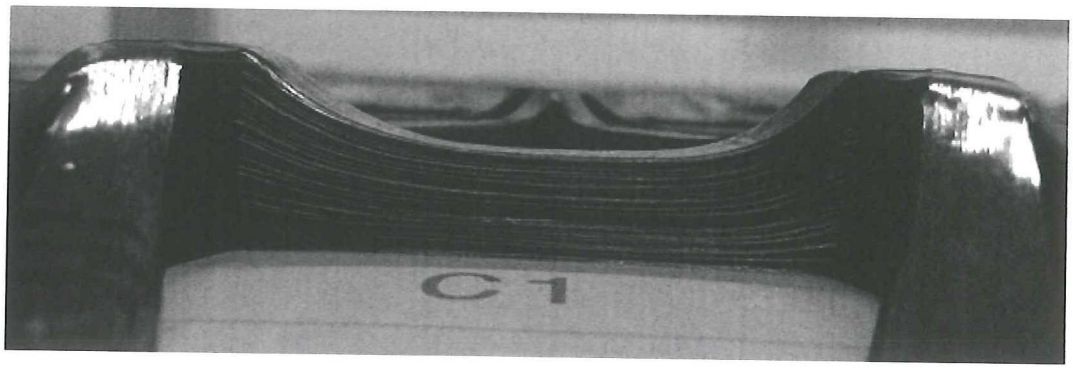

Figure 5.9: Uncured hoop rib and node

5.2.2 Dimensions

The dimensioning of the rubber tooling is based on a 2D expansion model. This model however cannot predict accurately the expansion of a triangular rubber tool. While it was assumed that an expanded triangle would remain triangular the test sample show thinner ribs in between nodes and wider ribs near the nodes. For the ribs in the far-field grid this is a very local phenomenon and only noticeable within a few millimeters from the nodes. The ribs in between the nodes and laminate however are wider than predicted and the ribs on the laminate build-up are almost the laid up width as can be seen in Figure 5.10. The height of the rib is close to the expected height, so the cross-sectional area of this rib section is significantly, 18%, bigger than intended. The dimension measurements are summarized in Table 5.2 and Table 5.3. It should be mentioned that the height of the helical ribs has been measured at the full height section between the taper and potting. At the taper of the ribs no accurate height measurements could be done. A constant taper has been assumed.

The cross-sectional area of the helical ribs near the potting end is only 2% bigger but on average (including the helical ribs on and near the laminate build-up) the ribs are 5% bigger than designed. In Section 5.2.1 it has been shown that the fibers in the ribs are 6% too long on average and this could explain the bigger ribs. The skin and laminate sections are slightly thinner on average (2.5%) so the increased volume of the ribs is not caused by thicker plies.

The dimensions of the nodes in the testpanels are slightly larger than modeled. In the model

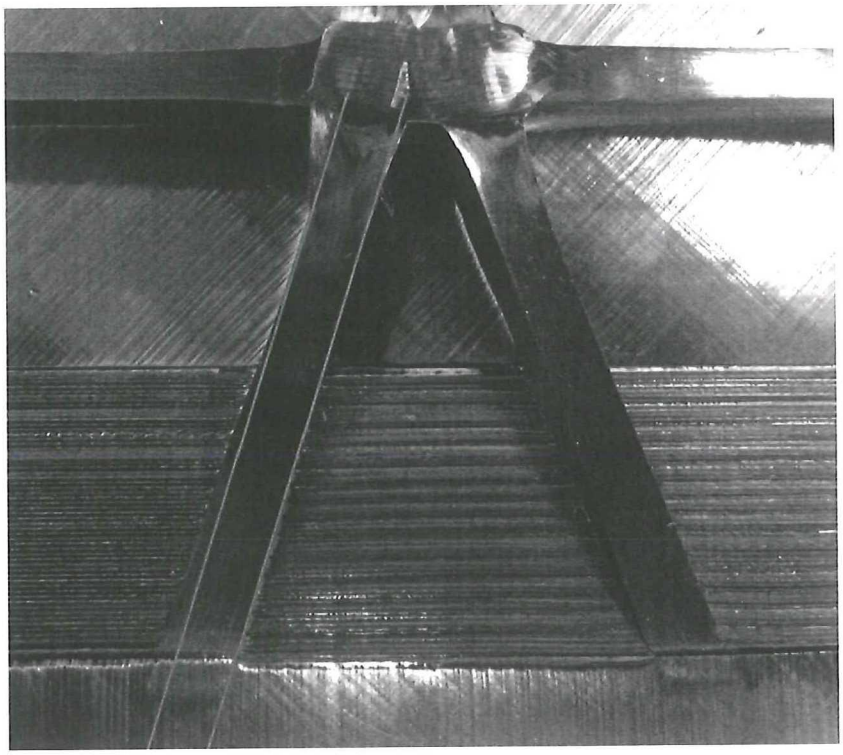

Figure 5.10: Helical rib on laminate build-up showing little compression from rubber tooling

Table 5.2: Dimensions C1 panels at key locations

	Nominal	Average	Standard Deviation
Skin thickness	1.27 mm	1.24 mm	0.02 mm
Laminate thickness	7.37 mm	7.19 mm	0.06 mm
Helical ribs width	5.00 mm	5.26 mm	0.10 mm
Helical ribs at laminate build-up width	5.00 mm	6.24 mm	0.38 mm
Hoop ribs width	5.00 mm	5.23 mm	0.13 mm
Helical ribs height	15.00 mm	14.43 mm	0.05 mm

Table 5.3: Dimensions C2 panels at key locations

	Nominal	Average	Standard Deviation
Skin thickness	1.27 mm	1.25 mm	0.02 mm
Laminate thickness	5.08 mm	5.01 mm	0.04 mm
Helical ribs width	5.00 mm	5.23 mm	0.13 mm
Helical ribs at laminate build-up width	5.00 mm	6.00 mm	0.27 mm
Hoop ribs width	5.00 mm	5.51 mm	0.08 mm
Helical ribs height	15.00 mm	14.63 mm	0.06 mm

it was assumed the tapes in the nodes would be compressed by the rubber tooling. This however happens only little. The model does not take into account that tapes in the node overlap, resulting in twice the material locally. All the nodes combined are approximately 3 grams heavier than modeled. Also the overlap of rib and laminate plies at the rib-laminate interface are not taken into account by the model. Although being small, all theses overlap pieces add up to 1,5 grams and 1 gram for the C1 and C2 configuration respectively.

While the rib and laminate plies overlap at the interface, no significant increase in laminate thickness is observed. That means that overlapping of rib and laminate plies over a finite length does not result in excessive build-up of plies.

5.2.3 Fiber Volume Fractions

As discussed in Section 5.2.2 the ribs are bigger in volume than predicted. While a larger volume might indicate resin rich areas, Fiber Volume Fraction (FVF) tests show quite consistently high FVFs throughout the samples. The FVF is determined based on the density at various locations and the densities of the two constituents. According to the data-sheet of the supplier the FVF should be 59.9%. The measured FVFs are tabulated in Table 5.4 and their locations are indicated in Figure 5.11.

Table 5.4: Fiber Volume Fractions at key locations

Location	FVF ±0.2%
1. Skin mid cell	64.1 %
2. Skin edge cell	63.9 %
3. Hoop rib	63.9 %
4. Helical rib halfway mid cell	63.4 %
5. Helical rib between node and laminate	62.4 %
6. Helical rib on laminate	63.9 %
7. Laminate buildup	64.0 %
8. Laminate	63.4 %
Average	63.6 %
Nominal	59.9 %

The helical rib between the node and the laminate shows a relatively low FVF (although still higher than the advertised FVF). It is already observed that this rib section has a significantly bigger cross-sectional area than the other rib sections. The rib sections close to the nodes are bigger as well so these areas could potentially have a lower FVF as well. If so, the lower FVF is compensated by the bigger cross-section so the net effect on the global elastic behavior will be negligible. The higher density (or FVF) of the samples also explains partially why the samples are heavier than predicted. The density of the samples is 1.1% higher than the advertised and assumed density. This explains about 2 grams of the mass difference. Together with the

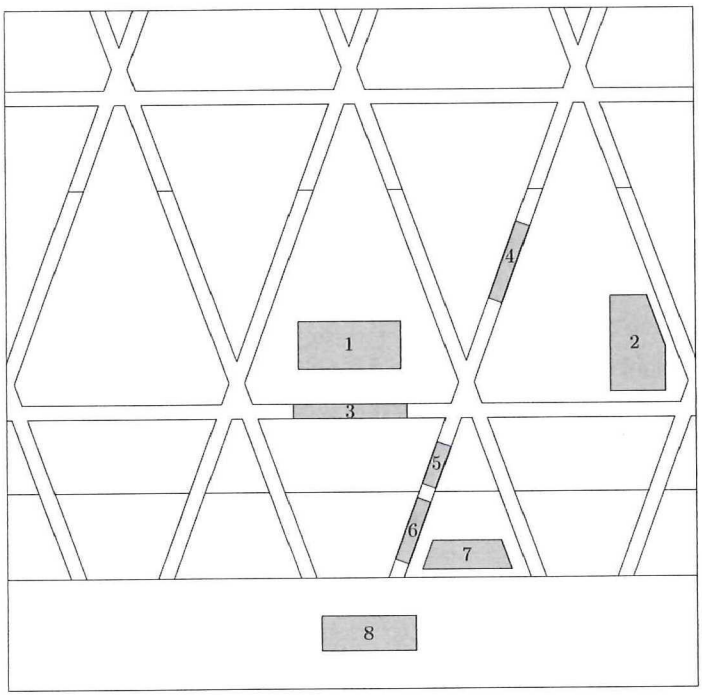

Figure 5.11: Locations of FVF measurements. Grey areas indicative for FVF sample size.

3.5 grams for the excessive fibers in the rib, the 1,5 gram for the rib-laminate interface and 3 grams for the nodal area the total mass difference can be explained.

The high FVF could have a few possible causes. The first one is that more resin is squeezed out than expected. However this would result in much thinner laminates and skins. Based on thickness measurements at the laminate and skins, the average ply thickness in the samples is 0.124mm. For this ply thickness the data sheet indicates a FVF of 61%. So pure resin squeeze out does not explain the high FVF. A second possible cause is that more material has been laid up than intended. This is very unlikely since during layup every ply is documented. Especially at the skin sections, which only consist of ten plies, laying up a ply too much is unlikely. A third possible cause is that the wrong material is supplied by the supplier. This however is unlikely since the batch is well marked with the resin content. A fourth possible cause is a wrong determination of FVF of the test samples of course. This is also unlikely due to proper documentation and careful execution of the tests following the testing standards. The density is measured from which the FVF is calculated. In this calculation it is assumed that the sample only consists of matrix and fibers, so no voids are taken into account. However for a certain density the presence of voids would only increase the FVF.

5.2.4 Curvature

Upon looking more closely at the panels they turned out to be deformed into a slight saddle shape. These curvatures are caused by cure induced thermal stresses in combination with the asymmetry of the panel. With a Digital Image Correlation (DIC) system the initial out-of-plane deformations of the samples can be obtained. This system will be used during testing to obtain both in- and out-of-plane deformations (described in Chapter 6). Figure 5.13 shows the out-of-plane deformation of a sample obtained by making a DIC picture before any load is applied.

The shape of the panel is then compared to the results of the FEM model. By applying a thermal step in the model, the deformations can be calculated. The deformation predicted by the FEM model show good correlation with the measurements obtained with the DIC. The model slightly over-predicts the thermal deformations, as can be seen in Figure 5.14. The deformation along the middle of the panel is then plotted for both the FEM and DIC in Figure 5.12.

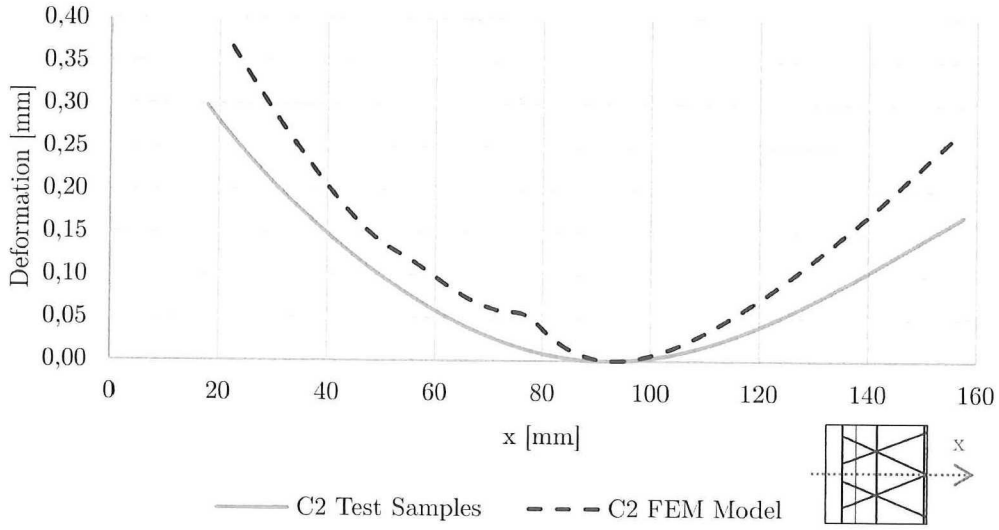

Figure 5.12: Out-of-plane deformation measured along the middle of the test-samples compared with FEM model

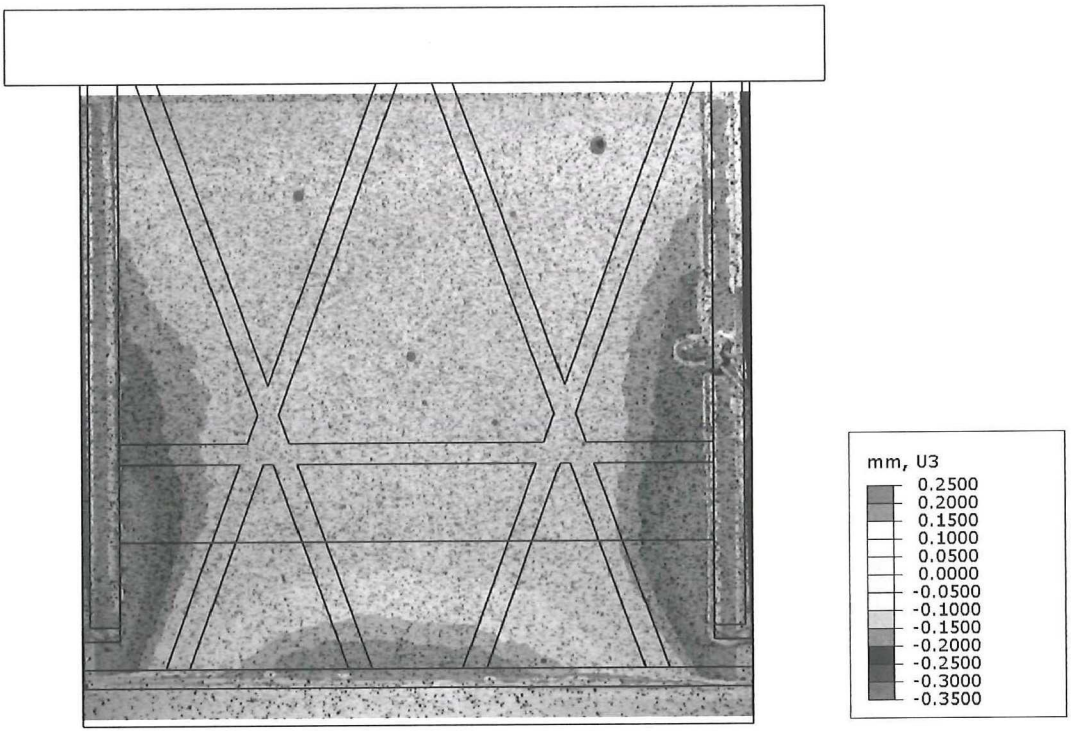

Figure 5.13: Out-of-plane deformation of panel captured with DIC system

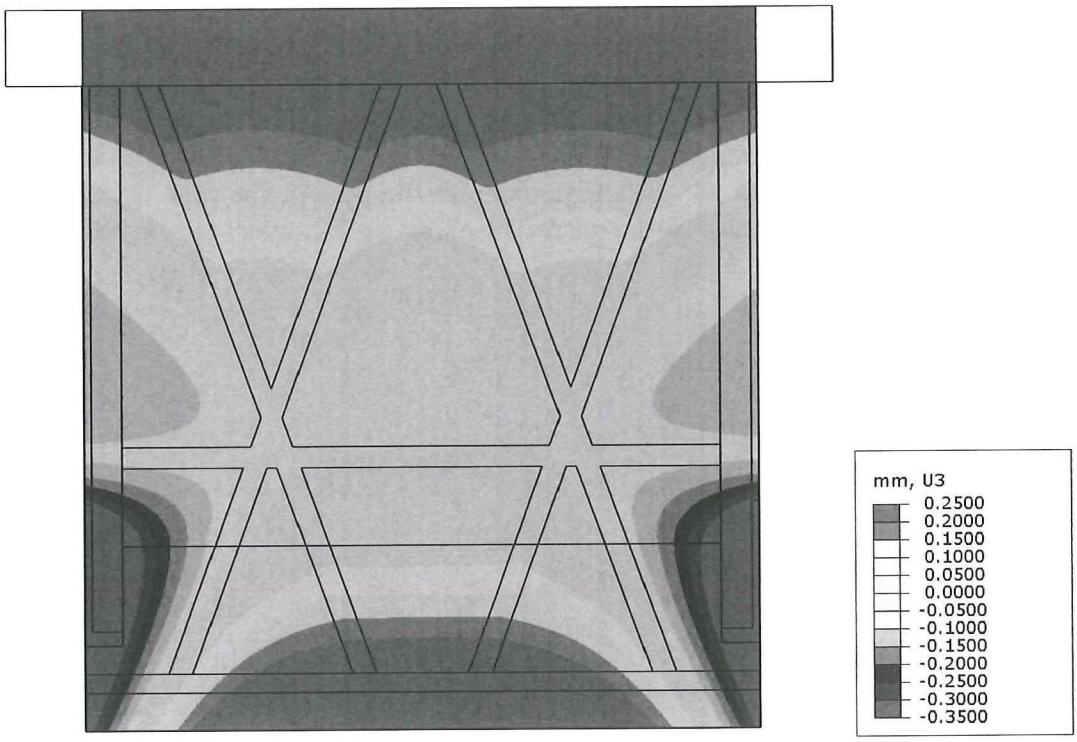

Figure 5.14: Out-of-plane deformation of panel predicted by the FEM model

The laminate section has an interface with the aluminum ring so the exact curvature is important. Obtaining the curvature of the panel with the DIC system requires applying a speckle pattern and this was only done after the aluminum rings were bonded. To measure the curvature along the laminate prior to testing a dial indicator is used. This measurement is then compared to the FEM model as is shown in Figure 5.15. The curvatures for the C1 and C2 configuration are identical, hence only C2 is shown. Curvature data for all samples can be found in Appendix A.2.

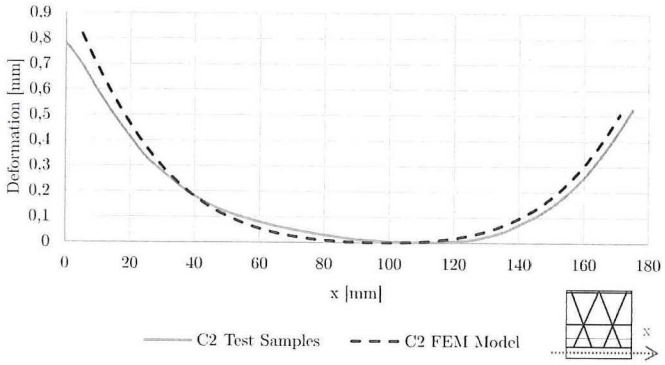

Figure 5.15: Curvature along the width of the test-samples compared with FEM model

The skin makes the panel at both the grid and laminate sections asymmetric. This asymmetry cannot be prevented at the grid section so the curvature along the length of the panel cannot be avoided easily. In the case of the Interstage this curvature is also less relevant, due to its cylindrical shape. But since the model can predict the thermal deformation quite well it is used to investigate the effect of laminate layup on the deformation along the laminate. The skin in the test samples contains two 90° plies while the laminate is build up out of stacks of [0/0/0/0/45/-45] so has no 90° plies to counteract the ones in the skin. By changing the laminate to a quasi isotropic layup the curvature along the laminate can be reduced as can be seen in Figure 5.16.

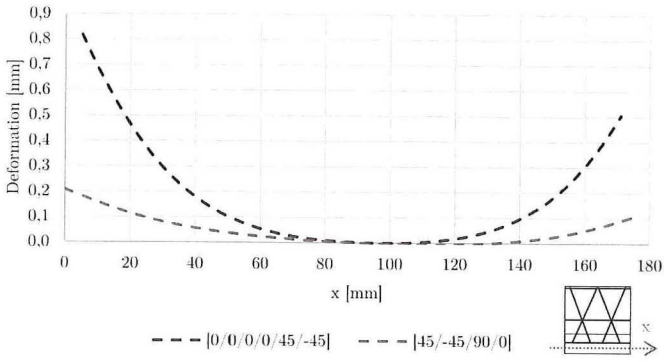

Figure 5.16: Effect of laminate layup on cure induced curvature along laminate predicted by FEM model

5.3 Assembly

The cured composite panels are trimmed to their final dimensions by removing the additional edge cells. An extra piece of rib is removed to remove a potential stress concentration which might lead to early failure. This piece is indicated in Figure 5.1.

The aluminum 'rings' are Computer Numerical Control (CNC) machined to accommodate the curvature described in Section 5.2.4. By matching the curvature of the sample with the ring the correct bond line thickness along the entire laminate can be ensured. The accuracy of the machined pieces has been verified and all dimensions are within ± 0.01mm

The FEM model indicates that during testing the stresses exceed the yield strength of the aluminum usually used for stock L-beams (AL6061), hence the aluminum L-beams have been machined from 7075-T6. Plasticity is not desirable since it makes it harder to predict its behavior.

5.3.1 Adhesive Bonding

The L-beams and the ring have to be bonded to the composite. To ensure a proper bond, all surfaces are cleaned with isopropyl alcohol, sanded and cleaned again. Sanding will roughen the top surface improving the adhesion. A paste adhesive is applied on both surfaces of the joint. Any excess adhesive will be squeezed out. The L-beams are clamped to the specimen with small clips to apply enough pressure for the adhesive to squeeze out and give the bond line the required thickness. To control the bond line thickness glass beads of 0.15mm are added. According to the supplier adding a small percentage of glass beads (1 wt%) should not have any noticeable effect on the material properties. For bonding the rings no clips can be used due to the closed nature of the rings. The bond line thickness will be determined by the accuracy of the rings, which has been shown to be within ± 0.01mm. Adhesive is applied at all surfaces and the composite panel is slid into the ring. The squeezed-out adhesive forms a bead which is left to reduce stress concentrations and is shown in Figure 5.17. This bead also indicates enough adhesive is applied and can be used as a simple means of quality control. Good control of bond line thickness has been confirmed by microscopy as shown in Figure 5.18.

Similar to the prepreg, a cure cycle for the adhesive has been defined by the supplier. The cure temperature does not really influence the material properties but it determines the time required to reach full cure. The test samples cured at room temperature for 24 hours after which they are further cured at elevated temperature (65°C) to ensure the adhesive is fully cured in a reasonable time frame. It is cured at room temperature first to reduce the thermal stresses introduced by to the difference in coefficient of thermal expansion.

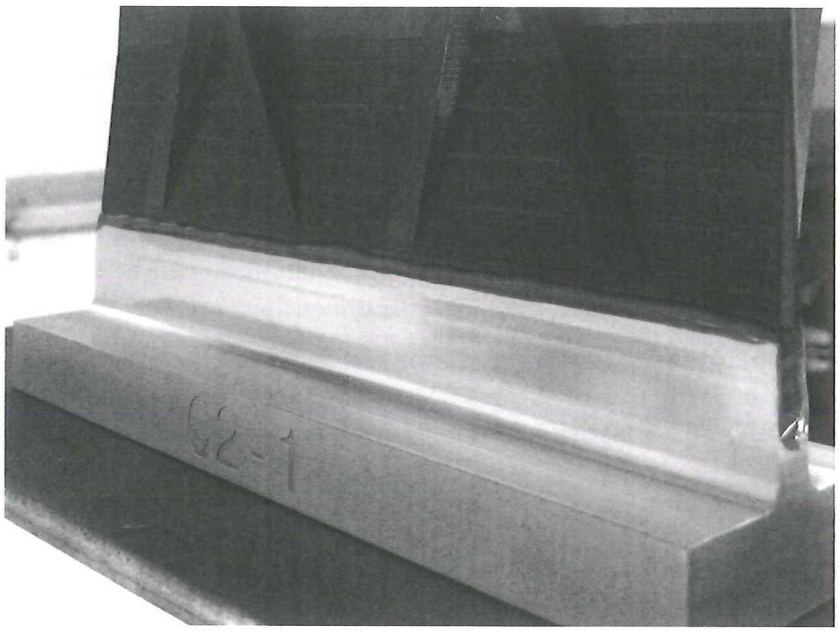

Figure 5.17: Bead formed by squeezed-out adhesive

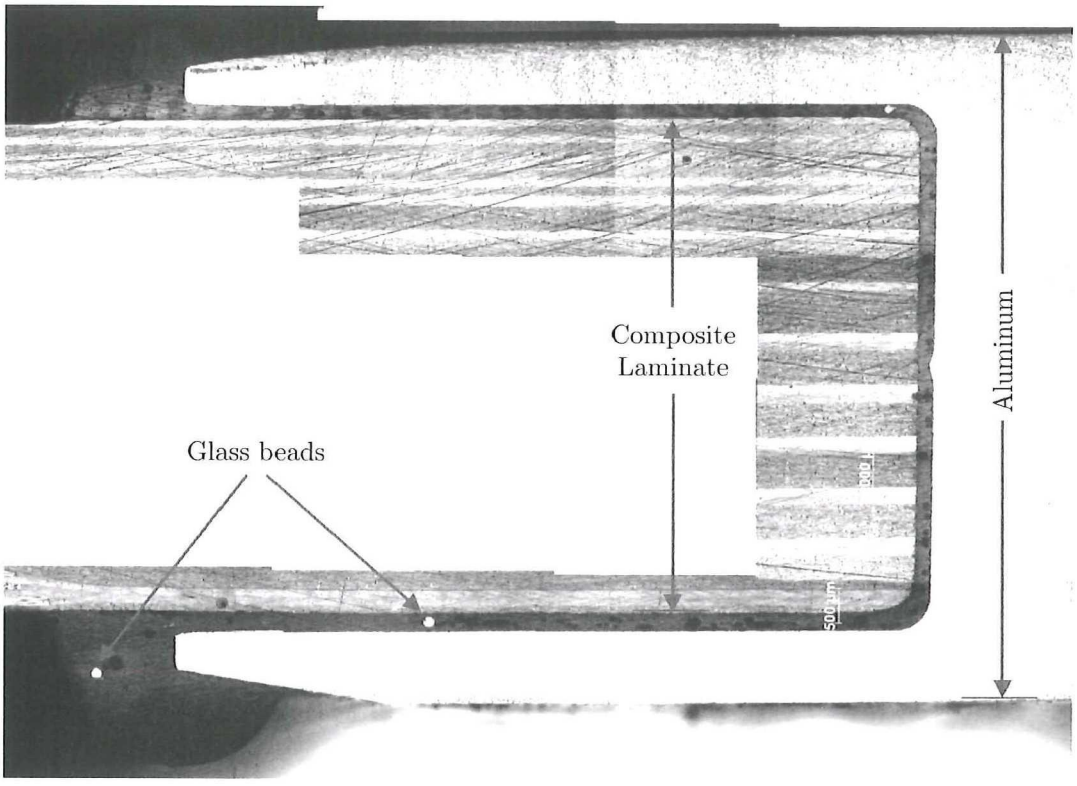

Figure 5.18: Microscopy picture of bond-line showing good bond thickness control and overall quality.

5.3.2 Potting

The final step is potting of the far-field grid-side of the panel. The embedded surface is cleaned and sanded for proper adhesion of the potting material. The test sample is placed in a mold and resin is poured till the potting has reached the required height after which is cured at 40°C for 14 hours. In the final step the top surface of the potting is machined to create a flat surface parallel to the bottom of the aluminum ring. This ensures the load will be evenly distributed.

Chapter 6

Testing and Correlation

Testing of the samples described in Chapter 5 is carried out to obtain the strain/stress fields in the sample which can be used to correlate and verify the FE models described in Chapter 4.2. Also the global performance of the panel can be verified, both in terms of stiffness and strength. This test campaign is focused on the elastic correlation but does allow for strength correlation.

In the first section of this chapter the test set-up is described after which the test results are presented. These results are then compared with the predictions made by the test sample models in Section 6.3. Finally in Section 6.3.4 the possible causes for differences between the models and tests are presented.

The testing of samples has been carried out at the DASML facilities.

6.1 Test Set-Up

The test samples have been designed for a compressive loading. The compressive test bench has a leveling top plate to make sure no additional bending is applied at the sample. Before every test the top plate is checked and adjusted if necessary. The test bench is operated manually. Also all data acquisition (DAQ) and DIC measurements were done manually. A reference measurement was taken at 0kN to calibrate the instrumentation. Since the DAQ was controlled manually load was applied in steps of 1kN. At 60kN, 100kN and 120kN a load excursion to zero was included to check for any hysteresis in the system.

6.1.1 Instrumentation

The data obtained for the correlation of the model is:

- **Applied load** - The applied load is required to obtain the stiffness and strength of the panel. Also the correlation of strain fields and out-of-plane displacement is based on applied load. The load is measured by a load cell in the bottom plate of the test bench which has been calibrated to assure correct readings.
- **In-plane displacement** - From the total in-plane displacement in combination with the applied load the membrane stiffness of the panel can be obtained which is used to verify the global elastic in-plane behavior. The displacement is measured by two Linear Variable Differential Transformers (LVDT) which are placed on both sides of the sample as shown in Figure 6.2. The displacement is measured between the two plates of the test bench and are placed as close to the sample as possible. The LVDTs are placed on both sides of the sample for redundancy and checking if the displacement is uniform along the sample.
- **Out-of-plane displacement** - The out-of-plane displacement is used to verify the bending and/or buckling behavior. It is also used to obtain the curvatures of the samples as discussed in Section 5.2.4. A DIC system is used to capture the out-of-plane displacements. A black and white speckle pattern is applied on the samples which is then captured by two cameras. A stereo system is used as it gives the out-of-plane displacement for the entire panel whereas a mono system would only give the in-plane displacements.
- **Strain fields** - The strain fields in the panel can be used to verify local behavior such as load paths and distribution. Strain fields can also be obtained from the DIC data, however a DIC system can only capture the strain at faces that are in the field of view of both cameras. Due to the complex geometry of the test samples the DIC system was used on the skin side. Strain Gages (SG) were used instead to measure the strains at the ribs and the aluminum ring. Strain gages were placed on all helical ribs to measure load distribution between the ribs which might indicate non-uniform loading. To measure the redistribution of load by the nodes strain gages were placed on both sides of the node. Since the models indicate that the adhesive is critical, strain gages are placed on the aluminum ring to measure the load transfer through the adhesive. These strain gages are placed on both sides of the aluminum ring to verify the load distribution between the skin- and grid-side adhesive. The placement of strain gages can be seen in Figure 6.1. An additional strain gage is placed on the DIC speckled side to correlate the DIC system as will be discussed in Appendix A. The noise of the DIC system is indicated in Table 6.1 for strain and displacement values.

  The final instrumented test-samples can be seen in Figure 6.3.

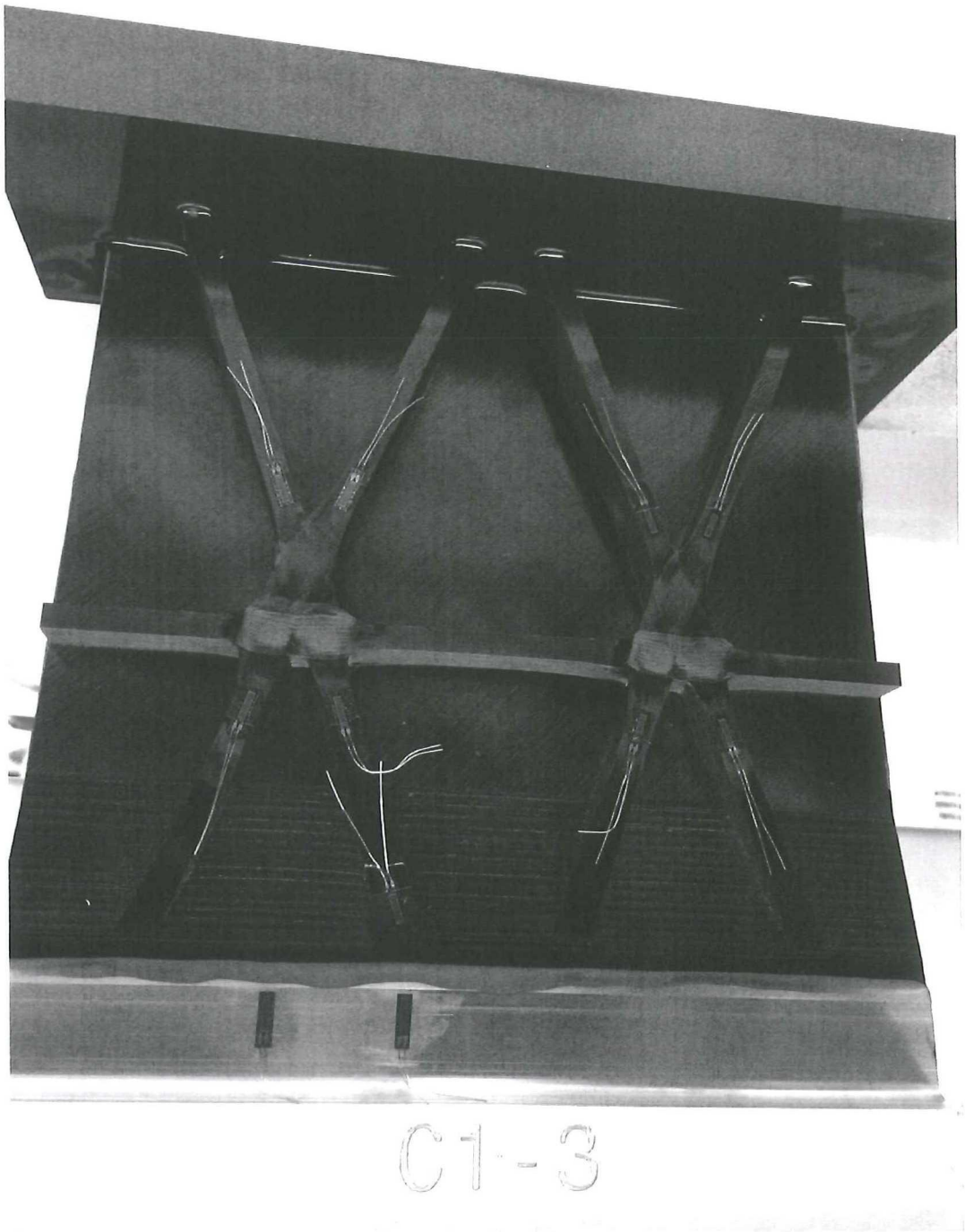

Figure 6.1: Strain Gages applied on test-sample

Table 6.1: Typical noise levels DIC system

Variable	Noise	Unit
Strain in-plane	0.00015	[-]
Displacement in-plane	0.003	[mm]
Displacement out-of-plane	0.020	[mm]

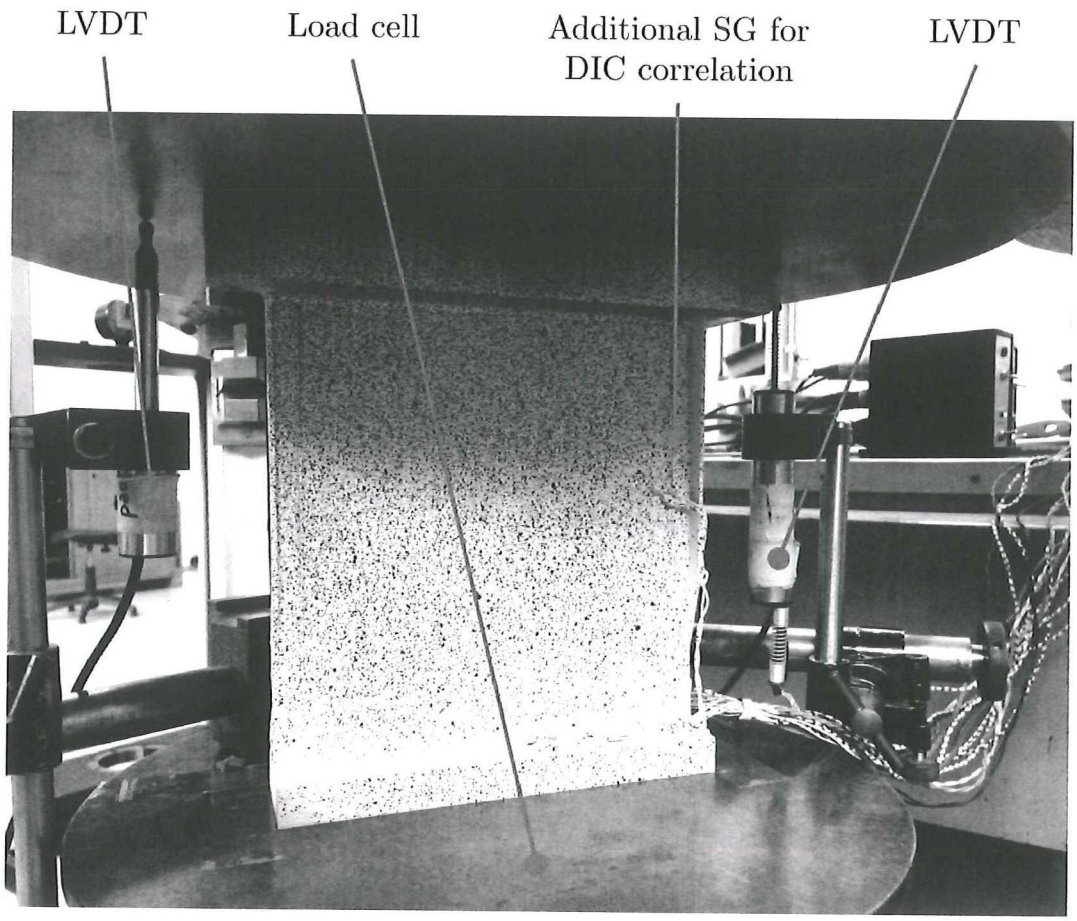

Figure 6.2: Test set-up showing DIC pattern and LVDTs

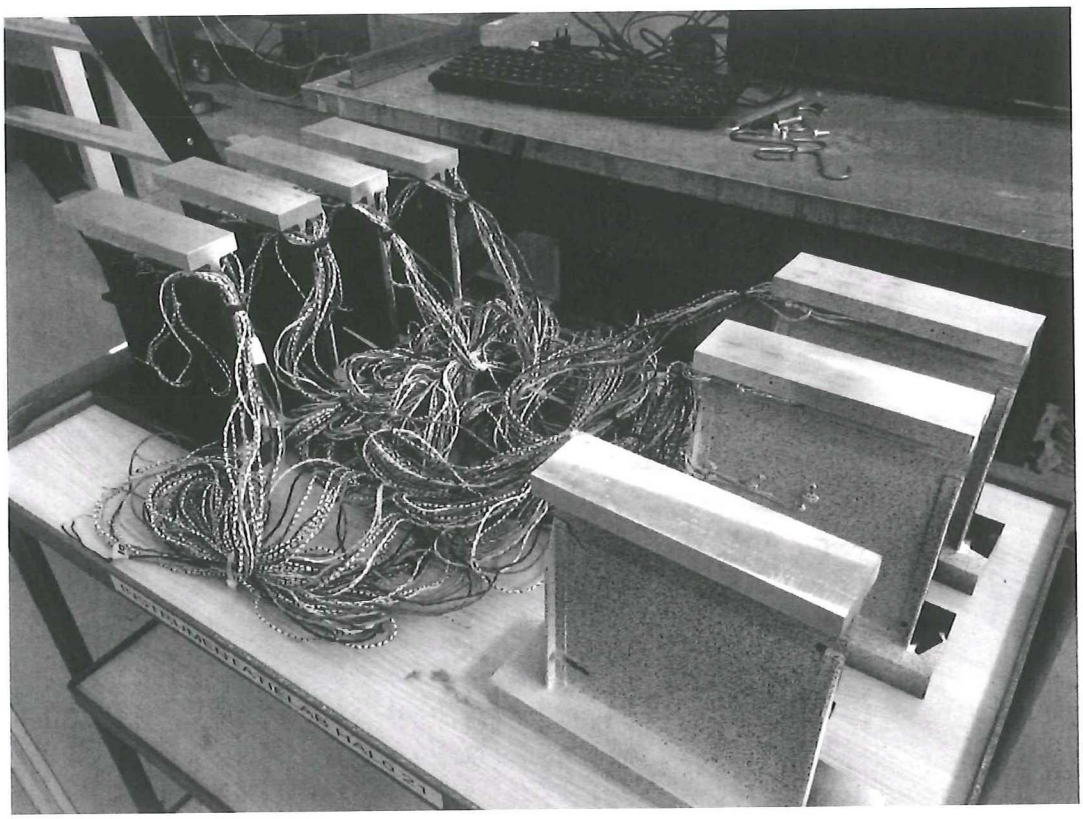

Figure 6.3: Test samples ready for testing.

6.2 Test Results

The test results are summarized in Table 6.2 and Figure 6.4. The initial failure loads are based on the first audible sign of failure. The C2 samples failed completely seconds after the first cracking sounds were heard. Hence for the C2 samples the initial failure is also the final failure whereas the C1 samples were loaded for another 3 to 8 kN after initial failure was observed. The samples within one configuration show great agreement in displacement and differ only ±1% to each other.

It should be noted that the testing of sample C1-3 is stopped after initial failure was observed. It is hard to deduce the initial failure location when the complete panel has failed as can be seen in Figure 6.5. Multiple different failure modes can be observed at different locations so it impossible to tell where it started purely based on the failed samples. However regions that did not fail can be identified. For example no failure is observed in the adhesive. Failure would most likely start at the edge of the aluminum ring on the skin-side where stresses are highest. Failure would show as a crack in the white paint applied for the DIC. Since sample C1-3 was only loaded to initial failure it was inspected with a microscope to look for its initial failure location. This will be described in Section 6.3.2. Also not all data is obtained for sample C2-1. The load cell of the test bench broke and no load data was obtained.

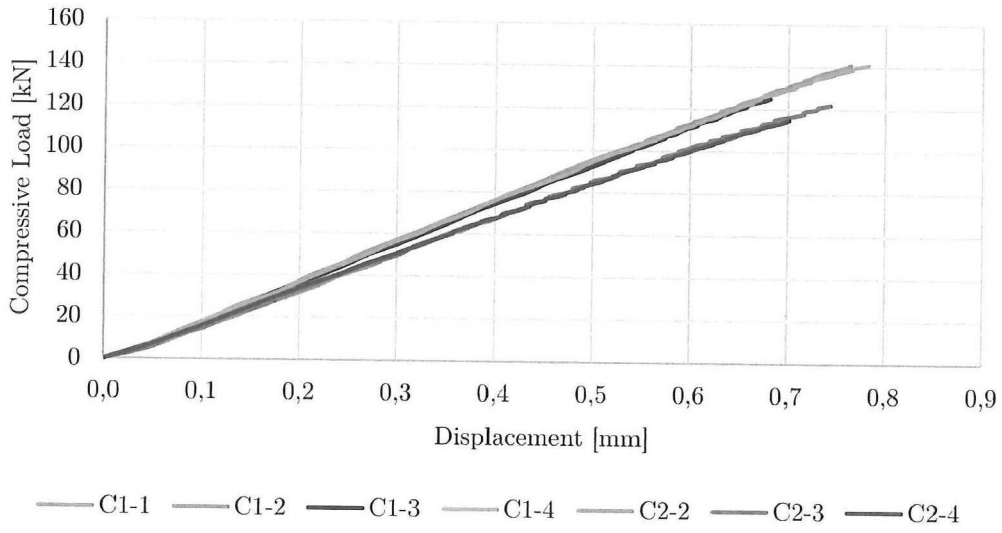

Figure 6.4: Displacement versus applied load for test samples

Table 6.2: Test results

Test sample	Load Initial Failure	Load Final Failure	Displacement Initial Failure	Displacement 93kN
C1-1	138 kN	141 kN	0.75 mm	0.49 mm
C1-2	134 kN	139 kN	0.72 mm	0.49 mm
C1-3	125 kN	-	0.67 mm	0.50 mm
C1-4	133 kN	141 kN	0.72 mm	0.49 mm
C2-1	-	-	0.782 mm	-
C2-2	110 kN	110 kN	0.66 mm	0.55 mm
C2-3	122 kN	122 kN	0.74 mm	0.55 mm
C2-4	115 kN	116 kN	0.70 mm	0.55 mm

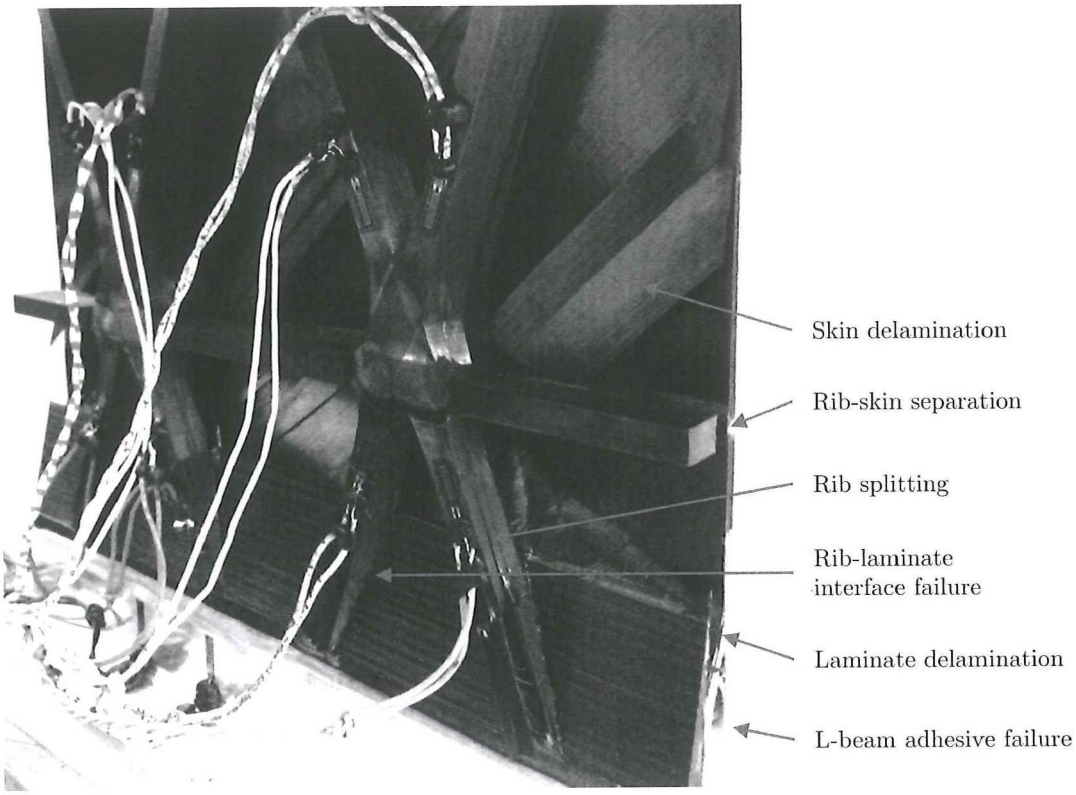

Figure 6.5: Complete failure of sample C1-1 showing multiple failed regions

6.3 Test Sample Model Correlation

The obtained test results are correlated with the models first by correlating the global performance. Bot in terms of stiffness (elastic behavior) and strength. The global elastic behavior correlation is done for both in-plane and out-of-plane. For strength the failure locations and failure loads are correlated with the model. Next the local performance is assessed by correlating at a more detailed level.

Results shown in this chapter are typical and/or averaged results. Full data can be found in Appendix A.

6.3.1 Stiffness

The global in-plane stiffness is correlated by plotting the total displacement, measured by the LVDTs, versus the applied load. Since the displacements of the samples of each configuration are within 2%, the data is averaged to a single test data curve. These displacement curves are shown in Figure 6.6. From these plots can be concluded that the test data matches the model already quite well in terms of global in-plane stiffness, although a slight under prediction of the stiffness can be observed for both configurations. The stiffness of the C1 test panels is 5.4% higher than de model predicted whereas the stiffness of the C2 test panels is only 4.1% higher than the model predicted. The stiffness values are based on the total displacement at 93kN as the behavior of the test samples is slightly non-linear. The models also show a slight non-linear behavior but not as strong as the test samples.

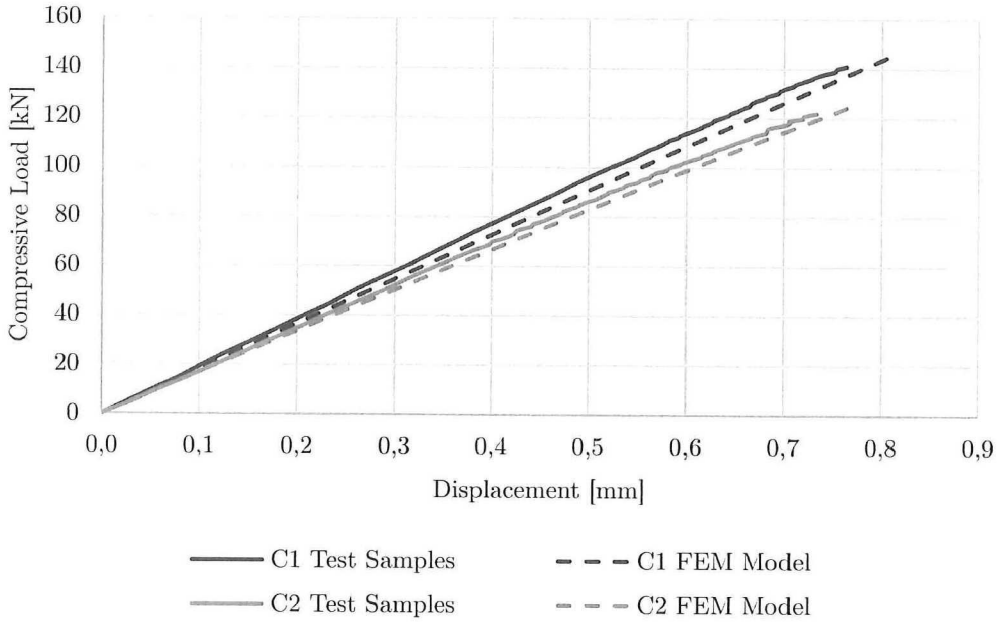

Figure 6.6: Averaged test results compared with FEM model prediction

The global out-of-plane stiffness is correlated by plotting the out-of-plane displacement field, measured by the DIC system, and comparing this to the displacements obtained from the FEM

model. The FEM model shows in general more out-of-plane displacement, which indicates a lower bending stiffness. This is in line with the lower in-plane stiffness. At the two nodes in the middle of the panel, which will be used as a reference for the grid, we see that the model predicts 26% higher out-of-plane displacements than the C1 test samples. For the C2 test samples the opposite can be seen where the model actually predicts 2% lower displacements. The maximum out-of-plane displacements can be found at the skin in the middle cell closest to the laminate. The displacement at this point is over-predicted by the model by roughly 13% for both configurations. The models predicted a relative displacement of the skin to the nodes of 0.31mm for C1 and 0.57mm for C2. The actual measured displacements were 0.30mm for C1 and 0.43mm for C2. So the C1 FEM model over-predicts the overall out-of-plane displacement where the C2 model only over-predicts the out-of-plane skin displacement. As shown in Section 5.2.4 the samples are slightly curved. This curvature will have an effect on the global elastic behavior of the panel. Even though the curvatures of both configurations are similar, it will have stronger effect on the thinner and softer C2 samples. The out-of-plane displacement measured along the middle line of the panel is shown in Figure 6.9 for C1 and in Figure 6.10 for C2. In these graphs it can also be observed that the out-of-plane displacement between the hoop rib (at 75mm) and the potting (at 170mm) varies quite a bit. Not only does the amount of displacement differs also the direction of displacement is different between samples. These differences are most likely caused by imperfections in the skin, which could be for example thickness variations, ply angle variations or variations in thermal stresses.

The results for the stiffness correlation between the model and the test samples are summarized in Table 6.3.

Table 6.3: Comparison of global stiffness predicted by FEM model and measurements

Displacement at 93 kN	Predicted	Measured	Difference
C1			
Total in-plane	0.51 mm	0.48 mm	-5.4%
Node out-of-plane	0.27 mm	0.20mm	-26%
Maximum out-of-plane	0.58 mm	0.50mm	-14%
C2			
Total in-plane	0.57 mm	0.55 mm	-4.1%
Node out-of-plane	0.47 mm	0.48mm	+2%
Maximum out-of-plane	1.04 mm	0.91mm	-12%

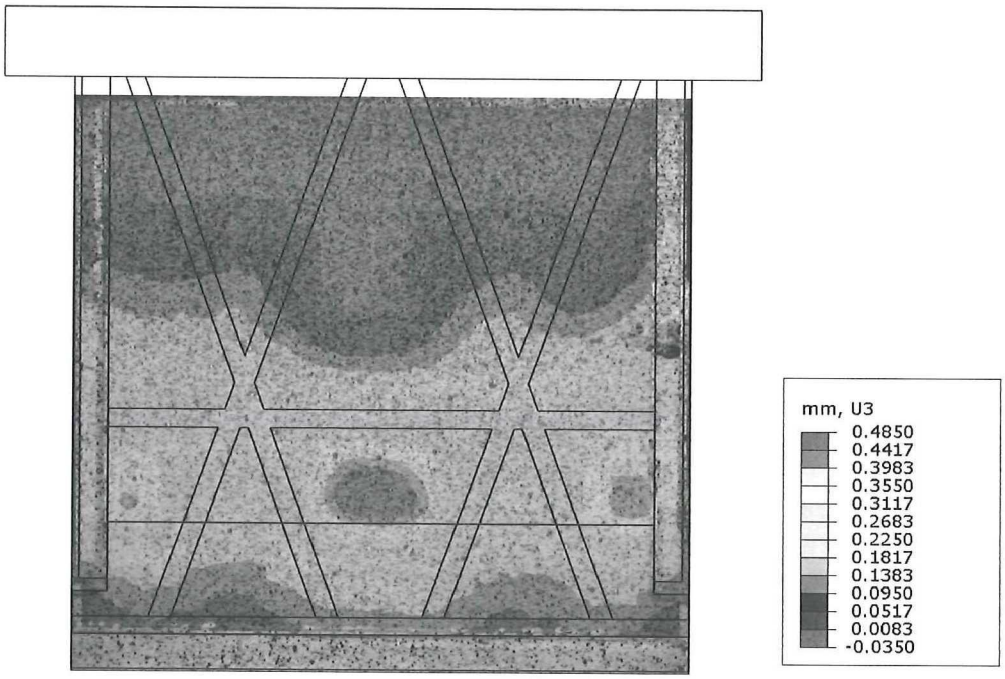

Figure 6.7: Out-of-plane displacement at 93kN captured with DIC system (sample C1-1)

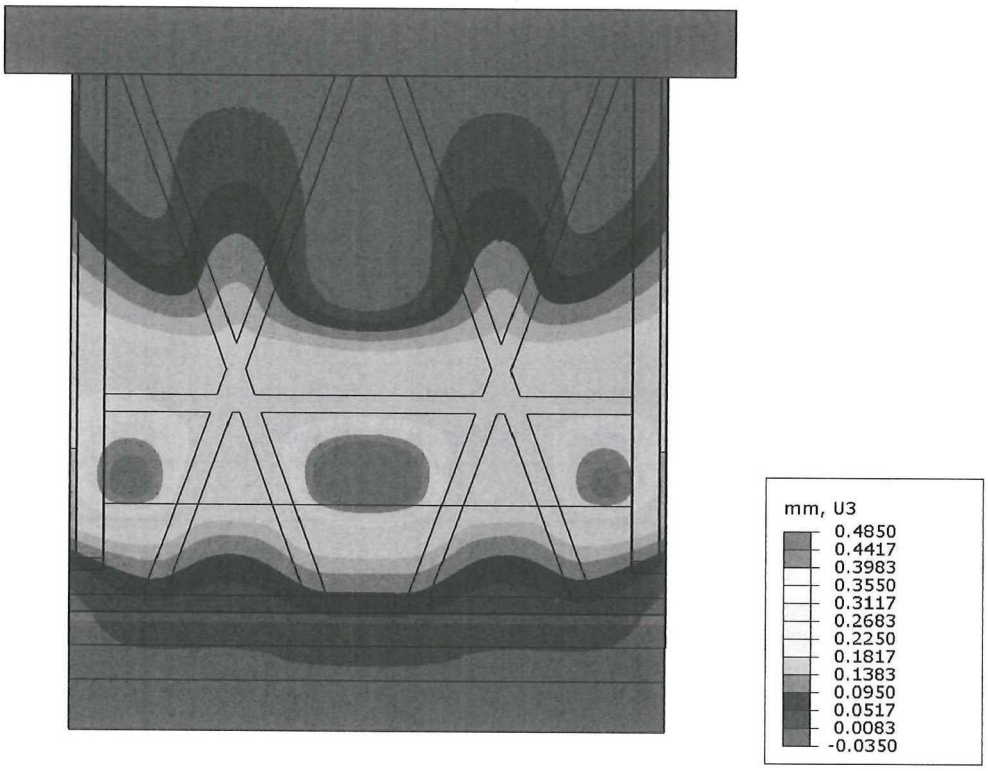

Figure 6.8: Out-of-plane displacement at 93kN indicated by C1 FEM model

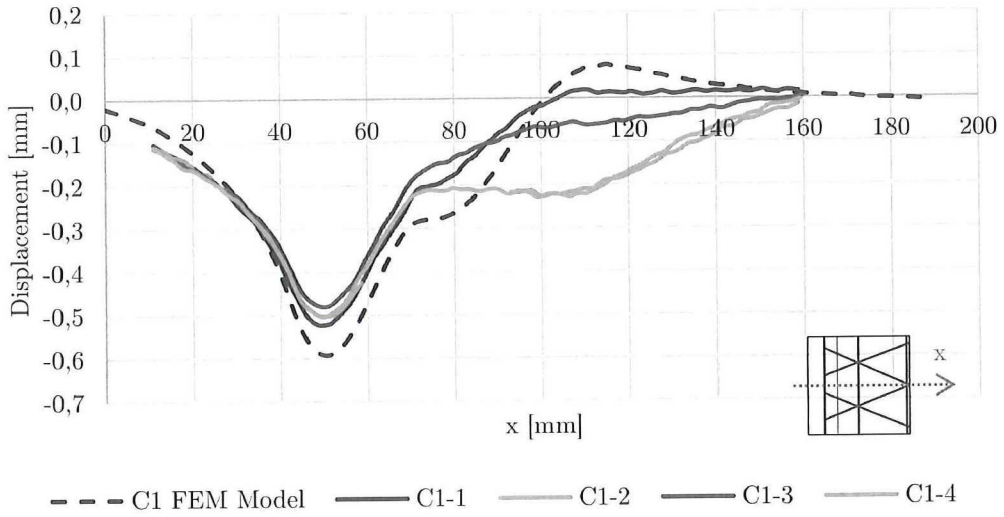

Figure 6.9: Comparison of out-of-plane displacement at 93kN measured along the middle line of C1 test samples at 93kN and FEM model

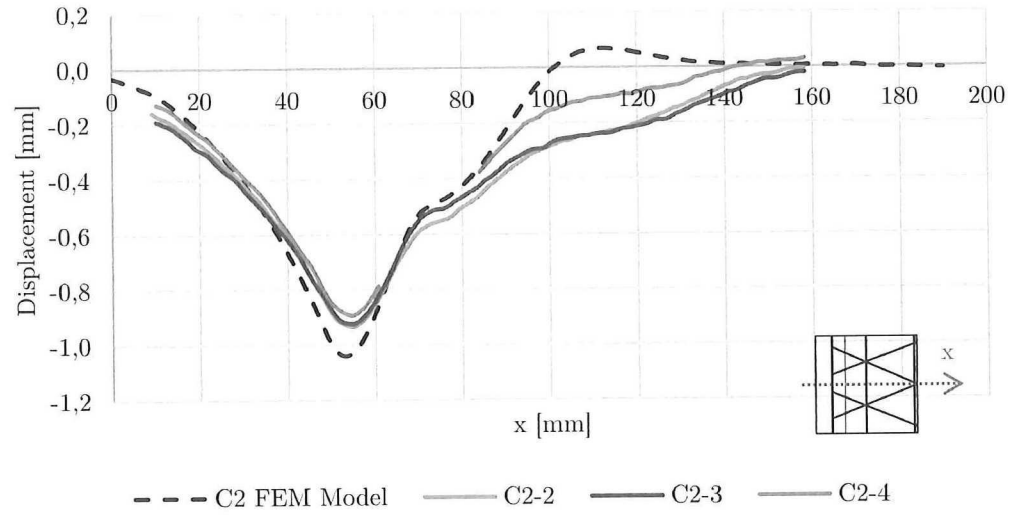

Figure 6.10: Comparison of out-of-plane displacement at 93kN measured along the middle line of C2 test samples at 93kN and FEM model

6.3.2 Strength

The models predicted the C1 samples to fail in the skin close to the rib-laminate interface. However failure of the skin does not automatically lead to complete failure of the sample. The ribs are the main load carrying elements, so failure of the skin will most likely result in redistribution of loads into the ribs. As was already observed in Chapter 4 the model indicated that the failure of the skin was closely followed by failure of the laminate at the rib-laminate interface. Failure of this interface and hence failure of the critical load path will lead to complete failure of the sample. This explains the load carrying capability of the C1 samples after initial failure. Microscopy of sample C1-3, which was only loaded up to initial failure, confirmed the existence of failure in the skin and also some failure of the rib-laminate interface as can be seen in Figure 6.11. On the other hand, the models of the C2 samples predicted failure to start at the rib-laminate interface. In this case the initial failure will directly lead to complete failure of the sample. The test samples therefore show no load carrying capabilities after initial failure.

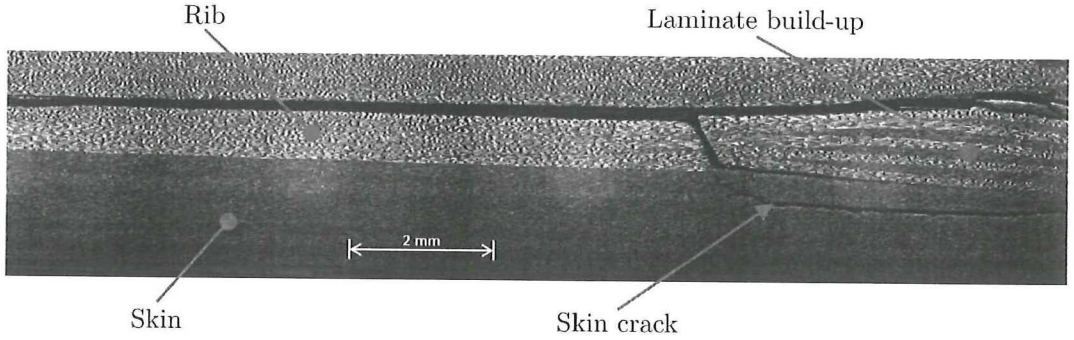

Figure 6.11: Failure at the rib-laminate interface and crack in the skin

The initial failure loads of the C1 samples are within 10% of each other. Compared to the FEM model the failure loads are only 20% lower than predicted. The same can be said about the failure loads of the C2 samples which are also within 10% of each other and roughly 20% lower than predicted. The results can be found in Table 6.4.

Table 6.4: Comparison of initial failure loads predicted with FE model and measurements

Test sample	Predicted	Measured	Difference
C1-1	163 kN	138 kN	-15 %
C1-2	163 kN	134 kN	-18 %
C1-3	163 kN	125 kN	-23 %
C1-4	163 kN	133 kN	-18 %
C2-1	147 kN	-	-
C2-2	147 kN	110 kN	-25 %
C2-3	147 kN	122 kN	-17 %
C2-4	147 kN	115 kN	-22 %

6.3.3 Local Performance

From the DIC data also the in-plane strain values in the skin can be obtained. The FEM models show slightly higher strain values compared to the test results, indicating the test samples are stiffer than the FEM model. This is in line with the other results.

The DIC only shows the strain in the skin, so for the actual strain values in the ribs the strain gage data is used for correlation. While the strain gages resulted in good quality data, the actual strain values between samples within a configuration varied a bit as can be seen in Figure 6.12. The samples are symmetric around the middle line, so the strains in the outer ribs should be the same as well as the two inner ribs. In total 106 strain gages are placed on 18 different locations, so to make results interpretable the strain gages on the outer ribs are averaged as well as the strain gages on the inner ribs. Also the strain gage data of the different samples within a configuration are averaged. After initial failure the local strain will start to vary, so the averaged strain values are only representative till the first sample starts to fail. The average of the strain gages on the outer ribs for the C1 samples is shown in Figure 6.13. From the strain gage data it can be observed that in general the test samples show less strain than the FEM model. Again the FEM model is under-predicting the stiffness.

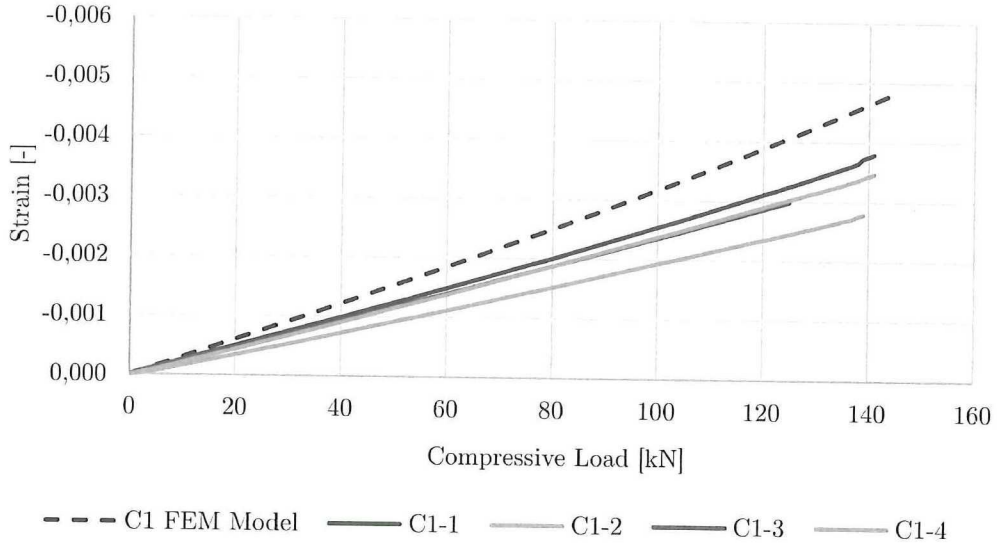

Figure 6.12: Typical strain gage data compared with FEM model

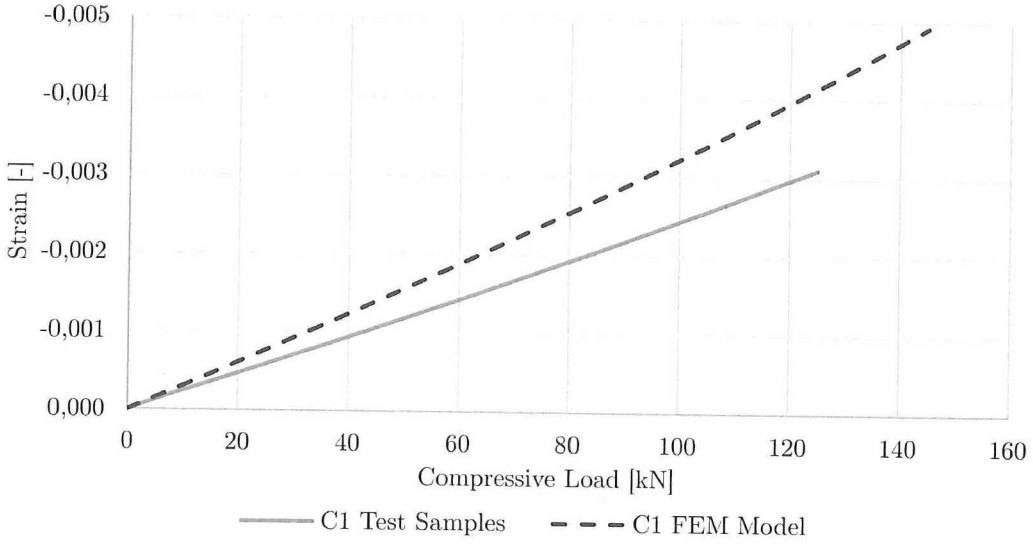

Figure 6.13: Averaged strain gage data of C1 samples compared with FEM model

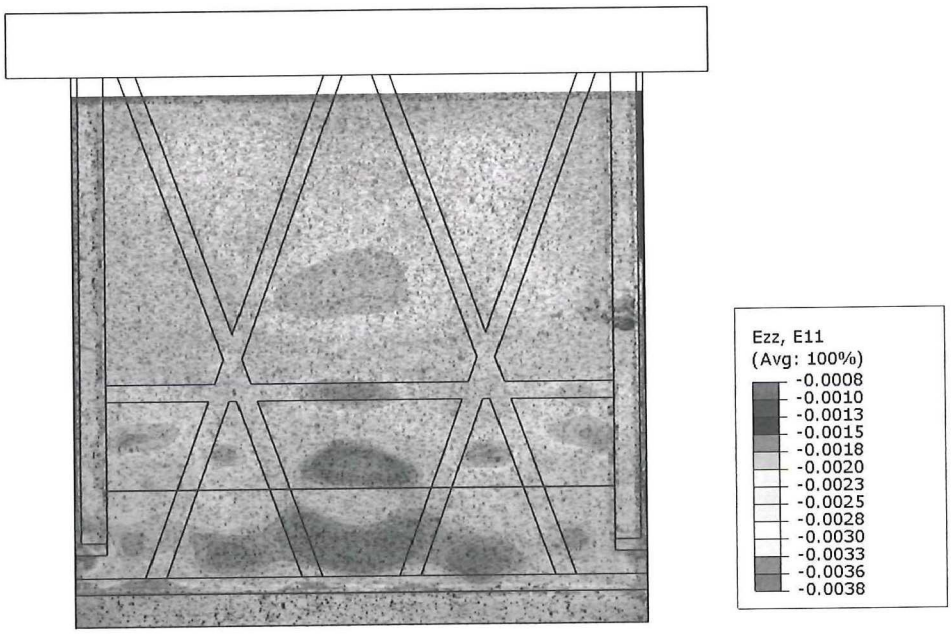

Figure 6.14: Strain in loading direction captured with DIC system (sample C1-1)

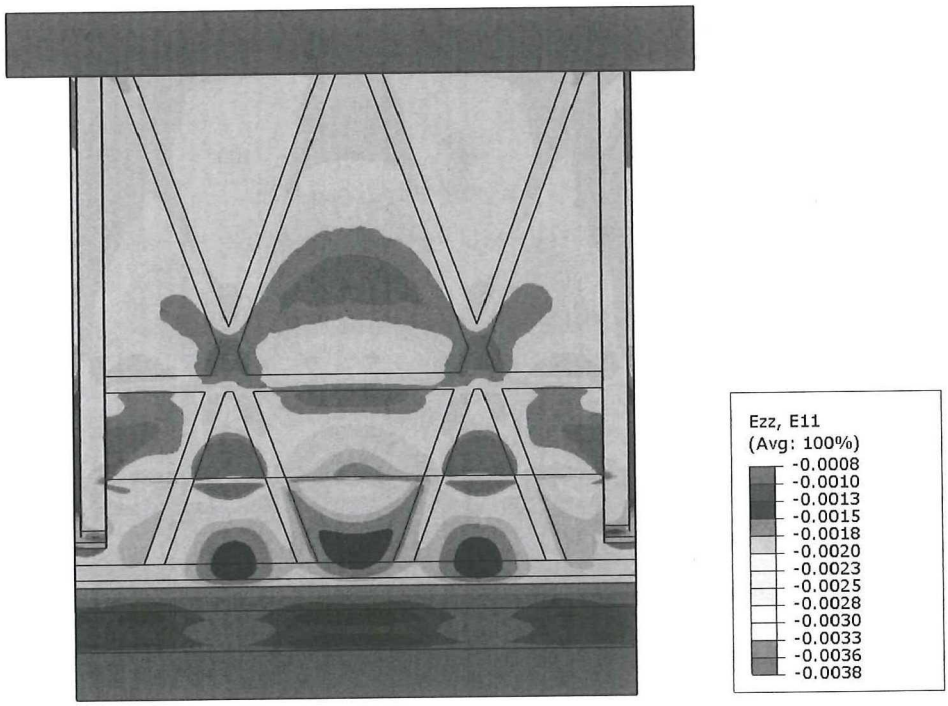

Figure 6.15: Strain in loading direction predicted by FEM model

The strain gage data also clearly shows a sudden increase in strain in the ribs for sample C1-2 and C1-4. For C1-2 this happens at 134kN what corresponds with the initial failure load which was based on the first audible sounds. For C1-4 the sudden increase in strain happened at 136kN while the first cracking sounds were heard at 133kN. Also for C1-1 cracking sounds were heard at 138kN but no significant change in strain can be found in the strain gage data. While sample C1-2 and C1-4 showed a significant increase in strain in the helical ribs it does not show a clear load distribution. In Figure 6.16 the strain values for strain gages 1 to 8 can be found. Strain gages 1 to 4 are located on the ribs between the node and potting (top four strain gages in Figure 6.1) and 5 to 8 are located on the ribs between the node and the laminate. It can be seen that SG 1 and 2 show a sudden increase in strain first. These stain gages are located on adjacent ribs. A little later the same sudden change in adjacent strain gages 3 and 4 can be observed. Based on the strain gage data the initial failure location can not be identified.

In the strain gage data obtained from the C2 samples no significant changes in strain can be found. Also no audible sounds were heard during testing.

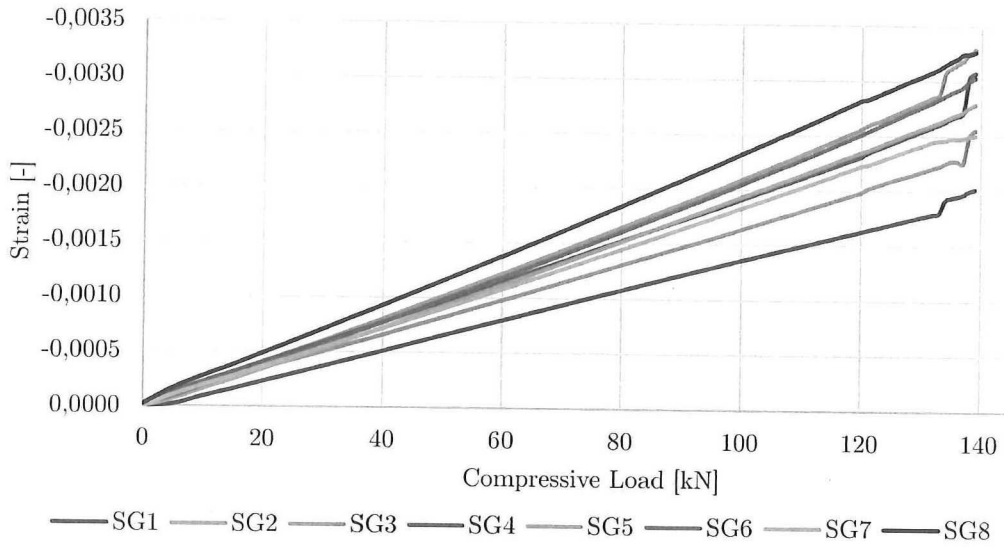

Figure 6.16: Strain gage data of sample C1-2

6.3.4 Conclusions

Although showing good correlation in general, the model seems to be slightly over-predicting the strains and thus under-predicting the global stiffness. The model over-predicts the out-of-plane displacement, which could point to a too low bending stiffness. This lack of global stiffness in the model might have the following causes:

- **Material assignment** - All CFRP parts in the model are assigned the same material properties. Abaqus does not make a distinction in compressive and tensile properties, therefore the CFRP stiffness properties are selected based on the lowest values. Which in the case of the modulus in the fiber direction is the compressive, while some parts in the panel might be in tension. The difference in modulus in fiber direction between tensile and compressive is roughly 12%. Proper assigning material properties according to whether they are under tension or compression can improve the model performance.
- **Dimensions** - It has already be shown in Chapter 5 that the dimensions of the test samples are between 2,5 and 5% different than the design values. Since the FEM model is based on the design values any difference in the global stiffness can be attributed to not having the correct geometry.
- **Material properties** - Material properties have a direct influence on the global stiffness of the panel. The material properties of the aluminum parts will not differ significantly from the design values. The material properties which are most likely to be different than assumed are the adhesive and CFRP properties. The effect of the adhesive properties on the global behavior is expected to be small. It has been shown in Section 5.2.3 that the FVFs are higher than assumed in the model. The increased E-modulus of the material will have an effect on the global behavior.
- **Panel curvature** - As shown in Chapter 5 the panel is deformed to a saddle shape due to thermal stresses after cure. These deformations can influence the global performance of the panel either by decreasing or increasing its global stiffness. The curvature in the laminate section of the panel might give it geometrical stiffness whereas the curvature in the grid section decreases the global stiffness.

The model also showed a decent correlation in terms of strength. Although over-predicting the strength by roughly 20%, the model seems to be predicting the failure location and sequence quite well. Some aspects that might improve the strength prediction apart from the ones mentioned above are:

- **Defects** - Local defects such as the ones in the nodal region discussed in Section 5.2. The defects will create stress-concentrations leading to early failure. For example stress concentrations at the rib-laminate interface, caused by the interwoven rib plies, might have led to early failure.
- **Thermal stress** - The thermal stresses that partly resulted in curvatures of the test samples are not accounted for in the models. Even though stresses in the samples are relieved by the curving of the panel, some internal pre-stresses might sill be present.

- **Material properties** - The increased FVF will not only affect the stiffness properties of the material, also strength values will be affected. Other factors that increase material scatter such as environmental influences might also result in inaccurate material failure properties.

- **Model related** - Several inaccuracies can be found in the model apart from the dimensional and material assignment. Simplifications described in Chapter 3.3.2 might not have affected the global elastic behavior but they can have a large effect on strength predictions. Simplifications that might have affected the strength prediction are among others the discretization of the laminate build-up, not modeling the interweaving of rib and laminate plies and neglecting the angling down of rib plies. On top of that the failure criterion might be inaccurate.

Chapter 7

Model Improvement

In the previous section multiple potential causes of the mismatch in global stiffness are discussed. The causes can be translated into possible improvements of the models. As outlined in Chapter 1 the main focus of this research is on the global elastic behavior. This means that the models are improved only on the items that will lead to a better stiffness correlation. The strength will be correlated with these improved models but is not a direct input for the model improvements.

7.1 Test Sample Model Modifications

Four main causes for the under-prediction of global stiffness were discussed; the material assignment, sample dimensions, material properties and the panel curvatures. Each of these causes and the corresponding improvements are assessed and evaluated separately. By doing this the impact of the different causes can be identified. In the end the applicable improvements are combined into a final improved model.

To keep things clear all graphs in this section show results for the C1 configuration only. All relevant graphs for the C2 configuration can be found in Appendix B. Also typical strain gage values are used. A detailed overview of strain gage correlation with the improved models can also be found in Appendix B.

In order to study the impacts of the different improvements the values for the base model are summarized in Table 7.1.

Table 7.1: Comparison base model with test samples

	Base Model	
C1		
Global in-plane stiffness	-5%	Under-prediction
Out-of-plane displacement at node	+26%	Over-prediction
Strain SG5/8	+32%	Over-prediction
C2		
Global in-plane stiffness	-4%	Under-prediction
Out-of-plane displacement at node	-2%	Under-prediction
Strain SG5/8	+12%	Over-prediction

7.1.1 Material Assignment

For the CFRP sections in the model an anisotropic material has been defined. That means different material properties are assigned to different directions. This however does not allow for assigning both tensile and compressive material properties to a single direction. For the base model the lowest value for each property is used, which means the compressive modulus in the fiber direction and the tension modulus in the transverse direction. While most of the material is in compression some parts or plies might be in tension. Each ply in each section is assessed whether it is in compression or tension and assigned the correct material property. Since most of the material is in compression and the compressive modulus was already assigned to the fiber direction the implementation of the Material Assignment (MAT) improvement had little to no effect as can be seen in Table 7.2.

Table 7.2: Comparison improved material assignment (MAT) model with test samples and base model

	MAT model	Improvement
C1		
Global in-plane stiffness	-5%	0%
Out-of-plane displacement at node	+26%	0%
Strain SG5/8	+32%	0%
C2		
Global in-plane stiffness	-4%	0%
Out-of-plane displacement at node	-3%	-1%
Strain SG5/8	+11%	1%

7.1.2 Dimensions

It was shown in Section 5.2.2 that the ribs were about 5% bigger than designed. Modeling the real geometry will obviously improve the model. The 5% was an averaged number so different sections of the model are modeled to match the actual measured dimensions. This Improved Dimensional (DIM) model shows quite some improvement in terms of global in-plane stiffness and under-predicts the stiffness of the C1 samples by only 1.5% and 'over-predicts' the stiffness of the C2 samples by a mere 0.3% as can be seen in Figure 7.1.

Also the out-of-plane displacement of the C1 configuration matches the test samples quite well and is only off by 9% at the nodes. The skin in the cell bay between the nodes and the laminate almost shows a perfect match, as can be seen in Figure 7.2. This shows that the bending stiffness of the model has increased which improved the C1 configuration but for the C2 configuration, which was already too stiff, resulted in a larger over-prediction of bending stiffness.

The realistic rib dimensions also improved the local strain fields measured by the strain gages. Where the strain gages on the C1 test samples still show that the model over-predicts the strain and therefore under-predicts the stiffness (see Figure 7.3), the strain gages on the C2 test sample indicate an over-prediction of stiffness. This matches with the observations made earlier.

Table 7.3: Comparison improved dimension (DIM) model with test samples and base model

	DIM model	Improvement
C1		
Global in-plane stiffness	-1%	4%
Out-of-plane displacement at node	+9 %	17%
Strain SG5/8	+9%	23%
C2		
Global in-plane stiffness	0%	4%
Out-of-plane displacement at node	-24%	-22%
Strain SG5/8	-6%	6%

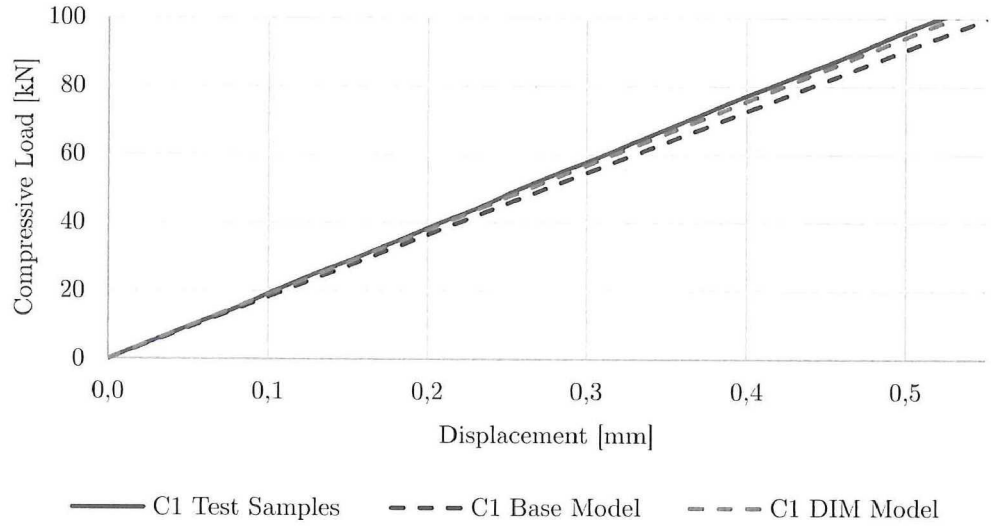

Figure 7.1: Displacement versus load of C1 test samples, base model and improved dimensional model

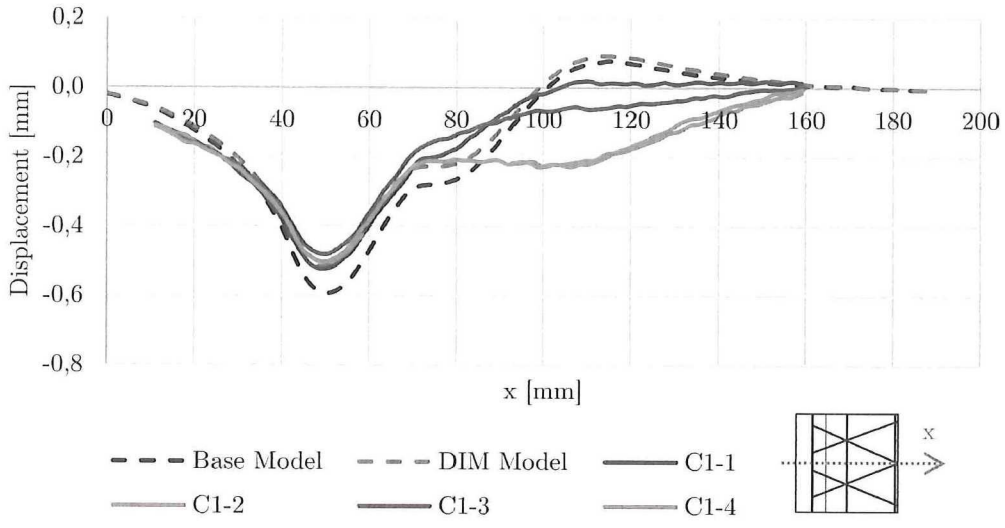

Figure 7.2: Out-of-plane displacement at 93kN along middle line of C1 test samples, base model and improved dimensional model

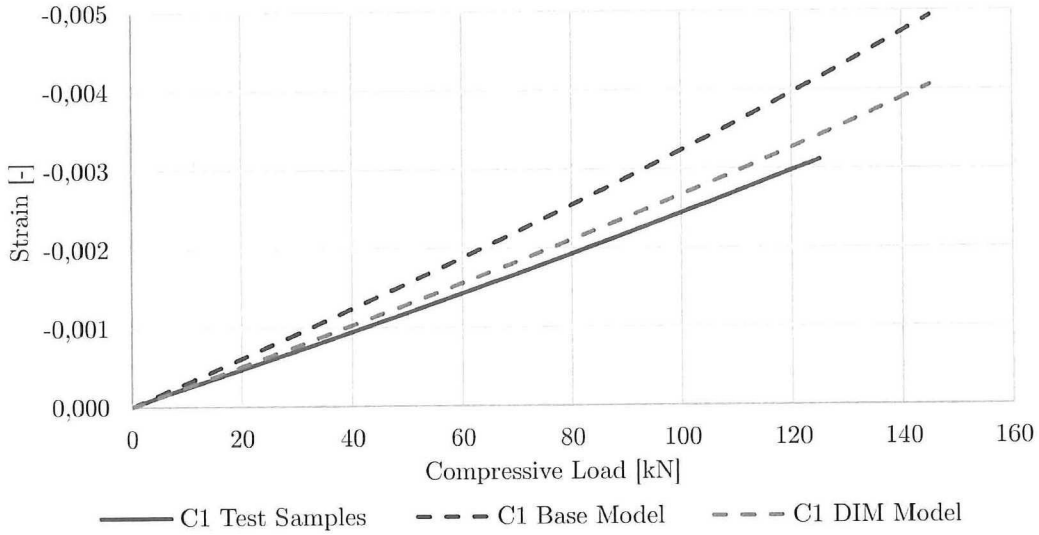

Figure 7.3: Strain measured at outer helical ribs of C1 test samples, base model and improved dimensional model

7.1.3 Material Properties

Material properties have a large effect on the stiffness of a structure. As already mentioned the properties of the aluminum will not be much different from the assumed properties. So any difference will most likely be in the adhesive and the CFRP.

The adhesive shear stiffness will have a negligible effect on the global stiffness and hence will not show in the the global displacement. Any effect of the adhesive stiffness will be most noticeable in the strain gages placed on the aluminum flanges. Increasing the modulus of the adhesive by 35% does hardly change the strain values in the aluminum flanges as can be seen in Figure 7.4.

It was already shown in Section 5.2.3 that the fiber volume fractions were 3.7% higher than values indicated in the data sheet provided by the supplier. Since the modulus of a composite material depends on its ratio and the stiffness of its constituents, the increased FVF will result in a higher modulus. For small increases in FVF it is assumed that modulus can be calculated using the rule of mixtures ($E_c = v_f * E_f + (1 - v_f) * E_m$). The relation between FVF and the modulus in fiber direction can further be simplified to a linear relation assuming that the modulus of the matrix is small compared to the modulus of the fibers. In this case an increase in FVF of 3.7% will result in an increase in modulus of 6.2%. It was shown that the rib sections in between the nodes and laminate had a relatively low FVF and was different from other sections of the panel. Those sections were assigned lower modulus values (4.2% increase) than the rest of the panel.

The increased modulus of the material directly increases the global in-plane stiffness. While the improved material properties model shows a perfect match in terms of global in-plane stiffness for both configurations (as can be seen in Figure 7.5) the out-of-plane stiffness correlation has hardly improved (as can be seen in Figure 7.6). The bending stiffness increases slightly which improves the correlation between the C1 model and the test samples but makes

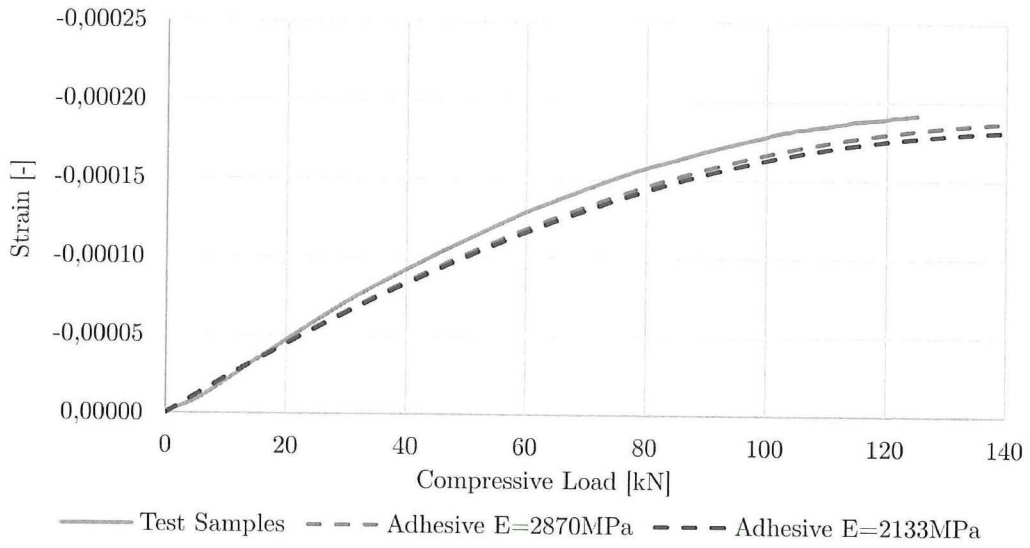

Figure 7.4: The effect of adhesive Young's Modulus on the strain measured at the aluminum flanges.

correlation slightly worse for the C2 configuration.

Looking at the local strain values little improvement has been gained by improving the material properties as can be seen in Figure 7.7. This does not come as a surprise since strain and stiffness are closely related. By scaling the material properties slightly the behavior has not changed drastically. Load distribution and out-of-plane bending behavior will still be similar so the improvements in strain are practically limited to the scaling of the modulus.

Table 7.4: Comparison improved material properties (FVF) model with test samples and base model

	FVF model	Improvement
C1		
Global in-plane stiffness	-1%	4%
Out-of-plane displacement at node	+22%	4%
Strain SG5/8	+25%	7%
C2		
Global in-plane stiffness	0%	4%
Out-of-plane displacement at node	-10%	-8%
Strain SG5/8	+5%	7%

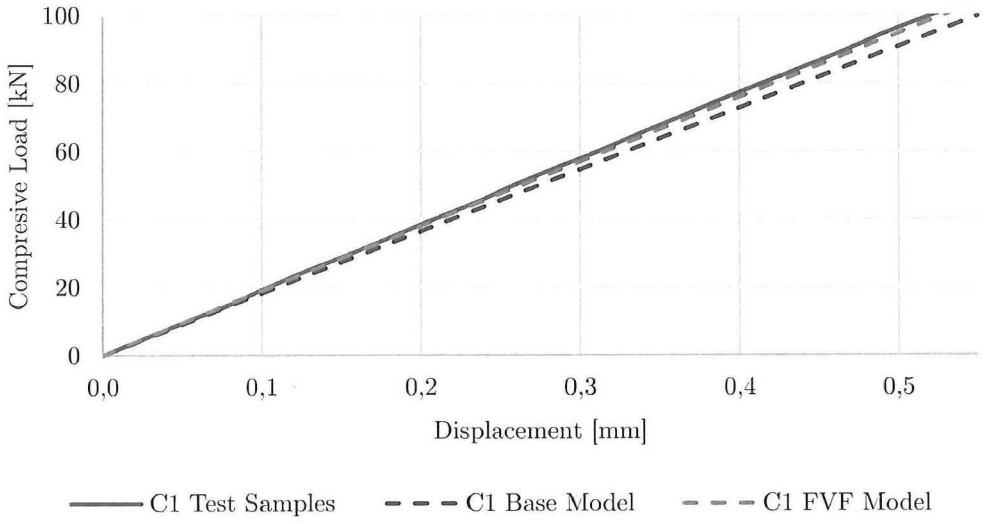

Figure 7.5: Displacement versus load of C1 test samples, base model and improved material properties model

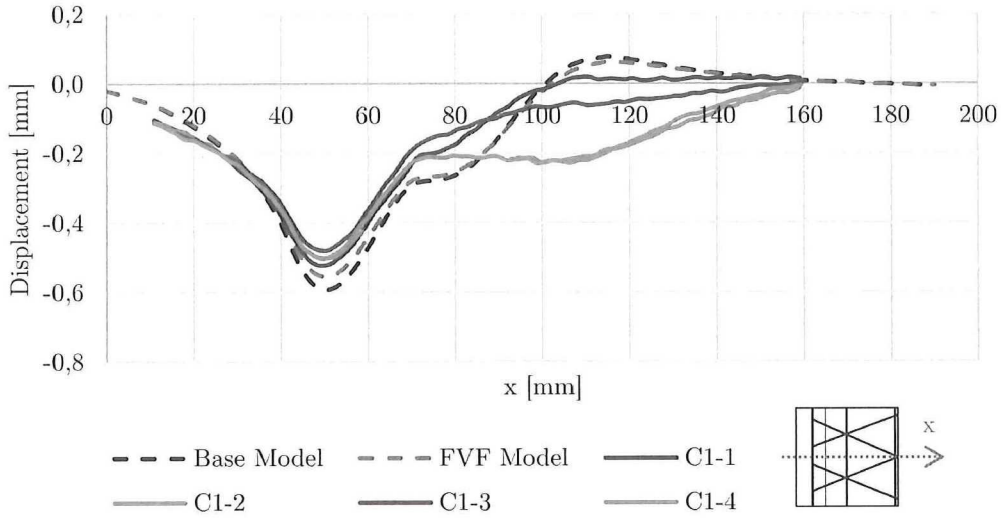

Figure 7.6: Out-of-plane displacement at 93kN along middle line of C1 test samples, base model and improved material properties model

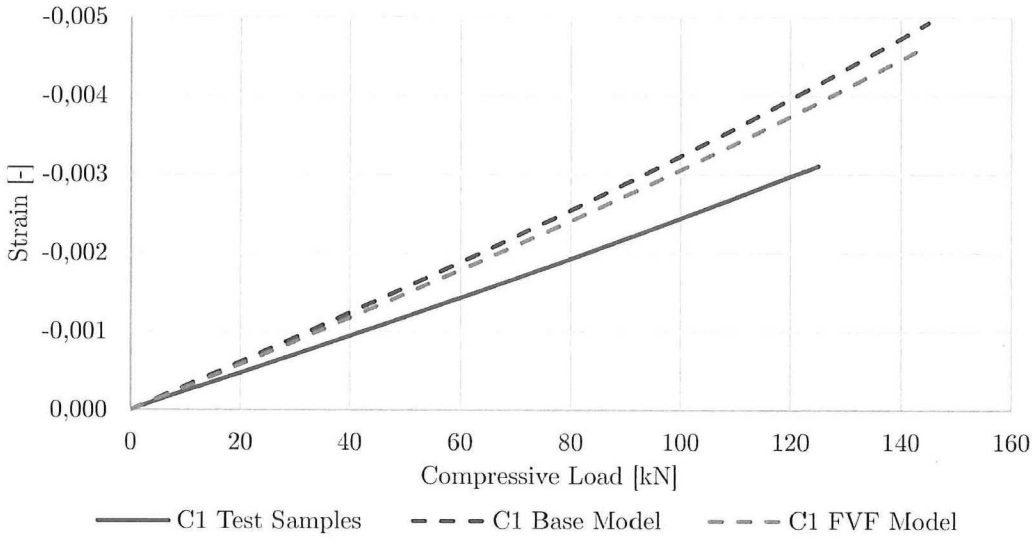

Figure 7.7: Strain measured at outer helical ribs of C1 test samples, base model and improved material properties model

7.1.4 Thermal Effects

The cure induced curvature has been mentioned a few times with regard to the out-of-plane behavior but it will affect the global in-plane stiffness as well. Implementing the curvature in the model would be a logical improvement. Implementing requires either a thermal step prior to the loading step to deform the panel to the initial shape or the curvature has to be implemented in the CAD models. The later would be infeasible for the current set-up of the model as discussed in Section 3.3.2. It has been shown in Section 5.2.4 that with a thermal step the curvature of the panel can be acquired quite accurately. However the adhesive, bonded L-beams and aluminum ring make applying a thermal step very complex due to the differences in thermal expansion coefficient. It was decided that this is for future research.

7.1.5 Conclusions

Stiffness

While the base model already showed good correlation in terms of global elastic behavior, improvements can still be made. Assigning the correct material properties might not have resulted in much improvement for this test sample model, it might in situations where the material is loaded in tension. To be conservative in defining the material properties the lowest modulus values were used. Which in this case corresponded with the applied compression loading. In a tension load situation assigning the lowest values might not be conservative after all. In that case assigning the correct material properties will most likely result in more accurate results. For this reason the correct material assignment improvement is incorporated in the final improved model.

While the dimensional improvement on itself gives a great result knowing that the material properties in the model do not match those in the test sample, both improvements should be incorporated in the final improved model. Incorporating all improvements in a single model results in a slight over-prediction of global in-plane stiffness for both the C1 and C2 configuration as can be seen in Figure 7.8. Where the base model under-predicted the stiffness of the C1 configuration by roughly 5% and C2 by 4%, the improved model over-predicts the stiffness by 2% and 5% respectively. The same can be seen for the out-of-plane displacement, which is reduced for both the C1 and C2 model. For the C1 configuration the base model was over-predicting the displacement so the reduction results in an almost perfect correlation between the test samples and the improved model, as can be seen in Figure 7.9. The C2 test samples already showed more out-of-plane displacement than the base model, so this reduction means the under-prediction has increased to 30%.

The test results show a non-linearity which is not fully captured by the models. The non-linear behavior shown by the model is not as strong as for the test samples. In Figure 7.11 the global in-plane stiffness is plotted versus displacement where it can be observed that the initial C1 test sample stiffness matches the improved model quite well but starts deviating after about 0.3mm displacement. While the models indicate a slight decrease in stiffness from the beginning, the C2 test samples clearly show an increasing stiffness till 0.2mm displacement after which it will start dropping quite rapidly. This initial increase in stiffness can also be seen for the C1 test samples but is less strong. The initial non-linear behavior of the test samples can be contributed to the curvature caused by thermal strains, presented in Section 5.2.4. Due to the shrinkage of the skin the samples are curved towards the skin side. Applying a compression load will result in an out-of-plane bending in the opposite direction. This will straighten the panel first and by doing so increase its stiffness, after which it will start bending out-of-plane and reduce the stiffness again. The curvature due to cure, which was similar for the C1 and C2 test samples, reduces the in-plane stiffness of the thinner and softer C2 test samples more than it affects the C1 test sample stiffness. The maximum stiffness for the C2 test panels, at 0.2mm displacement when the panel will be straight, is only 3% lower than the model predicted for a straight panel. Averaging over 93kN or 0.54mm results in an over-prediction of 5% due to the low initial stiffness as well as the low stiffness at 93kN. Since the C1 test samples are less affected by the curvature both the maximum stiffness and the averaged stiffness till 93kN are only 2% lower than the predicted stiffness values. This however does not explain the stronger non-linear behavior of the test-samples at displacements higher

than 0.3mm.

While the improved model of the C1 configuration matches very well with the test samples to and at a load of 93kN the non-linear behavior will result in much less accurate predictions at higher loads. This non-linearity already affects the prediction of the C2 model at a load of 93kN and gets even worse for higher loads. The C2 test sample also shows higher out-of-plane displacements at 93kN than the C1 test samples which explains the worse non-linearity in global in-plane stiffness. This indicates the models are still over-predicting the bending stiffness of the panels.

Table 7.5: Comparison improved model with base model

	Base Model	Improved Model	Improvement
C1			
Global in-plane stiffness	-5%	+2%	3%
Out-of-plane displacement at node	+26%	+3%	23%
Strain SG5/8	+32%	+3%	29%
C2			
Global in-plane stiffness	-4%	+5%	-1%
Out-of-plane displacement at node	-2%	-30%	-28%
Strain SG5/8	+12%	-11%	1%

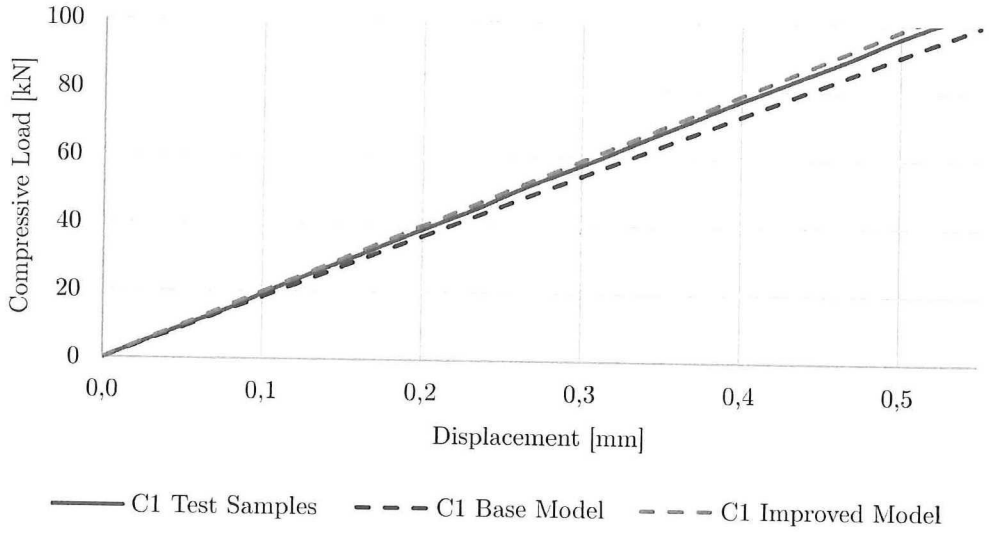

Figure 7.8: Displacement versus load of C1 test samples, base model and improved model

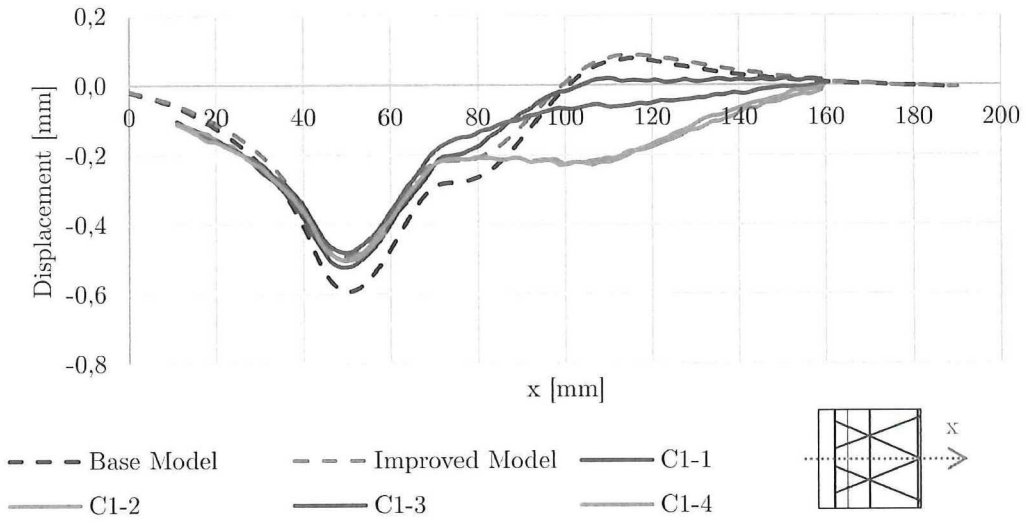

Figure 7.9: Out-of-plane displacement at 93kN along middle line of C1 test samples, base model and improved model

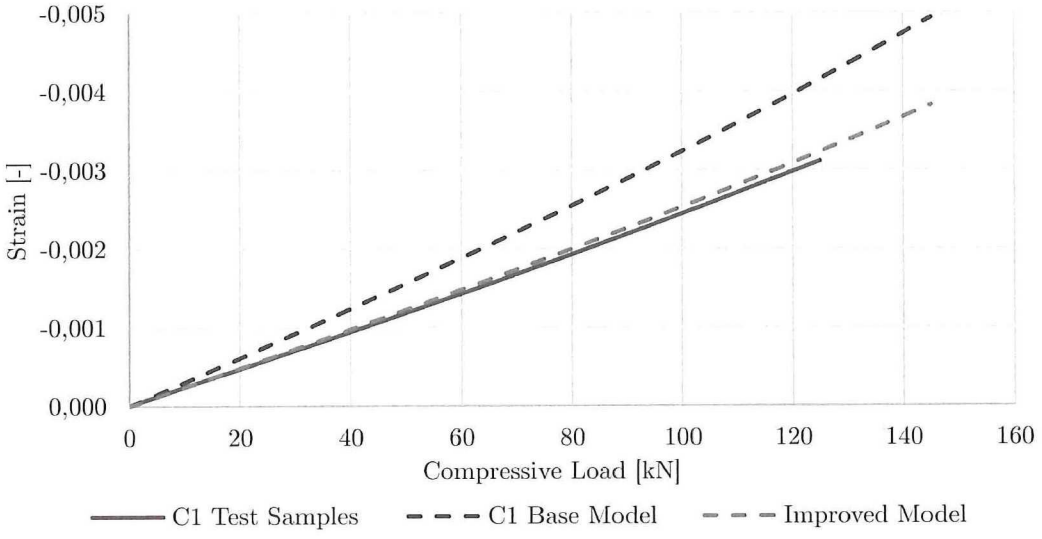

Figure 7.10: Strain measured at outer helical ribs of C1 test samples, base model and improved model

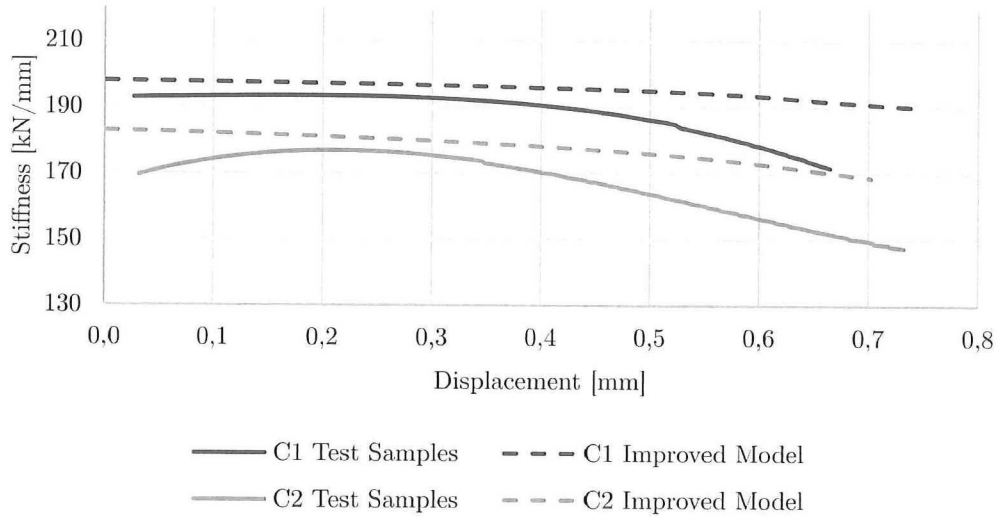

Figure 7.11: Global in-plane stiffness versus displacement for test samples and improved FEM models

Strength

While the improved models actually improved in capturing the stiffness behavior, the strength predictions worsened. The increased dimensions of the ribs have lowered the strains in the skin, making this area less critical. At the same time the increased dimensions of the rib also resulted in a larger footprint of the rib on the laminate. So while the strains in the skin are lowered, so are the strains in the laminate. The improved models indicate the same critical areas, but the expected failure loads have gone up by 20% in the laminate, skin and ribs and a little under 10% in the adhesive and aluminum. The over-prediction of strength for the C1 test samples increased to 47% and to 44% for the C2 test samples.

It was shown that the prediction of stiffness at loads above 93kN is becoming less accurate due to the strong non-linear behavior. This also makes predictions of strength, which are at loads above 147kN, unreliable. Also no improvements are made on predicting local stress fields at and around the rib-laminate interface.

Table 7.6: Predicted compression loads required for failure to occur at key regions

Location	C1 Base Model	C1 Improved Model	C2 Base Model	C2 Improved Model
Adhesive	117 kN	124 kN	82 kN	88 kN
Aluminum	185 kN	203 kN	142 kN	154 kN
Laminate	172 kN	206 kN	147 kN	167 kN
Ribs	200+ kN	300+ kN	189 kN	216 kN
Skin	163 kN	194 kN	153 kN	182 kN

7.2 Global Model Verification

The modeling and testing of the test samples was done in order to verify the global FEM model and modeling approach which was described in Chapter 3. While the improvements in the test sample model resulted in a better prediction of global elastic behavior of the test samples they will not necessarily be applicable to the global model. Of the three main improvements made to the test sample models the material property and dimensional improvement do not improve the modeling approach but are required to make the model more representative for the actual test samples. The material properties and dimensions of the geometry are inputs in the model and not part of the model itself. Material properties will have to be obtained separately. Any difference in geometry as result of manufacturing imperfections has to be accounted for in the optimization strategy of which the FEM model is just a part. So either good dimension control, to make sure that the manufactured part is as designed, or a good method of predicting dimensions, to make sure that the designed part is as manufactured, is required for optimization. It should however be said that the dimensions have a large effect on the behavior of the structure, so correct implementation of an accurate geometry is important.

The third improvement that was implemented in the test sample models was the correct material assignment to make sure tensile and compressive properties are assigned accordingly. It was observed that implementing this improvement had little to no effect on the global elastic behavior in this case. However it could improve the accuracy of the model in other cases and hence is implemented in the global model.

An improvement that was not implement in the test sample models was the curvature caused by thermal strains. This is closely related to the dimensional improvement discussed earlier. This curvature has to be either implemented in the model input or predicted by the model. It has been shown in Section 5.2.4 that the FEM model can be used to predict thermal deformations quite well. While technical difficulties prevented the implementation of the curvature into the FEM model for this thesis, incorporating a thermal step prior to loading will improve the accuracy of the global model.

Chapter 8

Conclusions and Recommendations

The main objective of this research, as stated in Chapter 1, is developing a versatile lightweight solution for edge-of-panel load introductions in grid-stiffened composite structures. Conclusions regarding this objective are drawn based on the different aspects of the development described in the previous chapters. The conclusions will be presented in the first section of this chapter after which follow the recommendations for future research.

8.1 Conclusions

The research has yielded great results with regard to the main objective by addressing all the theoretical and practical aspects of a load introduction in grid stiffened composites. How the different aspects are addressed is outlined in the following conclusions:

- The feasibility of transforming a grid into a monolithic laminate by interweaving of rib and laminate plies has been proven by manufacturing of three different types of samples. These samples have distinctively different designs and show a similar manufacturing quality, proving the rib-to-laminate design can be used for different grid designs and assuring versatility (Section 3.2 and Chapter 5).
- By overlapping the rib and laminate plies over a finite length, local build-up of plies and increased thicknesses of the laminate can be prevented (Section 5.2.2). Since the rib plies are terminated and do not become part of the laminate, the orientation of the laminate plies is independent of the orientation of the helical ribs (Section 3.2). This allows for optimization of the laminate region and makes the rib-to-laminate concept versatile.
- Interweaving of rib and laminate plies results in a design that has good load transfer capabilities (Section 6.2). However the stress concentrations at the rib-laminate interface may have led to early failure (Section 6.3.4).

- Parametrization of the load introduction zone allows for redistribution of loads which can be used for mass optimization (Section 3.4).

- The complex nature of laminate load introduction zones requires optimization strategy to obtain the optimum mass design (Section 3.4.8).

- The orientation of the laminate plies can be tailored to reduce stresses in the adhesive and rib-laminate interface (Section 3.4.7) but also has a strong influence on the thermal deformation of the laminate caused by the cure cycle in combination with the asymmetry of the structure. The deformation of the laminate can be predicted quite well by implementing a thermal step in the FEM model (Section 5.2.4).

- The asymmetry of the grid section results in an out-of-plane deformation caused by the cure cycle. This out-of-plane deformation can be obtained easily using a DIC system and can be predicted quite well by implementing a thermal step in the FEM model (Section 5.2.4).

- The layup strategy of the rib plies has a strong effect on the final dimensions of the ribs and the total mass of the panel (Section 5.2.2).

- The FVF of the test samples was significantly higher than the nominal FVF. No link between the manufacturing strategy and the high FVF was found. The most likely cause is that the wrong material is supplied by the supplier (Section 5.2.3).

- The dimensional accuracy of the test samples of a single configuration is very similar (Section 5.2.2) which resulted in great grouping in terms of global in-plane stiffness (Section 6.2).

- The bending stiffness of the test panels can be correlated with the FEM model by correlating the out-of-plane displacements (Section 6.3.1). These out-of-plane displacements can be obtained easily and accurately during testing by using a DIC system (Section 6.1.1).

- The global elastic in-plane behavior can be predicted well by FEM models but test samples show a stronger non-linearity in global stiffness. The initial stiffening of the test samples can be attributed to the thermal deformations. The test samples show a stronger decrease in global in-plane stiffness and a higher out-of-plane displacement than the model, which indicates the model is over-predicting the bending stiffness of the panels. Modeling of the curvatures at the laminate and grid section, either by implementing a thermal step in the FEM model or by modeling the curvature in CAD, would result in a better correlation of the initial non-linear elastic behavior of the test samples (Section 7.1.5).

- Assigning the proper tensile or compressive modulus to the CFRP sections did not result in a noticeable improvement in correlation between the FEM model and the test samples (Section 7.1.1). However the correct assignment of modulus properties may improve the correlation in other design or load cases and hence is implemented in the global modeling approach (Section 7.2).

- Accurate modeling of the test sample dimensions greatly improves the correlation between the FEM model and test samples in terms of global in-plane stiffness, bending stiffness as well as local strain values (Section 7.1.2). Hence it is important to model or predict the dimensions accurately (Section 7.2).
- The increased FVF has little effect on the bending stiffness of the structure and local strain values. However it has a strong effect on the global in-plane stiffness (Section 7.1.3).
- Combining the dimensional and material properties (FVF) FEM model improvement resulted in a slight over-prediction of global in-plane stiffness (Section 7.1.5).
- The improved FEM model over-predicts the strength significantly (Section 7.1.5). Although the model predicts the failure location quite well, better failure criteria or local models would be required to improve prediction of failure load (Section 6.3.2).
- Two out of three improvements implemented in the test sample FEM model, the material properties and dimensions, are based on manufacturing defects and as such not implemented in the global model. For better model correlation, better control of material and dimensions is required to make sure the manufactured part is as designed (Section 7.2).

8.2 Recommendations

While the presented work yields good results with regard to its objectives, additional steps can be made that will build on the performed work and aid in the global development of grid-stiffened composite structures. Recommendations for further research:

- Improve layup strategy in order to achieve better dimensional control and nodal quality by preventing excessive length of fibers while still preventing shift of fibers.
- Create better dimensional control and/or predictions by improved expansion models for rubber tooling.
- Investigate under-prediction of out-of-plane displacement by the model.
- Implement thermal step in the FEM model to predict and account for thermal stresses and deformations caused by cure cycle and asymmetry in the structure.
- Modeling of curved structures to improve the prediction of out-of-plane behavior.
- For better understanding of the failure initiating or failure sequence, stop tests after initial failure and investigate using additional techniques e.g. microscopy.
- Perform tests in tension and/or combined loading.
- Implement FEM model in optimization strategy to find the optimum mass design.
- Implement better failure criteria for composite and adhesive to improve strength prediction and correlation.
- Further investigate the high FVF for better control of material properties.

References

[1] Vasiliev, V., Barynin, V., and Razin, A., "Anisogrid composite lattice structures Development and aerospace applications," *Composite Structures*, Vol. 94, No. 3, Feb. 2012, pp. 1117–1127.

[2] Baker, D. J., Fudge, J., Ambur, D. R., and Kassapoglou, C., "Optimal design and damage tolerance verification of an isogrid structure for helicopter application," *44th AIAA/ASME/ASCE/AHS Structures, Structural Dynamics, and Materials Conference*, Norfolk, Virginia, USA, 2003, pp. 1–19.

[3] Díaz, V., Cardone, T., and Ramusat, G., "Advanced materials & structural concepts for interstages structures of future expendable launchers," *13th European Conference on Spacecraft Structures, Materials and Environmental Testing*, Vol. 2014, Braunschweig, Germany, 2014, pp. 1–6.

[4] Maes, V. K., "Design, Analyis, Optimization and Testing of Grid-Stiffened Composite Structures," 2015.

[5] Chen, H.-J. and Tsai, S. W., "Analysis and Optimum Design of Composite Grid Structures," *Journal of Composite Materials*, Vol. 30, No. 4, March 1996, pp. 503–534.

[6] Zhang, Z., Chen, H., and Ye, L., "A Stiffened Plate Element Model for Advanced Grid Stiffened Composite Plates/Shells," *Journal of Composite Materials*, Vol. 45, No. 2, May 2010, pp. 187–202.

[7] Wodesenbet, E., Kidane, S., and Pang, S.-S., "Optimization for buckling loads of grid stiffened composite panels," *Composite Structures*, Vol. 60, No. 2, May 2003, pp. 159–169.

[8] Jadhav, P. and Mantena, P. R., "Parametric optimization of grid-stiffened composite panels for maximizing their performance under transverse loading," *Composite Structures*, Vol. 77, No. 3, Feb. 2007, pp. 353–363.

[9] Collier, C., Yarrington, P., and Van West, B., "Composite, Grid-Stiffened Panel Design for Post Buckling Using HyperSizer," *43rd AIAA/ASME/ASCE/AHS/ASC Structures,*

Structural Dynamics, and Materials Conference, American Institute of Aeronautics and Astronautics, Reston, Virigina, USA, April 2002, pp. 1–17.

[10] Totaro, G. and De Nicola, F., "Recent advance on design and manufacturing of composite anisogrid structures for space launchers," *Acta Astronautica*, Vol. 81, No. 2, Dec. 2012, pp. 570–577.

[11] Huybrechts, S. M., Meink, T. E., Wegner, P. M., and Ganley, J. M., "Manufacturing theory for advanced grid stiffened structures," *Composites Part A: applied science and manufacturing*, Vol. 33, 2002, pp. 155–161.

[12] Huybrechts, S. and Meink, T. E., "Advanced Grid Stiffened Structures for the Next Generation of Launch Vehicles," *IEEE Aerospace Conference*, Aspen, Colorado, USA, 1997, pp. 263–270.

[13] Bakhvalov, Y. O., Petrokovskii, S. A., Polynovskiy, V. P., and Razin, A. F., "Composite irregular lattice shells designing for space applications," *ICCM-17 International Committee on Composite Materials*, No. Table 1, Edinburgh, Scotland, UK, 2009, pp. 1–10.

[14] Vasiliev, V. and a.F. Razin, "Anisogrid composite lattice structures for spacecraft and aircraft applications," *Composite Structures*, Vol. 76, No. 1-2, Oct. 2006, pp. 182–189.

[15] Razin, A. F. and Vasiliev, V. V., "Development of composite anisogrid spacecraft attach fitting," *11th European Conference on Composite Materials*, Rhodos, Greece, 2004, pp. 1–9.

[16] Vasiliev, V. V., Razin, A. F., Totaro, G., and Nicola, F. D., "Anisogrid Conical Adapters for Commercial Space Application," *AIAA/CIRA 13th International Space Planes and Hypersonics Systems and Technologies*, Capua, Italy, 2005, pp. 1–9.

[17] Bakhvalov, Y. O., Molochev, V. P., Petrokovskii, S. A., Barynin, V. A., Vasiliev, V. V., and Razin, A. F., "Proton-M Composite Interstage Structures: Design, Manufacturing and Performance," *European Conference for Aerospace Sciences (EUCASS)*, Moscow, Russia, 2005, pp. 1–7.

[18] Torres, J., Blanco, N., Olmo, E. D., and Grande, E., "Virtual testing of a composite cylindrical lattice structure for aerospace applications," *SIMULIA, 2011 SIMULIA Customer Conference*, Barcelona, Spain, 2011, pp. 1–16.

[19] Sjölander, J., *FE Analysis of a LAS-937 upper interface during combined compression loading*, Ph.D. thesis, KTH (Royal Institute of Technology), 2011.

[20] Diaz, V., Olmo, E. D., and Frövel, M., "Design & Development of Advanced Composite Isogrid Structural Solutions for Primary Structures of Future Reusable Launch Vehicle," *11th European Conference on Spacecraft Structures, Materials and Mechanical Testing*, No. 1, Toulouse, France, 2009, pp. 1–8.

[21] Sanford, G., Higgins, J. E., and Welsh, J., "Advanced Iso-Grid Fairing Qualification Test For Minotaur Launch Vehicle," *14th International Conference on Composite Materials*, San Diego, California, USA, 2003, pp. 1–10.

[22] Wegner, P. M., Higgins, J. E., and VanWest, B. P., "Application of Advanced Grid-Stiffened Structures Technology to the Minotaur Payload Fairing," *43rd AIAA/ASME/ASCE/AHS/ASC Structures, Structural Dynamics and Materials Conference*, Denver, Colorado, USA, 2002, pp. 1–7.

[23] European Space Agency, "Ariane 6 Project Request For Consultation for Ariane 6 Key Launcher Elements . ATTACHMENT II : Technical Conditions," Tech. rep., European Space Agency, 2013.

[24] Bailie, J. A., Ley, R. P., and Pasricha, A., "A summary and review of composite laminate design guidelines," Tech. rep., Northtop Grumman, El Segundo, California, USA, 1997.

[25] 3M, "Technical Datasheet Scotch-Weld 9323 B/A," 2010.

[26] Kassapoglou, C., *Design and Analysis of Composite Structures*, 1st ed., 2010.

Appendix A

Test Data

In Chapter 5 and Chapter 6 the test data is often averaged to increase clarity. Since valuable information such as scatter, can get lost in averaging results, the raw test data is presented in this appendix.

A.1 Strain Gage Data

In Section 6.3.3 the typical strain gage data was shown. The strain gage data for all strain gages placed on C1 test samples is presented in Figure A.2- A.15. Their location is indicated in Figure A.1.

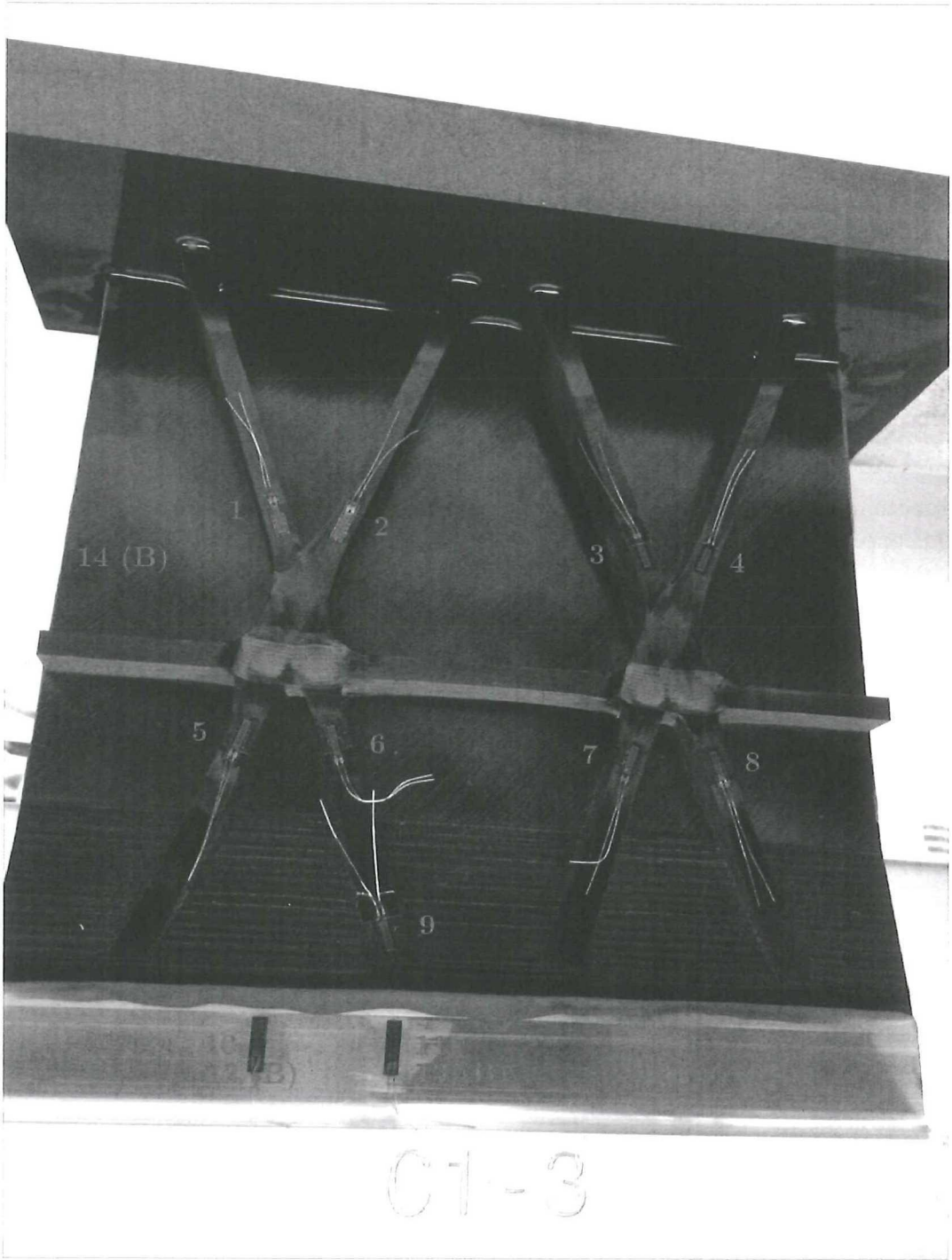

Figure A.1: Location of strain gages. (B) indicates strain gage on back side

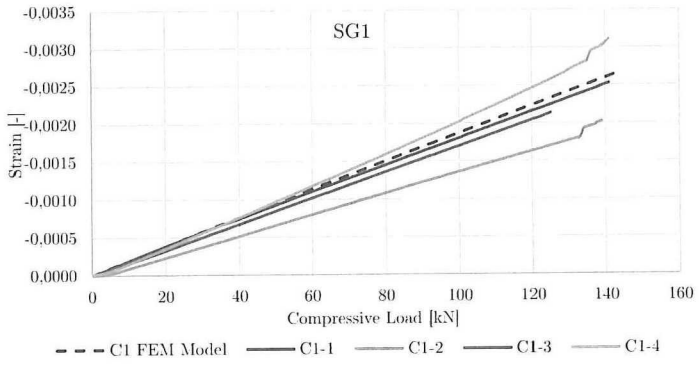

Figure A.2: Strain measured with SG1 on C1 test samples compared to C1 base model

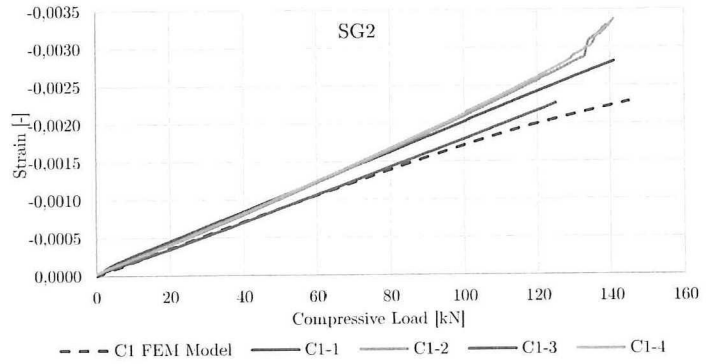

Figure A.3: Strain measured with SG2 on C1 test samples compared to C1 base model

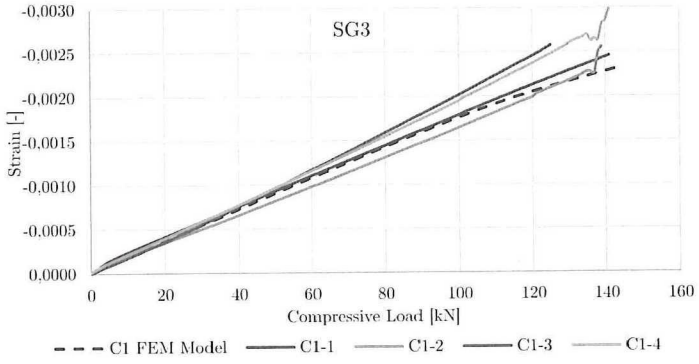

Figure A.4: Strain measured with SG3 on C1 test samples compared to C1 base model

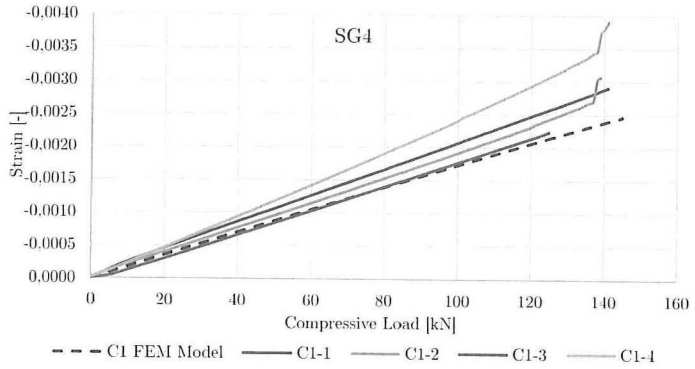

Figure A.5: Strain measured with SG4 on C1 test samples compared to C1 base model

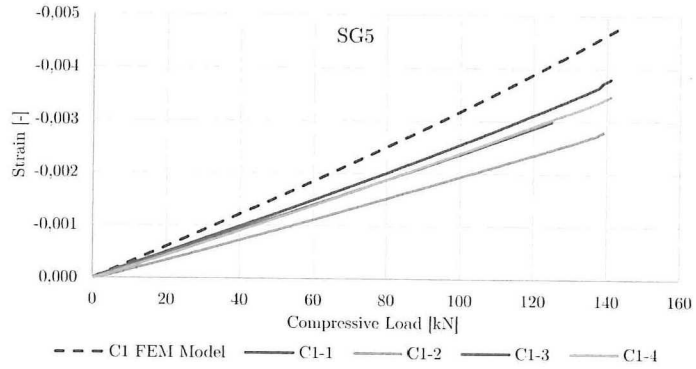

Figure A.6: Strain measured with SG5 on C1 test samples compared to C1 base model

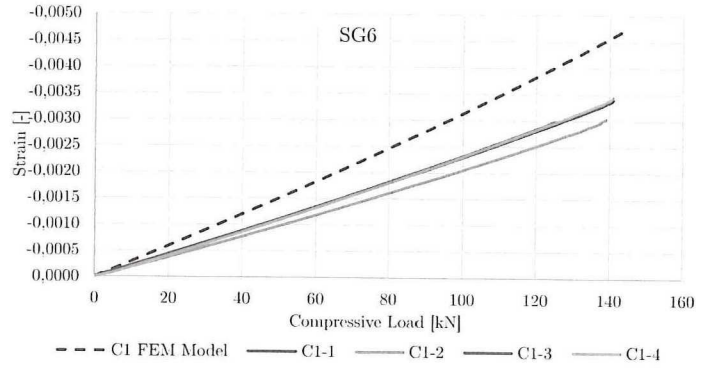

Figure A.7: Strain measured with SG6 on C1 test samples compared to C1 base model

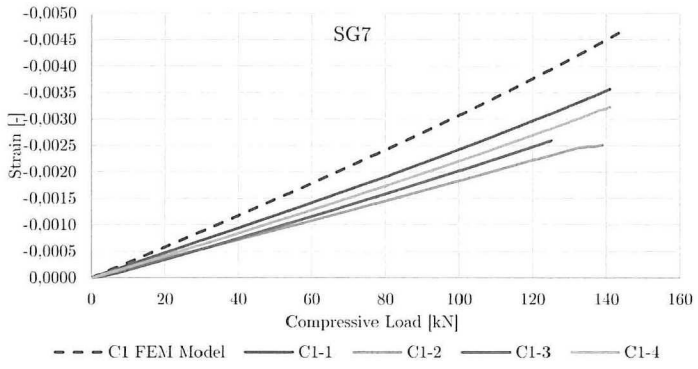

Figure A.8: Strain measured with SG7 on C1 test samples compared to C1 base model

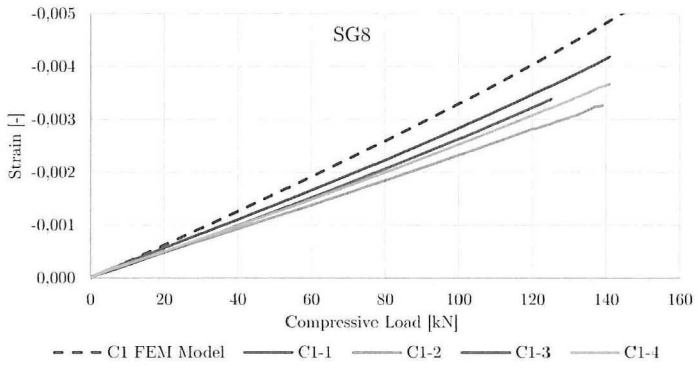

Figure A.9: Strain measured with SG8 on C1 test samples compared to C1 base model

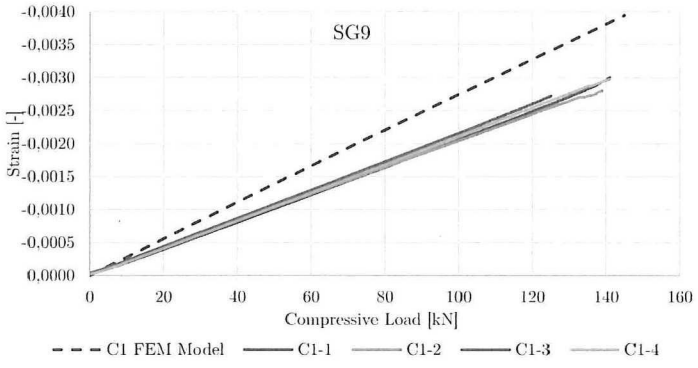

Figure A.10: Strain measured with SG9 on C1 test samples compared to C1 base model

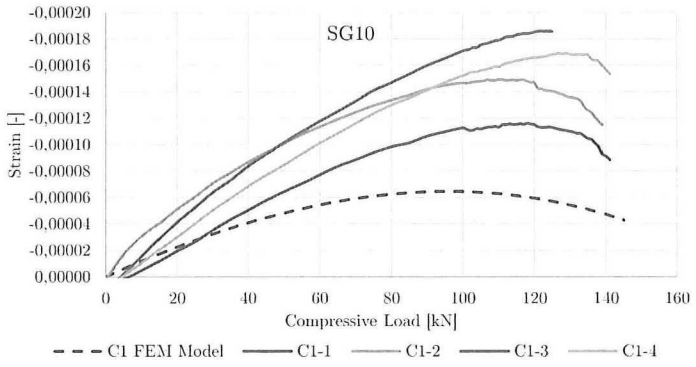

Figure A.11: Strain measured with SG10 on C1 test samples compared to C1 base model

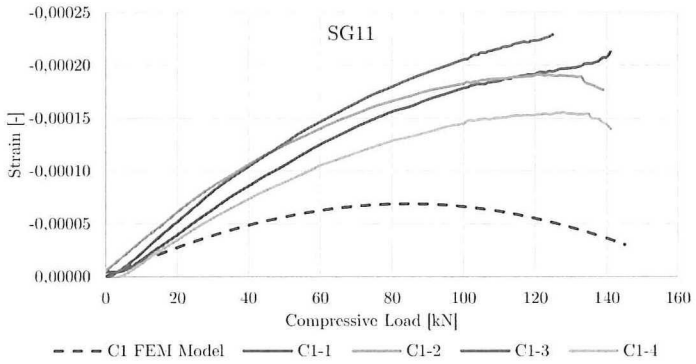

Figure A.12: Strain measured with SG11 on C1 test samples compared to C1 base model

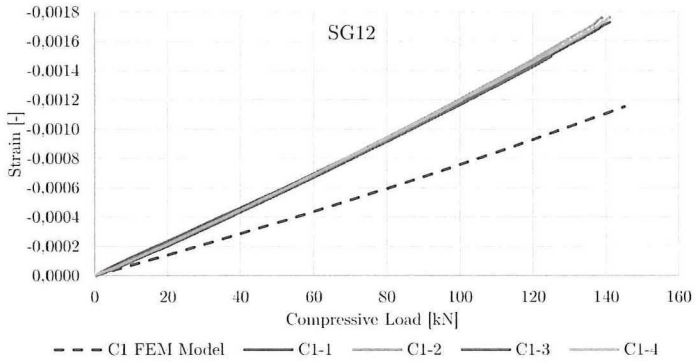

Figure A.13: Strain measured with SG12 on C1 test samples compared to C1 base model

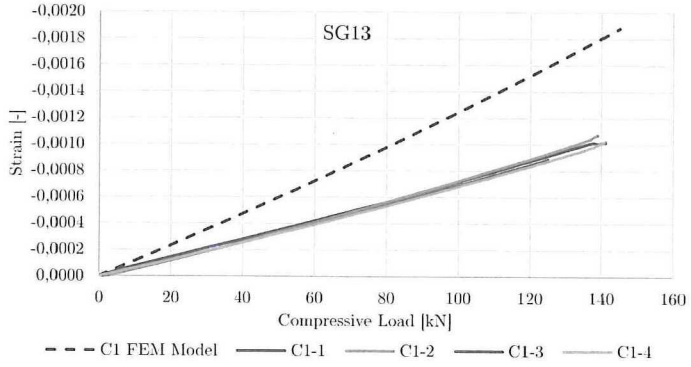

Figure A.14: Strain measured with SG13 on C1 test samples compared to C1 base model

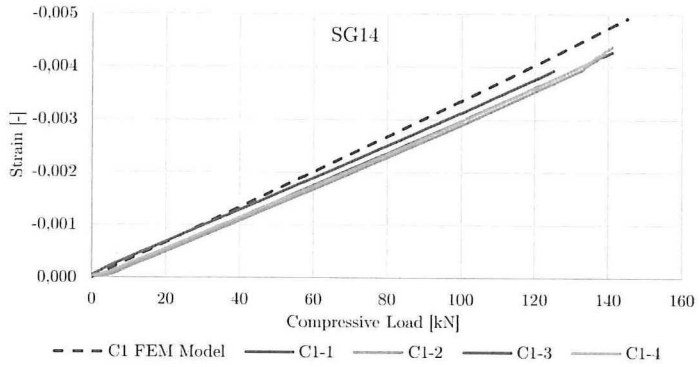

Figure A.15: Strain measured with SG13 on C1 test samples compared to C1 base model

A.2 Panel Curvature

In Section 5.2.4 the average of the curvatures measured with the DIC system and dial indicator were shown. In this section all measurements are shown. A slight variation in curvature can be observed, which can be caused by multiple manufacturing defects, for example non-perfect layup, material scatter, autoclave tooling flatness or temperature differences within product.

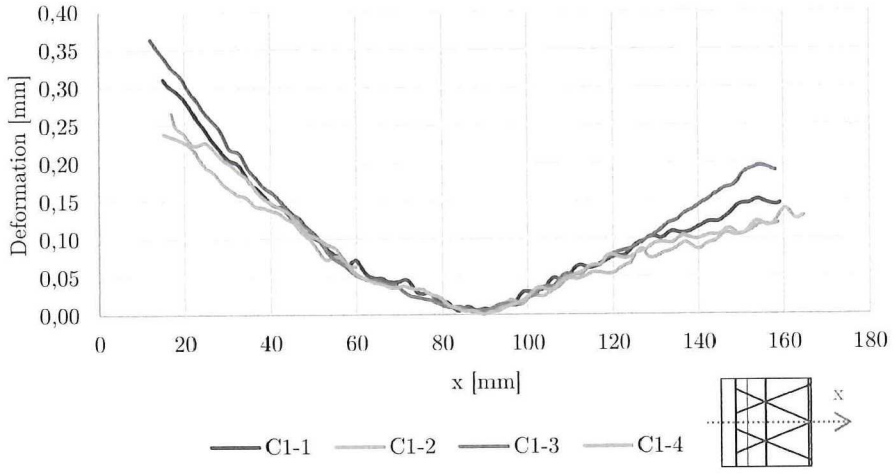

Figure A.16: Out-of-plane deformation along middle line (indicated by x) for C1 test samples obtained by DIC

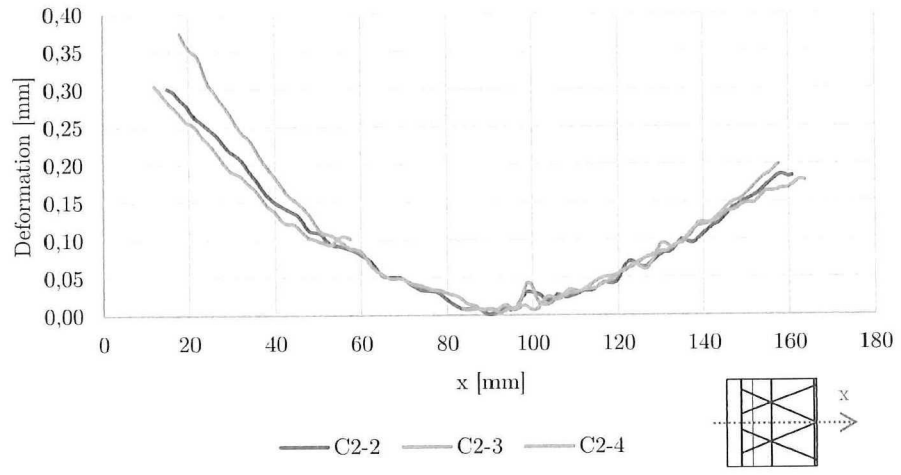

Figure A.17: Out-of-plane deformation along middle line (indicated by x) for C2 test samples obtained by DIC

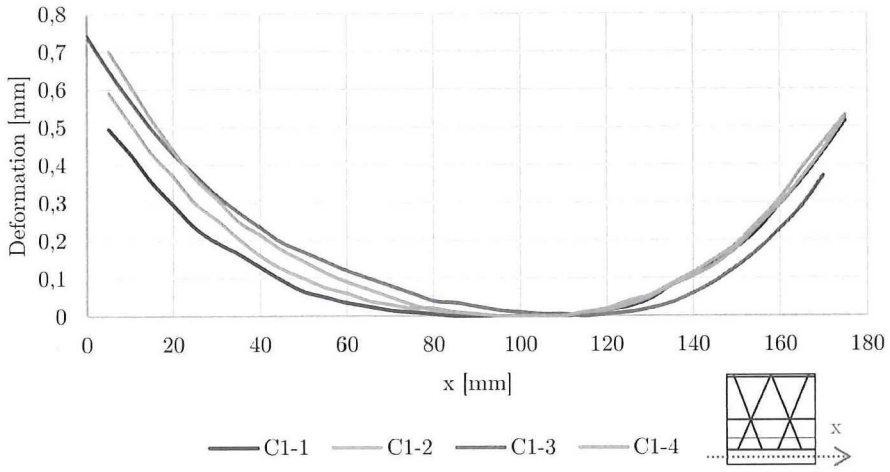

Figure A.18: Out-of-plane deformation along laminate (indicated by x) for C1 test samples obtained by dial indicator

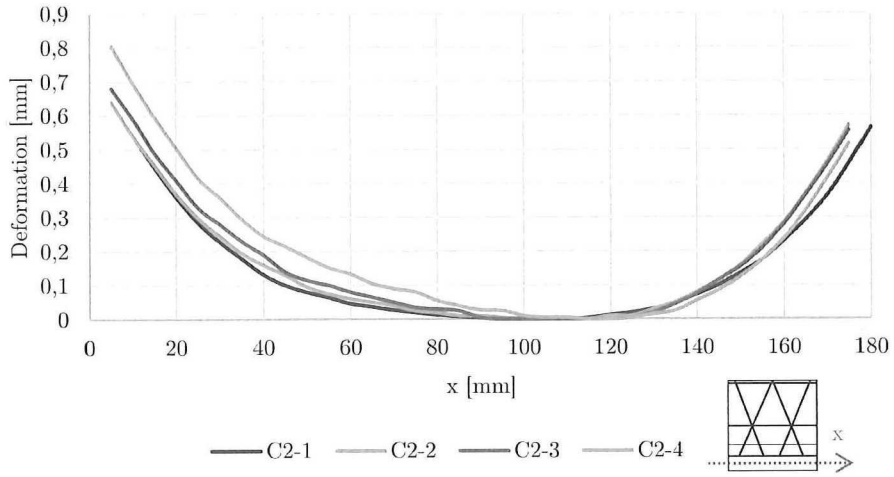

Figure A.19: Out-of-plane deformation along laminate (indicated by x) for C2 test samples obtained by dial indicator

A.3 DIC Data

An additional strain gage is placed on the skin on the DIC side of the samples. The strain in the loading direction captured by the strain gage (SG14) and the DIC is compared in Figure A.20. It can be seen that strain obtained by the DIC system is on average within 2% of the strain measured by the strain gage. Based on this it can be concluded that the DIC can also be used to correlate and verify the FEM models.

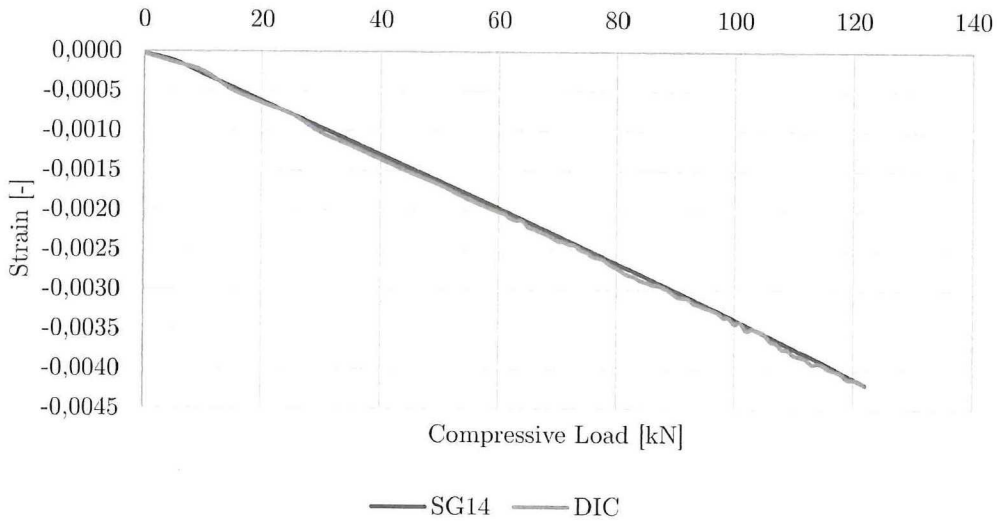

Figure A.20: Comparison of strain obtained by DIC and SG

Appendix B

Model Improvement

In this appendix the additional correlation results are shown for the improved models presented in Chapter 7.

B.1 C1 Configuration

In Section 7.1.1 the effects of the material assignment were described. In Figure B.1- B.3 the effects on the correlation with the FEM model are shown.

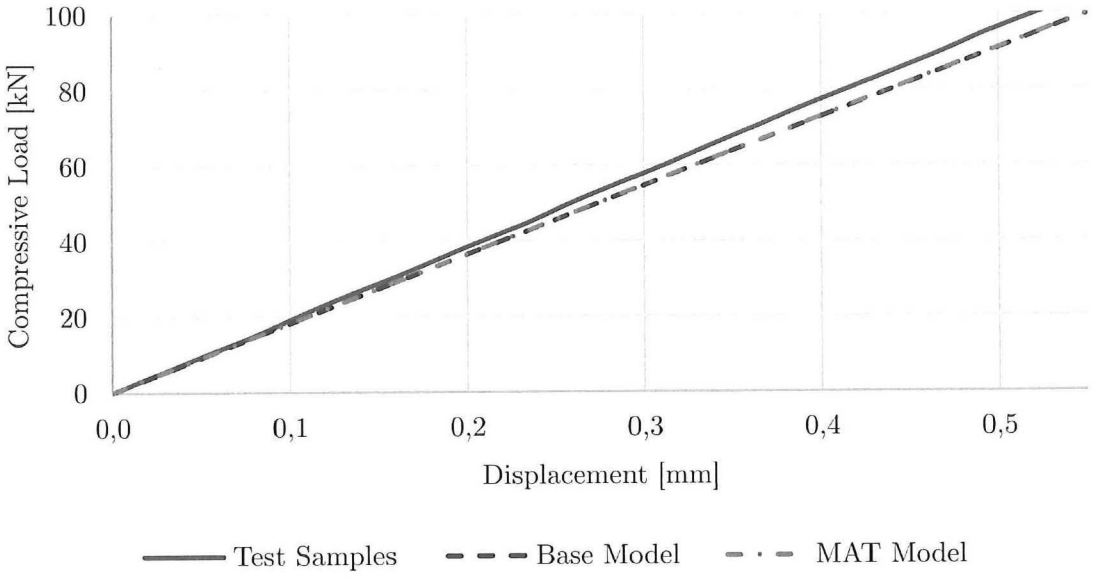

Figure B.1: Global stiffness of improved material assignment model for C1

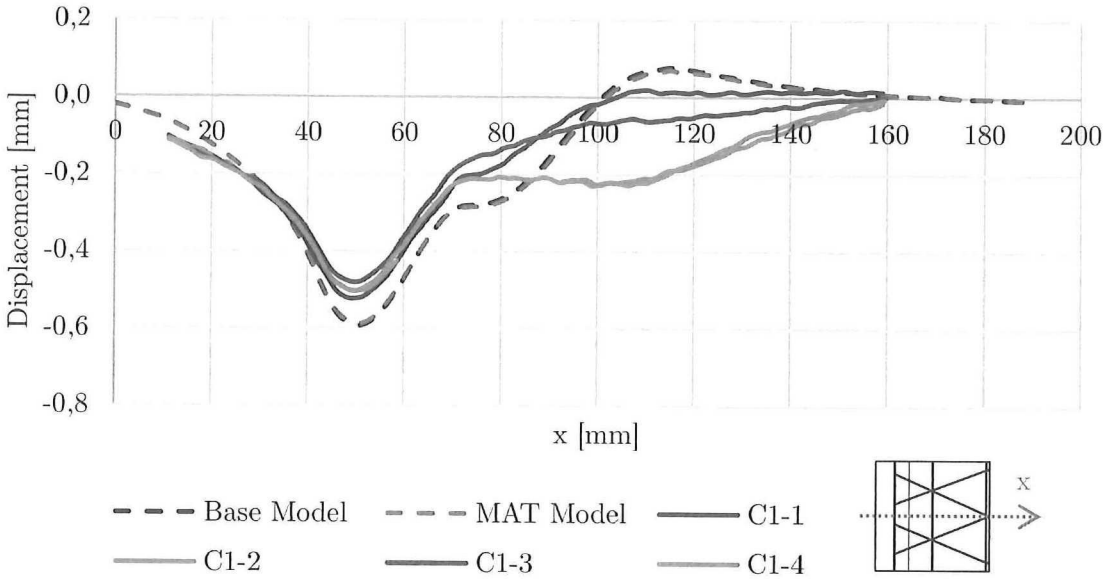

Figure B.2: Out-of-plane displacement at 93kN along middle line of improved material assignment model for C1

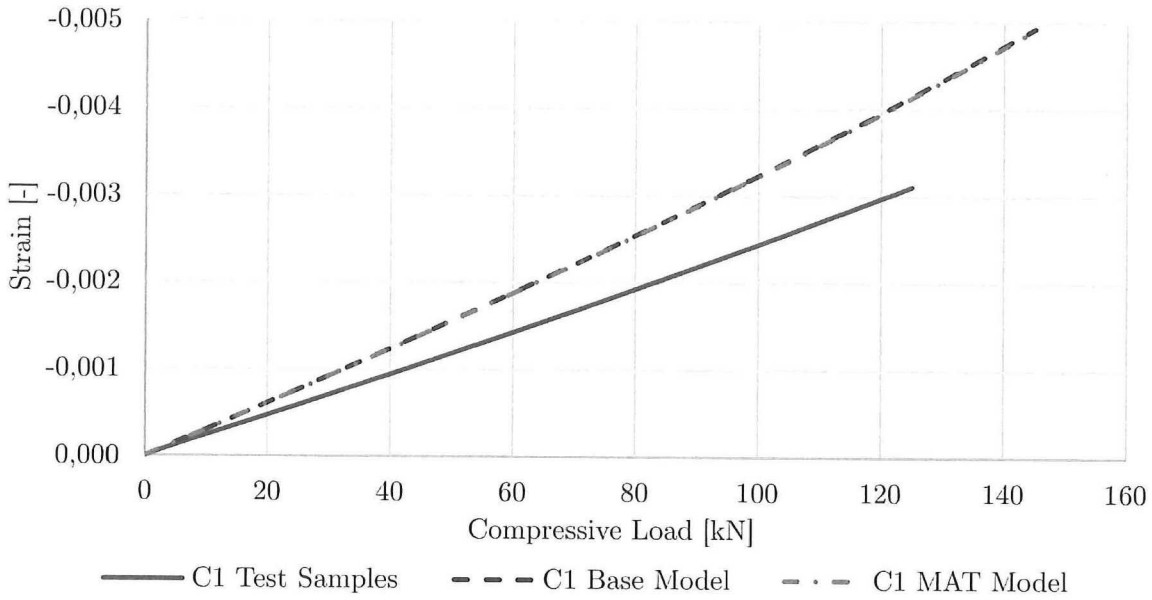

Figure B.3: Strain measured at outer helical ribs of improved material assignment model for C1

B.2 C2 Configuration

The correlation of the base and improved FEM model with the C2 test samples can be found in Figure B.4, Figure B.5 and Figure B.6

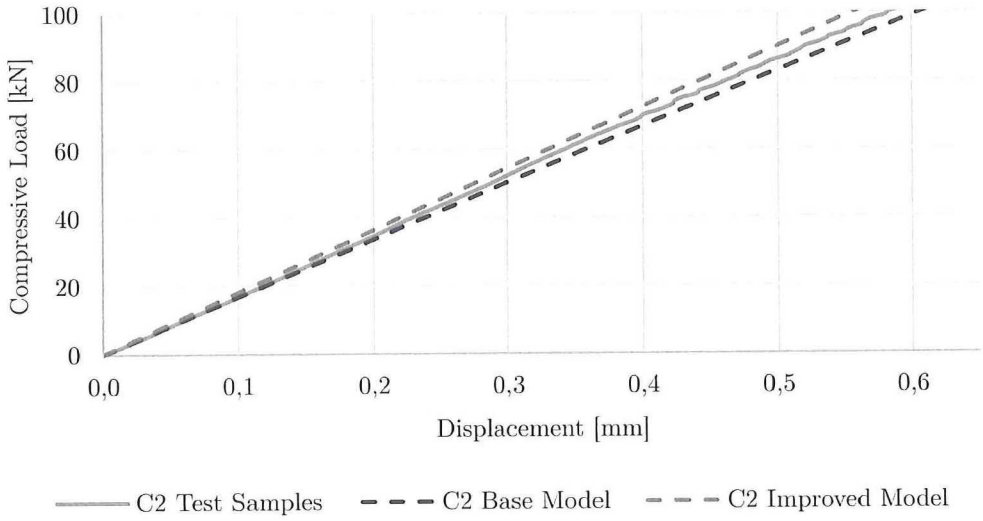

Figure B.4: Global stiffness of improved C2 model

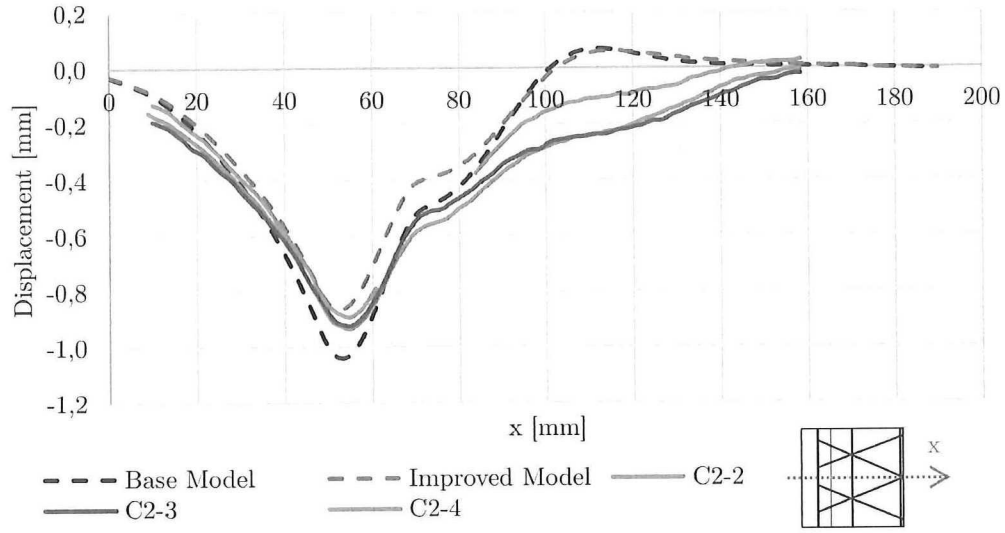

Figure B.5: Out-of-plane displacement at 93kN along middle line of improved C2 model

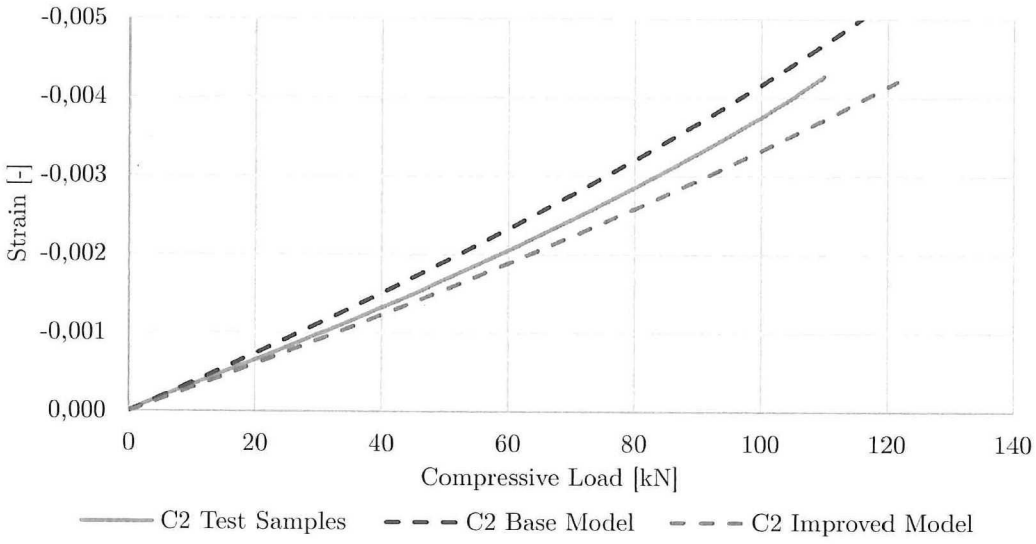

Figure B.6: Strain measured at outer helical ribs of improved C2 model